Differential Cross Sections in $\pi^{\pm}p$ Scattering at Low Energies

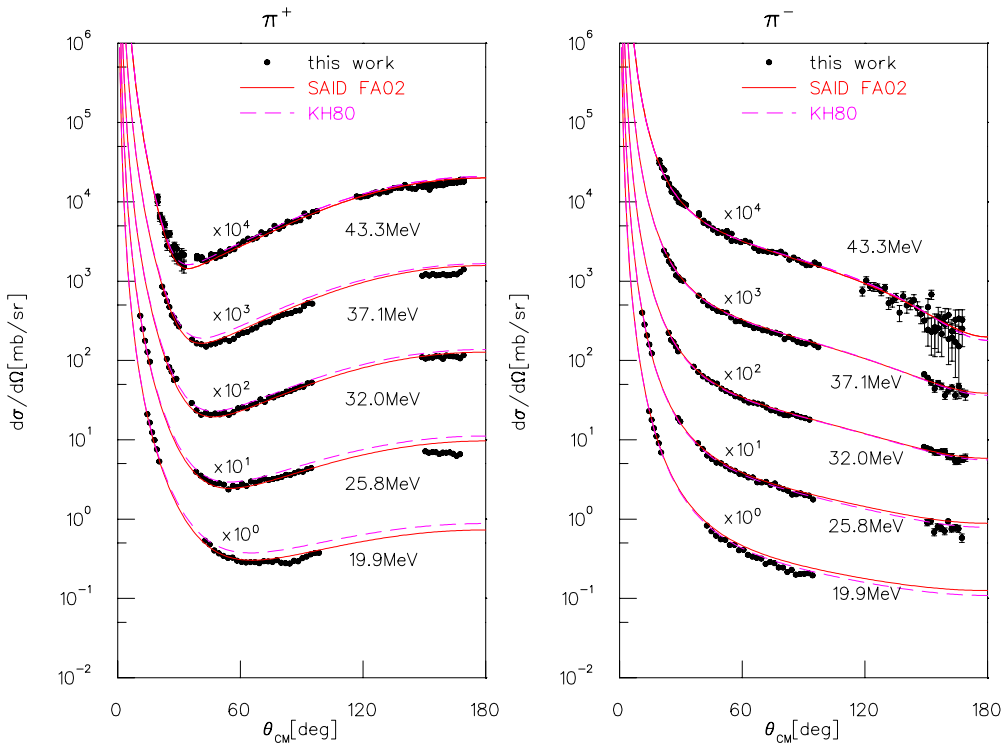

Dissertation

zur Erlangung des Grades eines Doktors
der Naturwissenschaften
der Fakultät für Mathematik und Physik
der Eberhard-Karls-Universität Tübingen

vorgelegt von
Holger Denz
aus Tübingen

2004

Tag der mündlichen Prüfung: 02.07.2004
Dekan: Prof. Dr. H. Müther
1. Berichterstatter: Prof. Dr. G.J. Wagner
2. Berichterstatter: Prof. Dr. H. Clement

The pion-nucleon sigma term, which is an important parameter in chiral perturbation theory and a measure of explicit chiral symmetry breaking of QCD due to non-vanishing current quark masses, can be extracted from elastic πp scattering data using partial wave analyses and dispersion relations. However, results of recent analyses yield a very large value for the sigma term, which leads to problems with the interpretation. Since the quality of the database on which the extraction is based is crucial for the result and there are known problems with incompatible measurements and scarce low energy data available, a new experiment was carried out within the CHAOS collaboration. Using the CHAOS detector and a newly developed range telescope covering the extreme forward scattering angles, differential cross sections in $\pi^{\pm}$p elastic scattering were measured at 19.9, 25.8, 32.0, 37.1, 43.3, 57.0 and 67.0 MeV pion kinetic energy at the TRIUMF meson factory in Vancouver, Canada. The CHAOS detector consists of tracking chambers and particle identification counters in a vertical magnetic field geometry. This experimental arrangement allows simultaneous measurements over a large angular range from 10 to 170 degrees, thus reducing systematic errors. Well-known $\mu^{\pm}$p scattering cross sections at forward angles were measured simultaneously as a check of the angle reconstruction and normalization.

This thesis describes the analysis of the low energy data from 19.9 to 43.3 MeV. Typical relative errors for the data are about 3 % statistical error per data point and between 3 and 8 % systematic error for the data sets.

For π^-p elastic scattering, the results of this experiment at 43.3 MeV lie in-between the data by Brack et al. and Joram et al. At 32.0 MeV the results are similar to the Joram et al. data for angles up to 80 degrees, at larger angles deviations are observed. For π^+p elastic scattering, particularly the low cross sections seen by Joram et al. in the Coulomb-nuclear interference region and at backward angles are not confirmed. Overall the results agree well with the SAID partial wave analysis in the π^-p channel at higher energies, but show some deviations at 25.8 and 19.9 MeV. For the π^+p channel, the data are systematically lower than predicted by the SAID partial wave analysis at backward angles, and the Coulomb-nuclear interference minimum is less pronounced than predicted. In the π^-p channel, the KH80 partial wave analysis solution gives a better description of the data than the SAID solution. In π^+p scattering, the KH80 solution is higher than the SAID solution. This yields a better description at forward angles, however at backward angles it does not match the behavior observed in the data.

The data from this experiment almost triple the available world data base for $\pi^{\pm}$p elastic scattering at low energies. It will be very interesting to see the impact of these data on the phase shifts obtained by partial wave analyses and on the value of the sigma term.

Contents

Chapter 1

Introduction

Experimental studies of the pion-nucleon system allow us to test and expand our knowledge of the strong interaction, one of the fundamental forces in nature. As a system which is to first order composed of 5 quarks, it is still fairly simple. Using high intensity pion beams produced at meson factories like LAMPF, PSI and TRIUMF, many scattering experiments have been performed in the last decades. In contrast, direct $\pi\pi$ scattering experiments probing the simplest hadronic system are still not possible today due to the short lifetime of the pions, although the DIRAC experiment at CERN now measures the lifetime of pionium and thus allows an indirect determination of $\pi\pi$ scattering amplitudes [Lan99].

Presently, the following quantities accessible through the πN system are of particular interest:

πNN coupling constant: The strength of coupling of a pion to a nucleon is needed e.g. in calculations using meson exchange models to describe the binding of nucleons. It can be determined from nucleon-nucleon

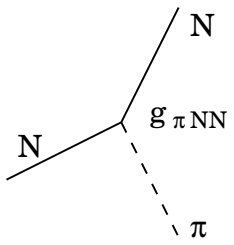

Figure 1.1: *πNN vertex*

scattering data or pion-nucleon scattering data by means of partial wave analyses.

isospin violation: For equal masses of up- and down-quarks the strong interaction should be invariant under isospin transformations. In that case, the 3 channels π^+p elastic scattering, π^-p elastic scattering and

the single charge exchange reaction π^-p$\rightarrow \pi^0$n can be described by only 2 scattering amplitudes corresponding to isospin 1/2 and 3/2. The size of isospin violation is connected to the mass difference between up- and down-quarks and might thus lead to a better determination of the current quark masses.

pion-nucleon sigma term: The pion-nucleon sigma term is a measure of explicit chiral symmetry breaking due to non-zero current quark masses and connected to the structure of the nucleon, especially the strange quark content and the generation of the nucleon mass. Unfortunately there is a long-standing and even increasing problem with the size of the strange quark content of the nucleon derived from a combined analysis of baryon masses and pion-nucleon scattering amplitudes. This continues to be a major concern up to today.

The following sections give a short overview of some of the theoretical background relevant to this thesis. They are not intended as a thorough and complete introduction, but rather as a brief reminder of concepts. Further information on pion-nuclear scattering can be found e.g. in a nice review [Klu91], and an introduction to the theoretical concepts can be found in [Che84].

After a short introduction into Quantum Chromodynamics as the fundamental theory of the strong interaction, a low energy effective theory, chiral perturbation theory, is described. Section 1.2 introduces partial wave analyses which are used to connect the measured data to quantities used in theory. One of these quantities is the pion-nucleon sigma term. Its extraction from baryon masses, from pion-nucleon scattering data and the implications for the structure of the nucleon and the problems to pinpoint its value are discussed in section 1.3. The role of the existing datasets in this puzzle is discussed in the last section (1.4).

1.1 Fundamental theory of strong interaction

1.1.1 QCD

At high energies Quantum Chromodynamics (QCD) provides a good description of the strong interaction. It features quarks carrying a color charge as elementary particles. Gluons acting as exchange particles generate the interaction. The quarks and gluons are described as fields, and the basic Lagrangian for the the 3 lightest flavors (u,d,s) is:

$$\mathcal{L}_{QCD} = \sum_{k=u,d,s} \bar{q_k} i\gamma^\mu (\partial_\mu - ig\frac{\lambda^a}{2} A^a_\mu) q_k - \frac{1}{2} tr G^a_{\mu\nu} G^{a\mu\nu} - \sum_{k=u,d,s} m_k \bar{q_k} q_k$$

where q_k denote the quark fields ($k = u, d, s$ for the 3 flavors), A the gluon gauge fields and λ the Gell-Mann matrices. The gluon field strength tensor can be derived from the gluon gauge fields A by $G_{\mu\nu} = \partial_\mu A_\nu - \partial_\nu A_\mu - ig[A_\mu, A_\nu]$. g is the coupling constant determining the strength of the interaction. The last term is the quark mass term. It vanishes in the case of zero quark masses.
Important features of QCD are confinement and asymptotic freedom of quarks. The QCD Lagrangian holds symmetries which are by Noether's theorem connected to conserved quantities. It is invariant under local SU(3) color transformations (color is conserved locally), invariant under global SU(3) flavor transformations for equal quark masses $m_u = m_d = m_s$ (flavor symmetry), and for zero quark masses invariant under $SU(3)_L \otimes SU(3)_R$, i.e. the left- and right-handed quarks do not interact (chiral symmetry).

In QCD-inspired quark models baryons and mesons are constructed as colorless objects containing 3 quarks and a quark-antiquark pair, respectively. If only up- and down-quarks are considered, the mass term of the Lagrangian is

$$m_u \bar{u} u + m_d \bar{d} d.$$

It is instructive to rewrite this term as follows:

$$m_u \bar{u} u + m_d \bar{d} d = \underbrace{\frac{m_u + m_d}{2}(\bar{u}u + \bar{d}d)}_{\text{chiral symmetry breaking}} + \underbrace{\frac{m_u - m_d}{2}(\bar{u}u - \bar{d}d)}_{\text{isospin violation}}$$

The first term vanishes in the limit of zero current quark masses and thus is a measure of the explicit breaking of chiral symmetry. It will be discussed in section 1.3.
The second term contains the difference between up- and down-quark masses. This difference is connected to the breaking of isospin symmetry in the strong interaction [Fet01, Amo01]. Experimental tests of this symmetry aim at providing a better determination of the mass difference.

1.1.2 Chiral perturbation theory

Towards low energies, the effective strong coupling constant rises, and a perturbative approach using an expansion in powers of this coupling constant is

not possible anymore. To overcome this problem, an effective theory called chiral perturbation theory has been developed using mesonic degrees of freedom.
The chiral symmetry is spontaneously broken: Although the Lagrangian is chirally symmetric, the scalar density $\langle \bar{q}q \rangle$ (chiral condensate) is not. According to the Goldstone theorem [Nam60, Nam61, Gol61, Gol62], this breaking of chiral symmetry gives rise to 8 massless pseudoscalar Goldstone bosons (identified as pions, kaons and η).

The explicit breaking of chiral symmetry due to the small but non-zero current-quark masses ($m_u \approx 1.5 - 4.5$MeV, $m_d \approx 5 - 8.5$MeV, $m_s \approx 80 - 155$MeV [PDG02]) causes a finite mass for the Goldstone bosons, however they are still exceptionally light compared to other hadrons.

1.2 Partial wave analysis

To make the connection between measured data, the scattering amplitude and results of theoretical models, partial wave analyses are used. In the following, after a short description of kinematic variables and the crossing symmetry connecting several channels in the πN sector, the scattering amplitude, partial waves and the connection to experimental data are discussed.

1.2.1 Mandelstam variables and crossing symmetry

In the description of pion-nucleon scattering often the Lorentz-invariant "Mandelstam" variables s, t and u are used [Man59]:

$s = (p+q)^2$ **:** total energy

$t = (q-q')^2$ **:** four-momentum transfer in the reaction.

$u = (p-q')^2$

$\nu = (s-u)/4M$ is related to the kinetic energy of the incoming particle.
p and q denote the four-momentum vectors of the pion and the nucleon before the scattering, p' and q' the corresponding vectors after the scattering process, and μ and M are the masses of the particles.
For example, the reaction $\pi^+ p \to \pi^+ p$ is shown in the left graph of fig. 1.2. The total energy in this reaction is given by s, therefore this channel is called the s-channel.
The reactions $p\bar{p} \to \pi^-\pi^+$ (t-channel) and $\pi^- p \to \pi^- p$ (u-channel) can be reached by employing the crossing symmetry. In the first case, the π^+ on the left side of the equation is replaced by its antiparticle π^- on the right side,

and similarly the proton is crossed as antiproton to the left.

Due to this crossing symmetry, one scattering amplitude describes all 3

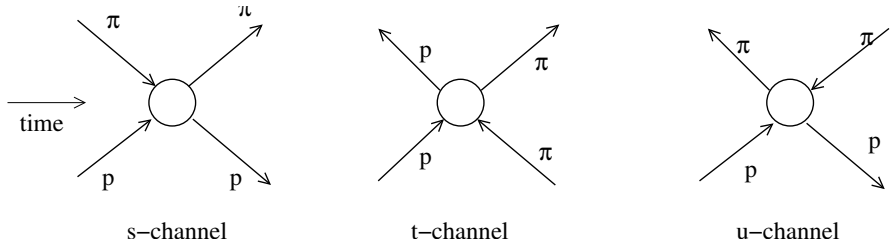

Figure 1.2: *s-, t- and u-channel in pion-proton scattering: Starting from $\pi^+ p$ elastic scattering (s-channel, left graph), the reactions $\bar{p}p \rightarrow \pi^-\pi^+$ (t-channel, middle graph) and $\pi^- p$ elastic scattering (u-channel, right graph) can be reached by utilizing the crossing symmetry. Antiparticles are depicted as particles propagating backward in time.*

reactions, however the reactions occupy different spaces in the Mandelstam $\nu - t$ plane. This is shown in fig. 1.3.

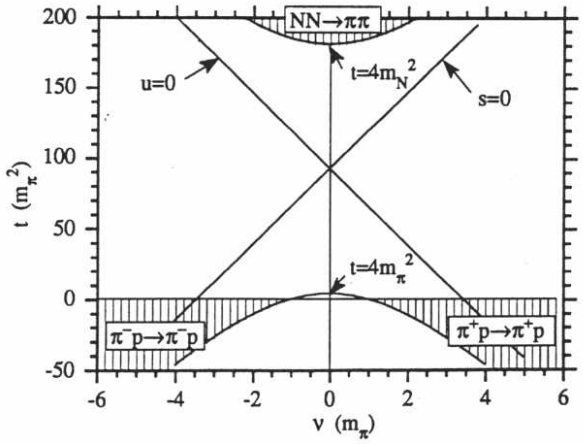

Figure 1.3: *Mandelstam $\nu - t$ plane (illustration taken from [Met90]): experimentally accessible areas for the 3 reactions are hatched.*

1.2.2 Partial waves

The wave function for the scattering of a spin-0 particle off a spinless target is given by:

$$\psi(r) = \frac{1}{\sqrt{k}}(e^{ikz} + f(\theta, k)\frac{e^{ikr}}{r})$$

where θ and k denote the scattering angle and the momentum of the particle in the center-of-mass system. The cross section is given by

$$d\sigma(\theta)/d\Omega = |f(\theta, k)|^2$$

The scattering amplitude $f(\theta, k)$ can be decomposed into partial waves of angular momentum l:

$$f(\theta, k) = \frac{1}{k}\sum_{l=0}^{\infty}(2l+1)e^{i\delta_l}sin\delta_l P_l(cos\theta)$$

An interesting feature of the scattering amplitude f is that it actually consists of two parts due to different interactions, the Coulomb part f_C and the nuclear part f_n. The nuclear interaction is a short-range interaction, in contrast the Coulomb interaction has an infinite range. Therefore the Coulomb amplitude dominates at very forward scattering angles, the nuclear amplitude at larger angles. In between, there is a region where the amplitudes are of the same size and the shape of the cross sections is influenced by the interference term (the Coulomb-nuclear interference):

$$\sigma = |f_n|^2 + |f_C|^2 + 2Re(f_C^* f_n)$$

Because of the attractive nature of the strong interaction, this interference is destructive in the π^+p channel and constructive in the π^-p channel. The effect of the interference can be seen in fig. 1.4. Shown are π^+p and π^-p differential cross sections measured at 32.2 MeV. The difference in shape of the two channels is in part due to the Coulomb-nuclear interference term. In principle, the real part of the isospin-even forward scattering amplitude can be directly determined from π^+p and π^-p data measured in the Coulomb-nuclear interference region. This was for example done in [Met90].
Due to the short range of the nuclear force, at low energy after a separation of the Coulomb part the nuclear scattering amplitude can be described by just a few partial waves corresponding to small angular momenta.
In the case of pion-nucleon scattering, the target carries a spin of 1/2, and the scattering can be described by 2 scattering amplitudes, the spin non-flip amplitude $G(s,t)$ and the spin flip amplitude $H(s,t)$. These amplitudes can in turn be expanded in partial waves:

$$G(s,t) = \frac{1}{k}\sum_{l=0}^{\infty}[(l+1)T_{l+} + lT_{l-}]P_l(cos\theta)$$

and

$$H(s,t) = \frac{1}{k}\sum_{l=0}^{\infty}(T_{l+} - T_{l-})P_l'(cos\theta)$$

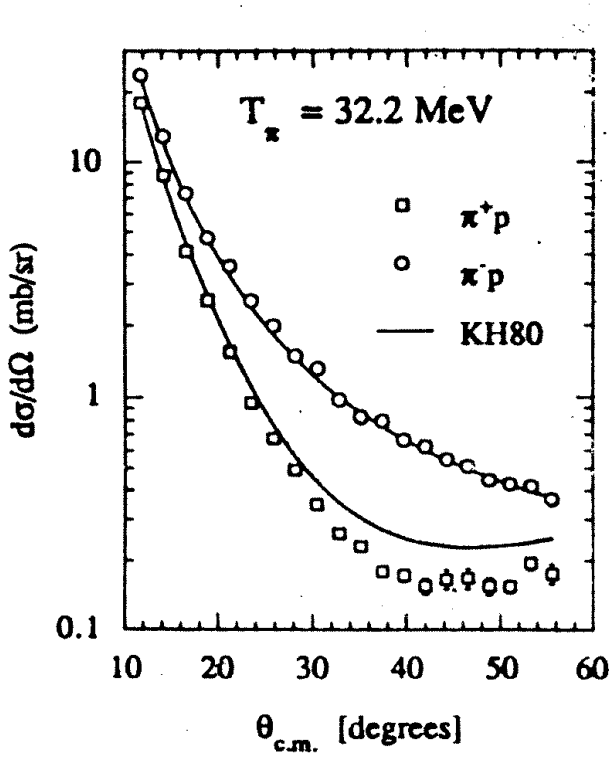

Figure 1.4: *π^+p and π^-p differential cross sections at 32.2 MeV [Met95]: the difference in shape for the two channels is in part due to the Coulomb-nuclear interference term.*

where

$$T_{l\pm} \equiv kf_{l\pm} = \eta_{l\pm}[exp(2i\delta_{l\pm}) - 1]/2i$$

and $f_{l\pm}$ are the partial wave amplitudes, $\delta_{l\pm}$ are the phase shifts and $\eta_{l\pm}$ the inelasticities. The total angular momentum for the partial waves is $j = l\pm 1/2$ for the index $l\pm$. Since at low energies elastic scattering processes dominate, the inelasticities $\eta_{l\pm}$ are close to 1.

The differential cross section is given by

$$d\sigma/d\Omega = |G|^2 + |H|^2$$

1.3 Sigma term

The pion-nucleon sigma term

$$\sigma_{\pi N} = \frac{m_u + m_d}{2}\langle N|\bar{u}u + \bar{d}d|N\rangle$$

is an important quantity in hadronic interactions. In the framework of chiral perturbation theory it is a measure of explicit breaking of chiral symmetry due to nonvanishing current quark masses. In the chiral limit, its value goes to 0. It is directly connected to the density dependence of the chiral condensate $\langle \bar{q}q \rangle$[Bro96].
It also gives the contribution of the current quark masses of the two lightest quarks (u,d) to the total mass of the nucleon, for example the proton mass can be written [Gas81] as

$$M_p = M_0 + \sigma_{\pi N} + m_s \langle p|\bar{s}s|p\rangle$$

where M_p is the total mass of the proton, M_0 denotes the mass generated dynamically by binding of the quarks and gluons, the sigma term $\sigma_{\pi N}$ the mass due to the up/down current quark masses and the last term the contribution due to the current quark mass of the strange sea quarks.

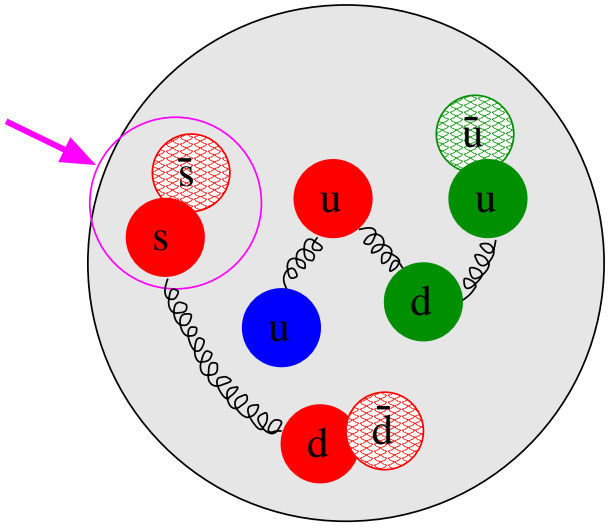

Figure 1.5: *Illustration of the quark and gluon structure of the proton: strange quarks form part of the sea quarks.*

The value of the pion-nucleon sigma term can be determined in two ways, from baryon masses and from πN scattering. A comparison of the values obtained by the two methods allows one to determine the strange quark content in the nucleon and the contribution of the strange quarks to the total nucleon mass. These are expected to be non-zero due to the presence of $\bar{s}s$ sea quark pairs (fig. 1.5).

1.3.1 Determination from baryon masses

The simplest method to calculate $\sigma_{\pi N}$ from baryon masses is

$$\sigma_{\pi N} = \frac{m_q}{m_s - m_q}(m(\Xi) + m(\Sigma) - 2m(N))$$

where $m_q = (m_u + m_d)/2$. For the masses of the baryons the measured values are used, the ratio m_q/m_s is determined from kaon masses to 24.4 ± 1.5 [Leu96]. This yields a value of 25 MeV [Gas81]. A detailed calculation [Bor97] within the framework of chiral perturbation theory [Gas88, Gas88b] yields

$$\sigma_{\pi N} = \frac{36 \pm 7}{1 - y}\text{MeV}$$

where

$$y = \frac{2\langle N|\bar{s}s|N\rangle}{\langle N|\bar{u}u + \bar{d}d|N\rangle}$$

is a measure of the strange quark content of the nucleon wave function.

1.3.2 Determination from pion-nucleon scattering data

A value for the pion-nucleon sigma term can also be extracted from pion-nucleon scattering data. This is illustrated schematically in figure 1.6.

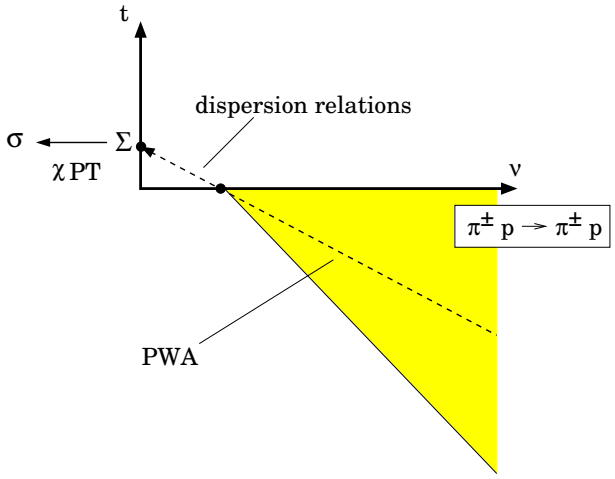

Figure 1.6: *Schematic picture of the extraction of $\sigma_{\pi N}$ from πN scattering data*

Shown is the plane of Mandelstam variables t vs. ν.
The experimentally accessible area is shaded. Using a partial wave analyis,

the scattering amplitude is extracted from the data. The scattering amplitude is then extrapolated to the Cheng-Dashen point in the unphysical region at $\nu = 0$, $t = 2\mu^2$. This extrapolation is done assuming analyticity for the scattering amplitude and considering constraints given by dispersion relations. The value of the isospin-even (average of the π^-p and the π^+p channel) forward scattering amplitude at the Cheng-Dashen Point is connected to the pion-nucleon sigma term.
Several different partial wave analyses have been performed. The two most influential ones are the Karlsruhe-Helsinki partial wave analysis and the SAID[1] analysis.
The Karlsruhe-Helsinki partial wave analysis [KH80] was published in 1980 and is still considered to be treating the extrapolation into the unphysical area and the constraints most vigorously. However, the available database has increased significantly since the analysis was performed, and new data sets measured at dedicated meson facilities are much more precise than the data used in the KH80 analysis.
The second partial wave analysis is the SAID partial wave analysis [Arn02] presently performed by the group at George Washington University, Washington D.C. This analysis over the years has included more and more features of the "old" KH80 analysis, but is based on the full database available today and updated regularly.

Σ can then be calculated from the scattering amplitude at the Cheng-Dashen point after subtracting the pseudovector nucleon Born term [Wei66, Che71, Bro71]. To obtain the pion-nucleon sigma term $\sigma_{\pi N}$, other corrections calculated by dispersion relations [Gas91] and/or chiral perturbation theory [Ber96, Bec99] have to be applied; in effect

$$\sigma_{\pi N} = \Sigma - 15 \text{ MeV}$$

The extraction of Σ from pion-nucleon scattering data has been performed by various groups, and the change over the years is illustrated in figure 1.7. The resulting values for Σ show a large scatter and an overall increase over the years and have recently settled in the region of 85 MeV. This implies a value of around 70 MeV for $\sigma_{\pi N}$ from pion-nucleon scattering.

1.3.3 Comparison

Comparing the values for $\sigma_{\pi N}$ obtained from baryon masses and from pion nucleon scattering yields a possibility to determine y. However, to obtain the same value for $\sigma_{\pi N}$, in the extraction from baryon masses a value of y=0.5

[1] Scattering Analysis Interactive Dialin

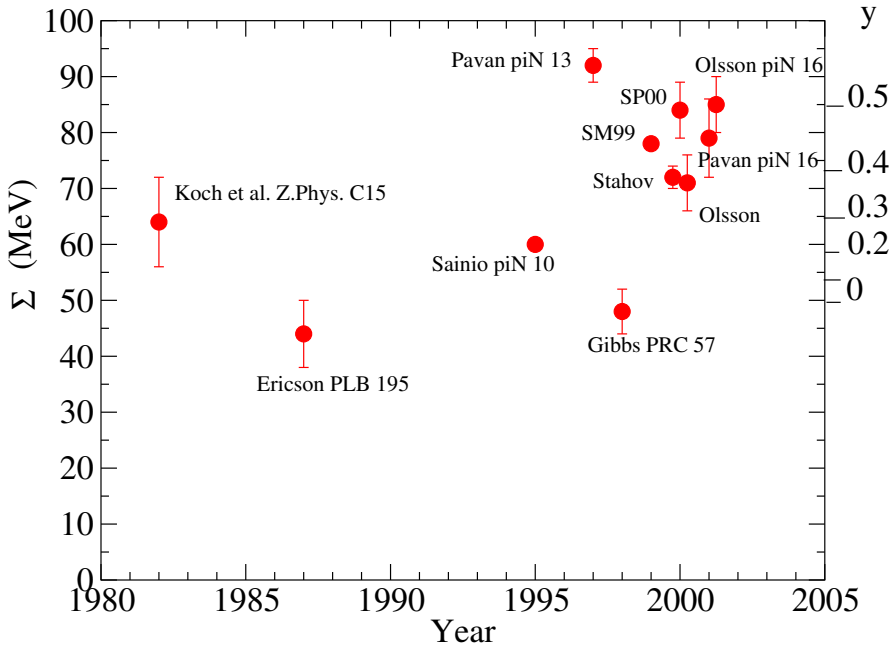

Figure 1.7: *Value of Σ obtained from several extractions [Koc82, Eri87, Sai95, Pav97, Gib98, Pav99, Sta99, Ols00, Pav01, Ols01] plotted over the year of the publication*

for the strangeness content in the nucleon would be required. Thus, in a naive calculation the strange quark mass contribution to the total nucleon mass would be roughly

$$m_s\langle p|\bar{s}s|p\rangle \cong \frac{m_s}{m_q}\frac{y\sigma_{\pi N}}{2} = 25\frac{0.5\cdot 70\text{MeV}}{2} = 440\text{MeV}$$

Results from deep-inelastic neutrino scattering are also sensitive to the strange quark content of the nucleon and do not support such a large value [Baz95]. A possible reason for the large value of y obtained might be the pion-nucleon data base the extraction of Σ is based on. The experimental data for pion-nucleon scattering at low energies which are available for the extraction of Σ using partial wave analyses will be presented in the next section.

1.4 πp database

Crucial for the extrapolation of the phases to the Cheng-Dashen point is a good knowledge of the phases close to the πN threshold. Unfortunately, due

to the short lifetime of slow pions, experiments with pions become increasingly challenging as one approaches this limit. Thus, especially when going to low energies, the available data become scarce. Also, partial wave analyses rely on data points measured in various experiments, and it turns out that the data sets are sometimes not compatible within the errors quoted by the authors [Fet97].
Figure 1.8 shows the distribution of all available differential cross section data for π^+p and π^-p elastic scattering at an incident pion energy of less than 50 MeV. In addition, pionic hydrogen experiments performed at PSI provide data for π^-N scattering exactly at threshold [Sch01].
Furthermore, analyzing power measurements provide additional information since they are sensitive to other partial waves. Thanks to two recent experiments [Pat02, Mei04], data for this observable are now available in the low energy regime down to 45 MeV. A comparison of different data sets for

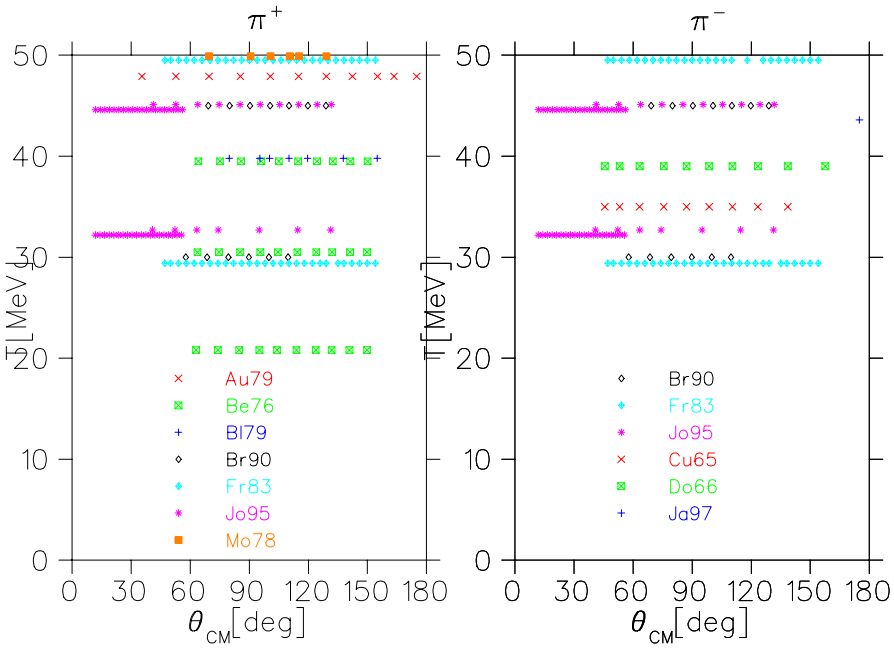

Figure 1.8: *Angle and energy distribution of available data for π^+p and π^-p elastic scattering below 50 MeV [Aul79, Ber76, Ble79, Bra90, Fra83, Jor95, Jor95b, Moi78, Cun65, Don66, Jan97]*

π^+p elastic scattering at low energies is shown in figure 1.9. Some caution has to be taken since the data are not measured at exactly the same energy, but even after correcting for the slightly different kinetic energies assuming an energy dependence as given by partial wave analyses, the experimental

data measured by different groups show disagreements which are beyond the quoted errors.

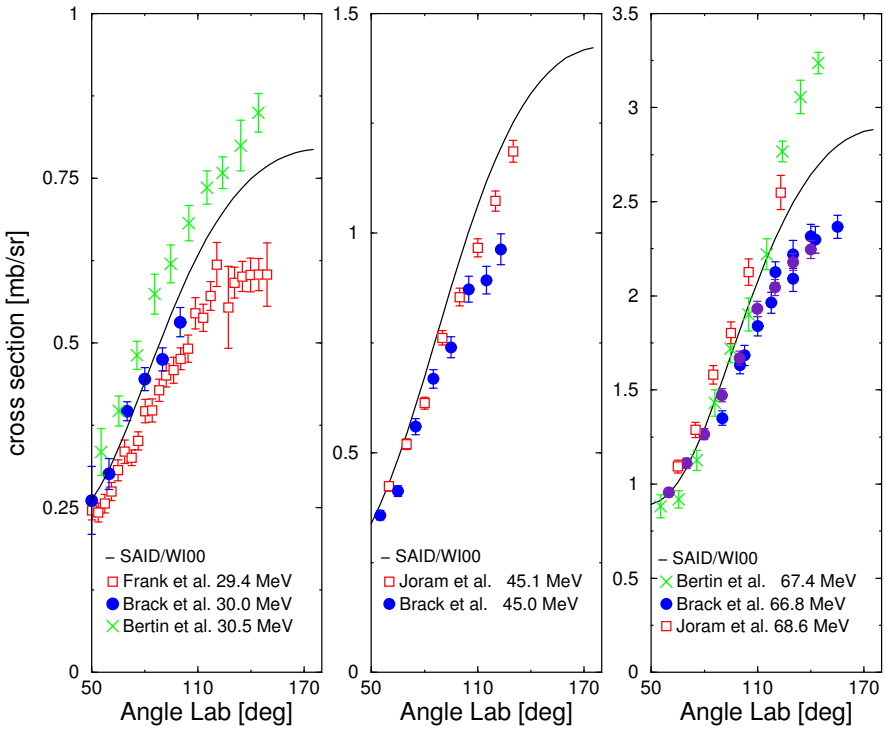

Figure 1.9: *Comparison of cross sections measured at roughly the same incident pion energy*

This unsatisfactory situation with the database (scarce data at low energy and contradicting data sets) and the importance of the pion-nucleon sigma term was the main motivation for the CHAOS[2] collaboration (for a complete list of the institutions and people involved see Appendix A) to carry out TRIUMF[3] experiment E778 [Smi96] which is described in this thesis. The idea of this experiment is to measure high quality differential cross sections for both π^+p and π^-p elastic scattering at several energies from 19.9 to 67.0 MeV and over a large angular range with the CHAOS detector. This detector is well suited for the experiment since it covers the full angular distribution simultanously, has a rather compact design and is built out of light materials. This reduces the problems due to energy loss and decays due to the short decay length of slow pions which pose severe experimental challenges at low

[2]Canadian High Acceptance Orbital Spectrometer
[3]TRI-Universities Meson Facility

energies.
If after the inclusion of the data from this experiment the extraction of Σ still requires a large strangeness content y, then alternative explanations will have to be found.
Several ideas have been put forward, questioning the extraction procedure from πp data [Sta02], the equivalence of the sigma terms extracted from πp scattering and baryon masses [Gib03], or the validity of the connection [Gas81] of baryon masses and sigma term [Lei00].

Chapter 2

Experimental setup

The experiment described in this thesis was performed at the M13 channel of the TRIUMF[1] research facility using the CHAOS spectrometer and a range telescope for the detection of scattered particles and a liquid hydrogen target. The different components of the experiment will be described in this chapter.

2.1 TRIUMF

TRIUMF is a Canadian research facility for nuclear and particle physics. It is located in Vancouver, British Columbia, Canada. The heart of the facility is a large cyclotron with a magnet diameter of 18 m that accelerates negatively charged H^- ions up to 520 MeV. The 2 electrons of the H^- ions are then removed by a thin stripping foil, and the protons are extracted into the 3 beam lines connecting to the newly built ISAC (isotope separator and accelerator) hall, the proton hall and the meson hall (fig. 2.1). The maximum current is about 200 μA in the beam line to the meson hall.
Due to the nature of acceleration the protons are delivered in bunches with a time structure corresponding to the cyclotron frequency of 23.06 MHz, resulting in one bunch every 43.37 ns.
Pions are produced on 2 production targets (usually beryllium or graphite) in the meson hall and the produced pions as well as their decay products (muons and electrons) are guided by secondary beam lines to several experimental areas.
M13 is a low-energy channel which was used for measurements from 43.3 MeV down to 19.9 MeV incident pion energy. M11 is a higher energy channel used for 37.3 to 67.0 MeV.

The M13 beam line which was used for the measurements described in this thesis consists of 2 dipole magnets and 7 quadrupole magnets (see fig. 2.2). A vertical slit after the first dipole magnet defines the momentum acceptance of the channel. The width of the slit was set to a momentum spread

[1] TRI-Universities Meson Facility

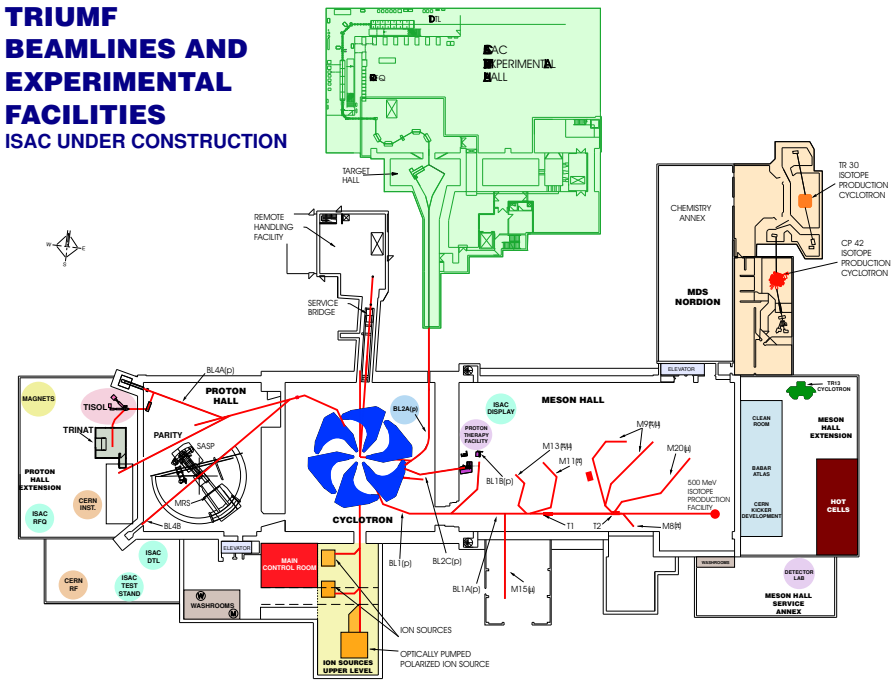

Figure 2.1: *TRIUMF beam lines and experimental facilities [TRI96]*

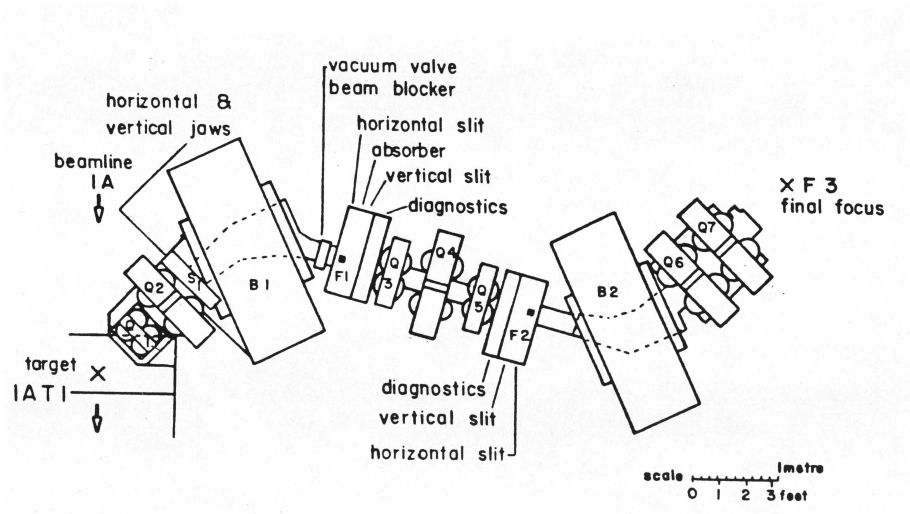

Figure 2.2: *M13 channel [Ora81]: The channel consists of 2 dipole magnets B1 and B2 and 7 quadrupoles Q1-Q7.*

p_{ch} [MeV/c]	p_π [MeV/c]	T_π [MeV]	p_μ [MeV/c]	T_μ [MeV]
120.6	118.2	43.3 ± 0.4	119.0	53.5
111.1	108.3	37.1 ± 0.4	109.2	46.2
103.0	99.8	32.0 ± 0.3	101.0	40.5
92.7	88.8	25.8 ± 0.3	90.3	33.3
82.2	77.1	19.9 ± 0.3	79.3	26.4

Table 2.1: *Channel momenta p_{ch} used at the M13 channel for the full target measurements and the corresponding momenta and kinetic energies for pions and muons in the center of the LH_2 target*

of 1 %. With the second dipole, the beam can be moved horizontally. The quadrupole doublets and triplet are beam focusing elements. By adjusting the quadrupoles Q6 and Q7, the final focus of the beam can be moved upstream or downstream. A full description of the channel can be found in [Ora81]. Typical beam rates of this channel with the slit settings used in this experiment were in the order of $10^5\pi/s$.
To identify pions, muons and electrons, the time of flight of the particles from the production target to the beam-defining finger counter after the beam pipe exit is used. Since there is no detectable signal at the production target, instead a signal generated by a capacitive probe in the proton beam line is used to obtain a start signal for the time of flight of the secondary particles in the beam line. Because the width of the proton bunches from the cyclotron determines the timing resolution for the secondary beam line, the accelerator tune was optimized for narrow proton bunches with a width of less than 2 ns for the higher energy measurements.

The momentum setting of the channel was monitored using NMR (nuclear magnetic resonance) probes measuring the magnetic fields of the momentum-defining dipole magnets with high accuracy. The absolute calibration was obtained by varying the distance between scintillator counters placed in a beam pipe extension and measuring the time of flight of pions, muons and electrons similar to the procedure used in earlier experiments for the M11 channel [Pav01c]. The uncertainty in the momentum in this calibration is estimated to be of the order of 0.6 %, resulting in an energy uncertainty for the pions of 1 to 1.5 % [Mat04]. The momentum settings for the M13 channel and the corresponding momenta and energies of the pions in the center of the liquid hydrogen target are given in table 2.1. The difference in momentum is due to energy loss in air, the finger counter, wire chambers and the target. For the empty target measurements, the channel momenta were adjusted to exactly match the momentum of the pions in the center of the target.

2.2 CHAOS

The main detector used in the experiment is CHAOS (short for "Canadian High Acceptance Orbital Spectrometer") [Smi95] . It is a dipole magnetic spectrometer with an almost 360° in-plane acceptance and an out-of-plane acceptance of ±7 degrees (see fig. 2.3). The plane is defined by the gap between the 2 poles of the magnet. In this gap 4 concentric rings of wire chambers are located. The outermost chamber is surrounded by CFT (CHAOS Fast Trigger) blocks each consisting of 2 scintillator layers and a lead-glass Cerenkov block. To create holes for the incoming and outgoing beam, usually 2 out of 20 blocks are removed.

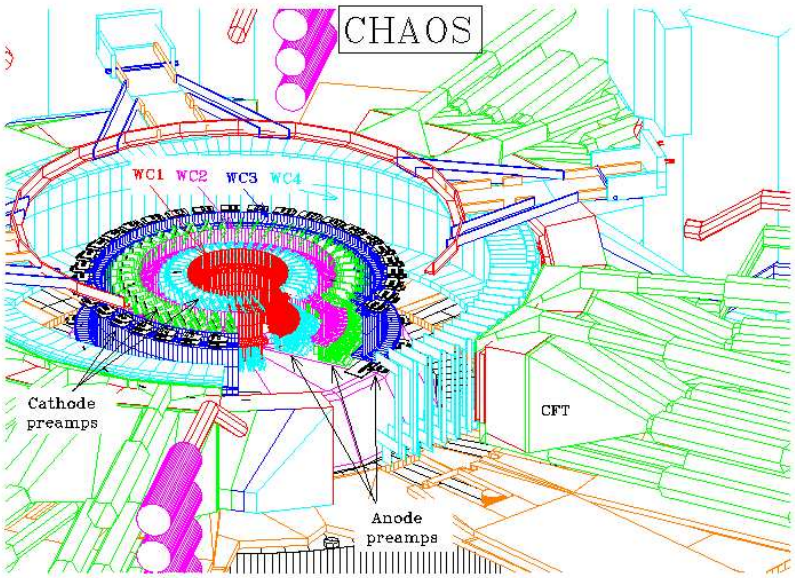

Figure 2.3: *CHAOS: view of detector elements*

In this experiment block # 19 was removed for the incoming beam. In addition blocks # 4 to 6 were removed, since the extreme forward region was covered by another detector, a range telescope (see section 2.3). An illustration of the experimental setup is shown in fig. 2.4.

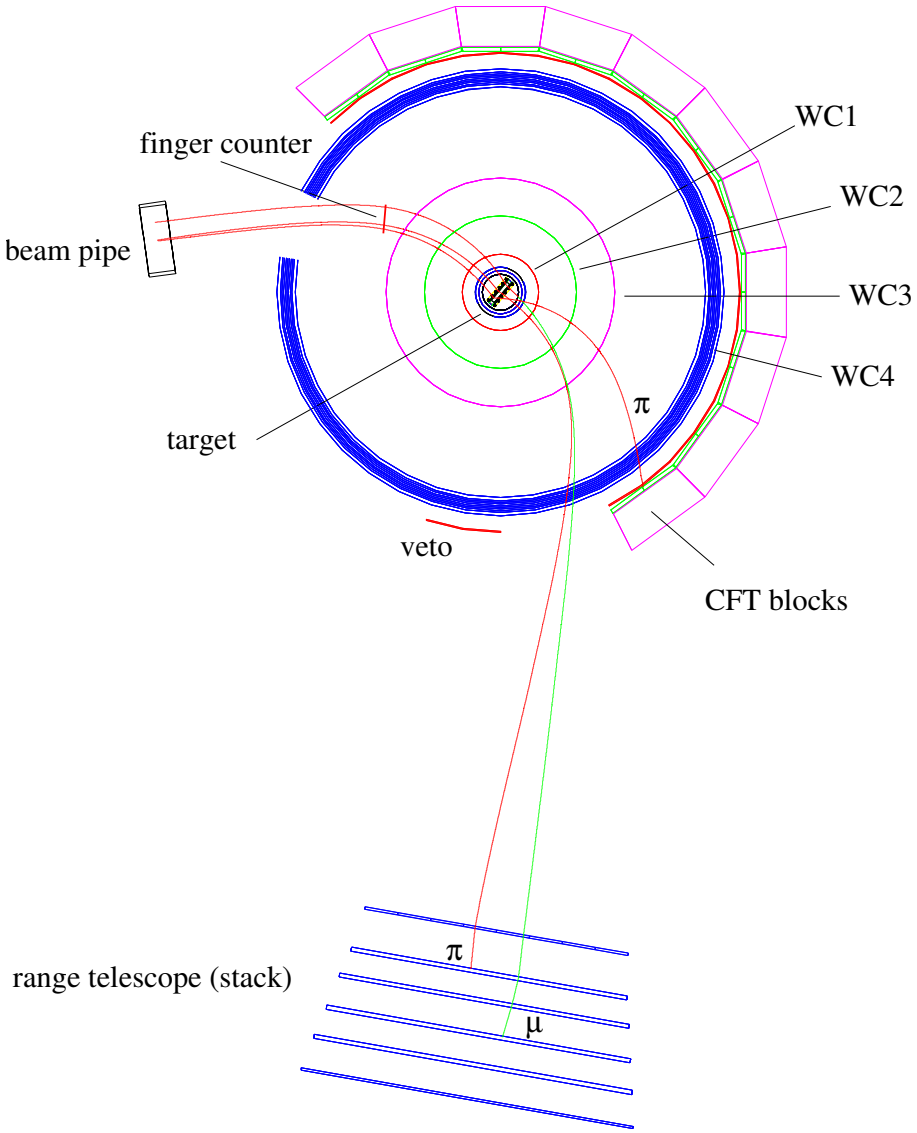

Figure 2.4: *E778 experimental setup: indicated are the 4 concentric rings of wire chambers of CHAOS, the surrounding CFT blocks used in this experiment (blocks # 7 to 17), the target in the center of the detector, the finger counter detecting the particles entering the apparatus, the range telescope positioned at forward scattering angles and the veto counter which is used to shield the range telescope from decays of unscattered beam particles after the target region. Three sample events are plotted: A scattered pion detected by a CFT block, a pion scattered at a smaller angle detected by the range telescope, and a pion decaying into a muon in the target region which is also detected by the range telescope.*

2.2.1 Magnet

The CHAOS magnet (fig. 2.5) has a homogenous field region extending in radius to WC3 with a maximum field of 1.5 T. Targets can be inserted into the center of the detector through a borehole in the top lid of the magnet. To correct for the distortion of the field caused by this borehole, a shim piece is built into the target holder.

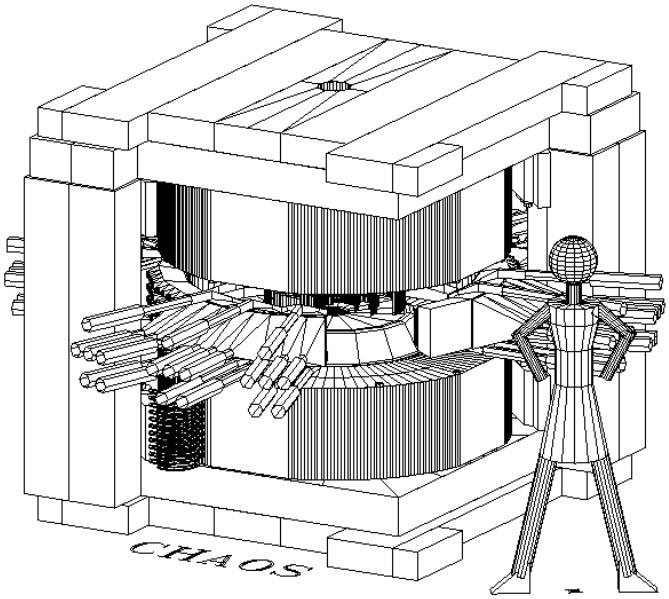

Figure 2.5: *CHAOS magnet: The detector elements are placed between the 2 coils of the magnet. A hole in the top lid of the magnet is used to lower targets into the center of the detector.*

In this experiment, the magnetic field was set to rather low values to prevent the low-energetic pions from spiraling up to a stop. The field ranged from 0.50 T at 19.9 MeV up to 0.95 T at 67.0 MeV. The magnetic field was monitored by an NMR probe and the magnet current was controlled by a feedback system to keep the field at a stable value. The absolute value of the magnetic field can be obtained from the curvature of pions and muons with known momentum (e.g. through-going beam).

2.2.2 Finger counter

The beam-defining finger counter scintillator detects the incoming particles from the beam line. It covers an area of 8 cm × 8 cm which is split into two vertical segments. The light from the two scintillators is detected by two fine-mesh high-field photomultipliers (Hamamatsu H6153). To minimize the energy loss of particles in this counter, its thickness is only 1 mm.

2.2.3 Wire chambers

The first two cylindrical wire chambers (WC1 and WC2) are proportional chambers. They feature 720 anode wires and 360 cathode strips each. The radii of the chambers are 11.46 cm and 22.92 cm, resulting in a wire spacing of 1 mm for WC1 and 2 mm for WC2 or 0.5 degrees for each of the chambers. Since a particle passing the chamber between two wires can create a signal at two wires, the actual resolution is improved to 0.25 degrees. The cathodes of the chambers are segmented into strips. The width of the strips is 2 mm for WC1 and 4 mm for WC2. These strips are tilted by 30 degrees with respect to the anode wires and thus provide information at what height the particle passed through the chamber.

The third wire chamber (WC3) is a drift chamber at radius 34.78 cm with an anode wire spacing of 15 mm (2.5 degrees). Four cathode strips per drift cell allow the resolution of the left-right ambiguity in the cell [Hof93].
The outermost chamber (WC4) is a vector drift chamber, consisting of 100 cells. Each cell is equipped with 8 radially aligned sense wires and 2 resistive wires which provide out-of-plane information. The first sense wire is at a radius of 61.25 cm, the spacing between the wires is 0.5 cm. Using the TDC information from the 8 sense wires, the direction of the particle in the chamber is obtained. To be able to resolve the left-right ambiguity in this cell, the sense wires are staggered by ±250 μm.
The typical momentum resolution for tracks reconstructed from the wire chamber information is 1 %, the scattering angle resolution is 0.5 degrees [Ker93].
Sections of wire chamber 3 were disabled by switching off the high voltage for the incoming and outgoing beam region. A section of wire chamber 4 was removed in the incoming beam region.

2.2.4 CFT blocks

The CFT blocks each cover an angular range of 18 degrees. Each block consists of two layers of plastic scintillator (the second layer is segmented in

two pieces) and a lead-glass Cerenkov block. The first scintillator layer is positioned at a radius of 72.0 cm. The first layer consists of 1/8 in (3.2 mm) of NE110[2], the second layer of 1/2 in (12.7 mm) of NE110. The height of the blocks defines the CHAOS out-of-plane acceptance of ±7 degrees.
With the information provided by the CFT blocks, electrons, pions and protons can be identified by Cerenkov light and energy loss vs. momentum plots. However, a discrimination between pions and muons is not possible, because their energy losses and therefore signals in the CFT blocks are very similar for particles of the same momentum.

2.2.5 CHAOS coordinate system

To identify a position in the CHAOS detector, two coordinate systems are used. One is a Cartesian coordinate system with the origin located in the center of CHAOS and an orientation of the axes as depicted in fig. 2.6.
Due to the cylindrical structure of the CHAOS detector, often polar coordinates are used instead. They consist of a radius from the center of CHAOS and an angle relative to the x-axis.
The CFT blocks are numbered from 1 to 20 in counterclockwise direction, as shown in fig. 2.6.

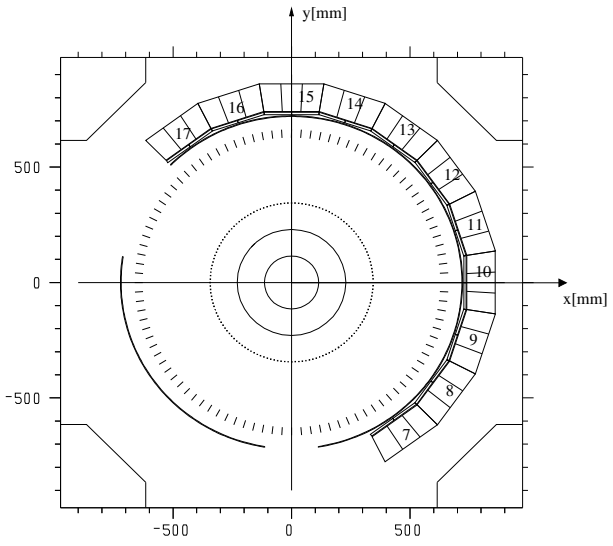

Figure 2.6: *Illustration of CHAOS coordinate system and CFT block numbering scheme: The directions of the axes are chosen parallel to the edges of the magnet lids.*

[2]Nuclear Enterprises (now Bicron) product identifier

2.3 Range telescope

A range telescope was used to handle the background of decay muons at forward scattering angles.
Pion decay into muons at low energies is one of the dominant sources of background. The muons can be divided into 5 classes.

1. Muons from decays in the production target are transported through the channel like pions of the same momentum. They are identified by TOF methods as mentioned earlier and used in the experiment for the μp cross sections that are measured simultaneously for normalization purposes.

2. Muons from decays in the channel are suppressed because they usually are not transported to the beam-defining finger counter.

3. The result of a simulation for muons from decays in the incoming beam region is shown in fig. 2.7. Due to the magnetic field of the detector the low-energetic part of the muons is focused towards the left. On the opposite side of the beam the contamination is lower, but still sizable at small angles. These events can be removed in the analysis by requiring a vertex in the target region.

4. The same is true for decays behind the target region.

5. The most problematic decays occur in the target region. In this experiment at low energies and forward pion scattering angles the recoil energy is too low to allow the proton to leave the target. Thus, only the scattered pion can be detected, and an identification of the reaction requiring both a detected pion and a proton is not possible. Therefore pions have to be separated from the decay muons by other means. Part of the decay muons can by identified by their momentum, but the distributions of the decay muons and the scattered pion band in the scattering angle vs. momentum plane overlap at forward angles (fig. 2.8). Therefore another way of identifying the particles is needed.

This is accomplished by a range telescope [Fra00] installed in the forward angle region. It covers in-plane scattering angles from approximately 8 to 30

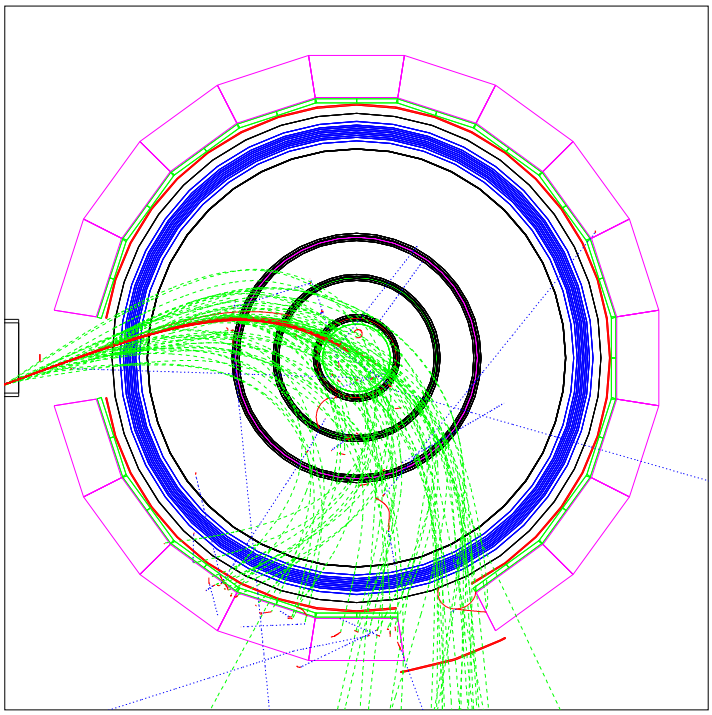

Figure 2.7: *Decay muons from pion decays in the incoming beam region. Due to the magnetic field of the detector the low-energetic part of the muons is focused towards the left. On the opposite side of the beam the contamination is lower, but still sizable at small angles.*

degrees with an out-of-plane acceptance of ± 6 degrees.
The telescope consists of 6 layers of plastic scintillators. The first layer is segmented into 8 vertical scintillator paddles. The dimension of each of these paddles is 40 cm high × 10 cm wide (see appendix E). They are read out at the top and the bottom by photomultiplier tubes. The other 5 layers are segmented into 2 horizontal bars and read out on the left and on the right side. The dimensions of the bars are 84.3 cm × 21.3 cm for layer 2, 88.5 cm × 22.3 cm for layer 3, 92.8 cm × 23.4 cm for layer 4, 97.1 cm × 24.5 cm for layer 5 and 101.3 cm × 25.5 cm for layer 6. The thickness of the first and the last layer is 0.25 in (0.64 cm), the middle layers have a thickness of 0.5 in (1.27 cm).
Between each pair of layers there is an 8 cm wide gap. This gap is required because of the diameter of the photomultiplier chassis and to allow insertion of aluminum absorber sheets to adjust the range telescope for different ener-

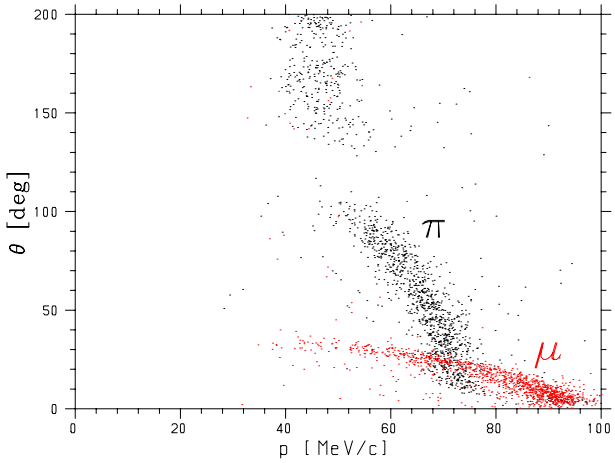

Figure 2.8: *Illustration of pion scattering band (black) and μ-band from pion decays (red) in an angle-vs.-momentum plot (simulation at 19.9 MeV, positive charge): Shown are two bands, the first one (black) corresponds to elastically scattered pions and follows the expected kinematics. The second band (red) is the result of pions decaying into muons in the target region. This band overlaps with the first band at forward angles. In this overlap region, a discrimination of the two processes using kinematic correlations is not possible.*

T_π [MeV]	d1 [cm]	d2 [cm]	d3 [cm]	d4 [cm]	d5 [cm]
43.3	0.95	0.95	0.64	0.48	0.0
37.1	0.48	0.48	0.32	0.32	0.0
32.0	0.16	0.16	0.16	0.16	0.0
25.8	0.16	0.16	0.0	0.0	0.0
19.9	0.0	0.0	0.0	0.0	0.0

Table 2.2: *Thicknesses of aluminum absorbers for the different energies measured: d1 is the sheet placed between the first and the second scintillator layer of the range telescope.*

gies. From a collection of sheets with thicknesses between 1/16 in (0.16 cm) and 1/2 in (1.27 cm), the absorber is chosen in such a way (see table 2.2) to optimize the particle identification efficiency of the detector for each energy. The absorber thicknesses are determined by a simulation. The chosen values correspond to settings where pions stop dominantly in layer 3 and muons in layer 5. For low channel momenta, pions stop in layer 2 and muons in layer 4.

All photomultiplier tubes are connected to ADCs[3], signals from the first

layer of the telescope are also fed to TDCs[4]. Thus, the available information in this detector is the deposited energy in the individual layers, timing information corresponding to the time of flight of the particles from the beam-defining finger counter to the first layer of the telescope, and with low resolution the range of the particles in the telescope. In addition by using the time difference of the detected signal at the top and bottom of the paddles of the first layer the vertical position of the hit in the paddle can be computed with moderate resolution (see section 3.1.3).
Furthermore the segmentation of the first layer allows the prescaling of events at small scattering angles. A front and side view of the range telescope are shown in figure 2.9.

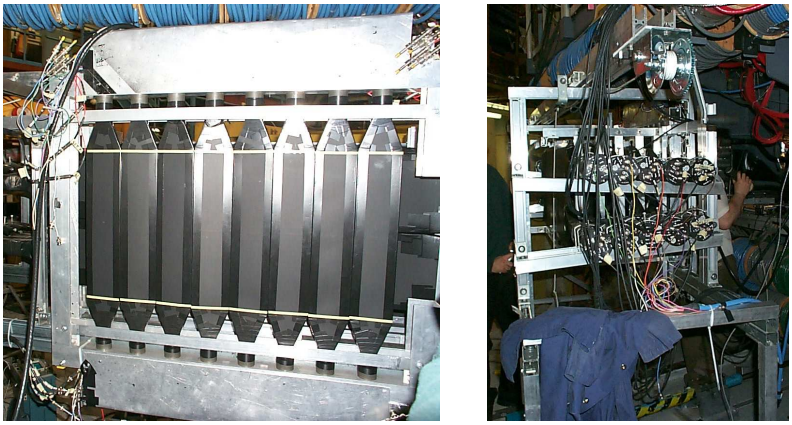

Figure 2.9: *Photographs of the range telescope: the front view shows the first layer which is segmented into 8 vertical paddles, the side view shows the 6 layers and the photomultiplier tubes attached to each of the two bars of layers 2 to 6*

2.4 Target

The target used is a liquid hydrogen (LH_2) target with flat rectangular inner windows. The inner target cell (fig. 2.10) containing the LH_2 has a volume of 80 cm^3 and a thickness of 1.25 cm. It is surrounded by a cell filled with hydrogen gas at the same pressure. This construction ensures that the windows enclosing the liquid stay flat and do not bulge. The hydrogen gas volume is contained in another evacuated cell isolating the cold cell from the outside

[3]Analog to Digital Converters
[4]Time to Digital Converters

atmosphere at room temperature. The foil of the innermost cell is 25 μm thick and glued to a copper target frame. The 2 outer foils are 125 μm thick. The target volume is connected to a tank containing 2 m^3 of hydrogen gas at 16.5 psi (1.14 bar).
The target is cooled by a commercial cooling finger to about 20 K. After filling the target vessel by condensing hydrogen into the target volume, the pressure of the system drops to 16.0 psi (1.10 bar), still slightly above atmospheric pressure. The temperature and phase of the hydrogen in the 2 cells are monitored by resistors and level sensors and controlled by heaters (see appendix D for target schematic drawings).

Figure 2.10: *Photograph of target cell: shown is the inner target cell without the two outer cylindrical windows.*

The target is lowered by an elevator system into the center of the CHAOS detector through the borehole in the top lid of the magnet.
The normal of the target plane is oriented at a nominal angle of -24 degrees with respect to the x-axis of the CHAOS coordinate system (fig. 2.11). At 43.3 MeV, data were also taken with a rotated target at -64 degrees.

2.5 Veto counters

Two veto counters left and right of the finger counter are used to reject beam halo (resulting from particles scattering in the beam pipe tube).

Downstream of the target, a fixed veto and a movable veto scintillator counter are placed at the position where the CFT blocks # 4 and 5 have been removed for the outgoing beam (figs. 2.4, 2.6). The purpose of these veto counters is to prevent triggering on particles detected under small angles

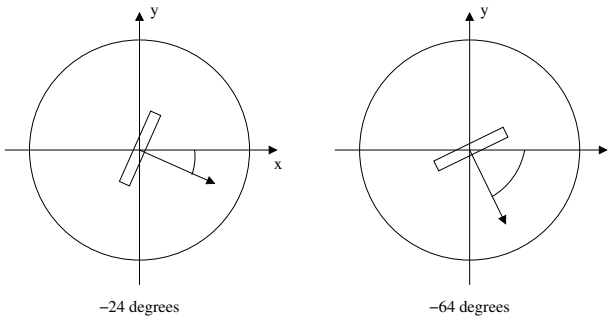

Figure 2.11: *Target angle settings used in the experiment*

which stem from decays of unscattered beam particles behind the target region. The movable veto is adjusted for each energy and charge to optimize the rejection without clipping the acceptance of the range telescope.
The veto circuit includes a gate on the deposited energy in the counter. This gate on the signal height is adjusted so that recoil protons at larger energies do not veto the event.

2.6 Trigger

CHAOS features a sophisticated multi-level trigger system to select the events that are recorded on tape. Up to 3 trigger stages have been used. The first level trigger is a fast trigger only using signals from scintillator counters. The trigger required:

- a hit in the beam-defining finger counter with a beam line time of flight outside the limits for electrons, thus enabling pion and muon beams (see section 3.5.1 and fig. 3.4)
- no valid hit in any of the veto counters
- at least 1 hit in the first layer of the range telescope or the first layer of one of the active CFT blocks

Events hitting the first 3 paddles of the front layer of the range telescope were prescaled if their beam line time of flight signal was within the pion gate. The prescale factors used were about 4 for paddle 1 (the paddle located at the smallest scattering angles) and paddle 2, and 2 for paddle 3. The exact values of the prescale factors are determined by scalers recording both the raw and prescaled rates of the paddles for every run.

The second level trigger (2LT) used information from the 2 innermost wire chambers. It was operated as a rejecting trigger allowing all events except those fulfilling the following conditions:

- exactly 2 hits in the windows defined for the incoming beam in WC2 and WC1
- exactly 2 hits in the windows defined for the outgoing beam in WC1 and WC2

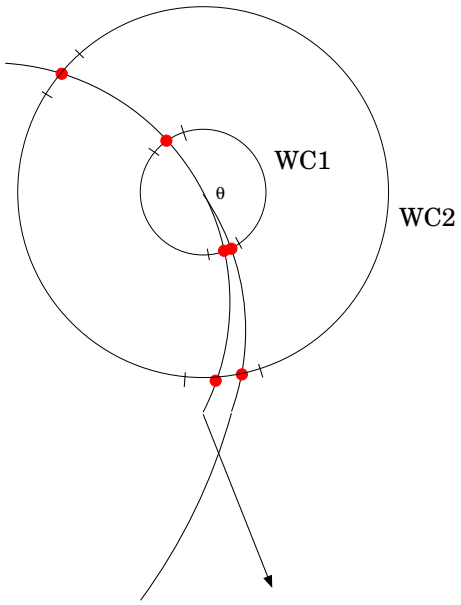

Figure 2.12: *Second level trigger illustration: windows are defined for the incoming and outgoing beam region, events with exactly one hit in each of these 4 windows are rejected.*

For these events, a hit pattern corresponding to tracks with an in-plane scattering angle of less than 2.7 degrees was used to remove the through-going events (fig. 2.13).

In the first beam times of the experiment this trigger level was implemented in MLUs (memory lookup units). After repeated hardware problems with the 2LT trigger stage, for the second half of the beam times the 2LT decision was moved to software and performed by the frontend computer.

For some energies (part of the 32.0 MeV data and 37.1 MeV), a third level trigger in the frontend also rejected decay muons based on very conservative cuts. These cuts removed events with time of flight corresponding to a pion,

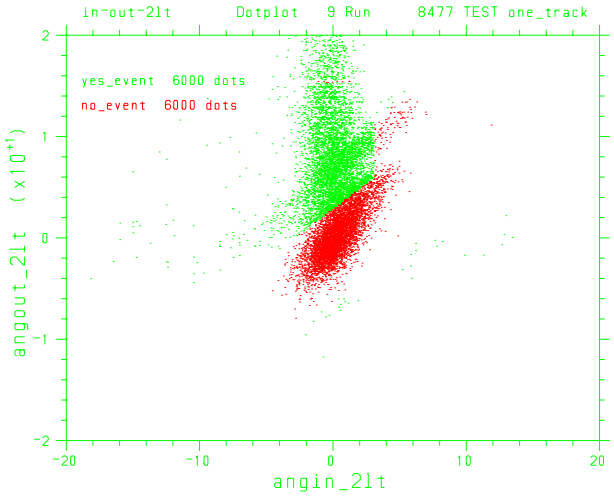

Figure 2.13: *Angles and the second level trigger: shown is the angle of the outgoing track vs. the angle of the incoming track. Accepted events are shown in green, rejected events in red. The trigger rejects events with an in-plane scattering angle of less than 2.7 degrees and also some events with a large in-plane angle which stem from decays before the target region.*

but range and energy loss information in the telescope clearly indicating it was a muon.
To check the performance of the trigger levels and control the trigger decisions, sample events normally not fulfilling the trigger conditions were recorded. For the first level trigger, beam sample events requiring only a hit in the finger counter were recorded. For the second level trigger, samples of rejected events were recorded.

2.7 Readout electronics and data acquisition

The signals of the various detector elements are digitized by CAMAC, FASTBUS, PCOS III and LRS 4290 modules. These modules are read out by a PowerPC-based frontend computer located in the VME crate. The operating system of the frontend is VXWorks. The data are sent via an Ethernet connection to the main data acquisition computer, a PC running Linux and the MIDAS data acquisition software package [MID01]. The data are stored on hard disk and later copied to DLT tapes.
The data acquisition is capable of recording about 1000 events/s with a dead

Time	T_π [MeV]	charge	comments
Spring 1999	43.3	$\pm$	not used (problem with CFT thresholds)
	25.8	$\pm$	not used (problem with CFT thresholds)
Fall 1999	43.3	$\pm$	low statistics
	25.8	$\pm$	
Spring 2000	19.9	$\pm$	
	32.0	$\pm$	
	15.0	$\pm$	not analyzed[5]
	37.1	$\pm$	
Fall 2000	37.1	$\pm$	M11[6]
	57.0	$\pm$	M11
	67.0	$+$	M11 CFT only

Table 2.3: *Overview of beam times and energies*

time of 50 to 60 %. The typical event rate is about 500 events/s with an event size of approximately 1 kB. Scalers are read to determine the beam on the finger counter, the data acquisition lifetime and the prescale factors for the paddles.

In total 183 DLT III tapes holding about 20 GB of data each have been written during the beam times in 1999 and 2000, amounting to a total of 3.5 TB of data.

2.8 Summary of beam times

Table 2.3 gives a summary of the beam times. The data analyzed in this thesis were measured in fall 1999 and spring 2000. The measurements of spring 1999 where repeated in fall 1999 because of an unrecoverable problem with the CFT thresholds. However, very limited time was spent for the 43.3 MeV measurements, therefore these data have significantly larger statistical errors than the other sets.

[5]The acceptance of the detector is too low at this energy.
[6]The data measured at the M11 channel are not part of this thesis.

Chapter 3

Analysis

The aim of the analysis is to extract the differential cross sections from the measured data. The first step is to determine the yield of detected particles. The methods used in the analysis will be described in this chapter. The determination of the acceptance of the detector and the various efficiencies which are needed for an absolute normalization will be discussed in chapter 4.

3.1 Analysis software

Each recorded event is composed of several banks[1]. Each bank contains the information digitized by one type of electronics module (for example the wire chamber hits read by the PCOS[2] system). The purpose of the analysis software is to decode the detector information stored in the bank structure of the event, reconstruct incoming and outgoing tracks from the detector signals and calculate the vertex position and scattering angle. The πp elastic scattering events have to be identified and separated from the background, mostly decays and scattering off structural elements of the detector (wire chamber foils, target pillars etc.)

3.1.1 Track sorting

The incoming track is obtained by fitting a circle with a radius given by the known momentum of the incoming beam to the WC2 and WC1 hits in the incoming beam region.
For reconstructing the outgoing tracks, 2 routines are used. The first one (`tree_sort`) requires hits in all wire chambers to reconstruct a track. It starts with hits in WC1 and tries to find matching hits in the other chambers ligning up with a track. In each step, starting from the angular position

[1]This event substructure is a result of the YBOS memory management package which is used to store and access the events.

[2]system for wire chamber readout made by LeCroy Research Systems

of the hit in the current chamber, the next outward chamber is searched for hits in an angular window allowing for curved tracks. The most probable solutions for tracks are chosen out of the combinatorial possibilities by selecting the tracks with the lowest χ^2 in a fit.
The hits which are not associated with tracks in this routine are passed to the second track finding routine (`sort_left_overs`). This routine requires hits in only 3 out of 4 chambers to reconstruct a track. It starts with the WC4 hits (this chamber has 8 signal wires and thus an efficiency of close to 100 %) and works its way inwards. If it does not find a connecting hit in a chamber, it will skip to the next inward chamber.
Combining these routines has two advantages. The efficiencies of WC1, WC2 and WC3 can be determined by looking at all tracks and determining the fraction of 3-hit and 4-hit tracks (see 4.3.1). In addition the track reconstruction efficiency is increased by also using the `sort_left_overs` routine. For a more detailed discussion of CHAOS track sorting see [Hof97].

3.1.2 Vertex routines

The vertices are constructed as intersections between outgoing tracks and the incoming track. Since the recoil proton usually does not receive enough recoil energy to leave the liquid hydrogen target, only the vertex reconstructed from the scattered pion track is considered in the analysis.
There are two different approaches to find the intersection. The first one, which was used in previous CHAOS experiments, calculates the intersection between the circles fitted to incoming and outgoing tracks. This method is feasible as long as the incoming and outgoing track are not nearly parallel.
For small scattering angles (less than 17 degrees) a different algorithm is used. It introduces a virtual target plane placed in the middle of the flat, boxlike target cell and calculates the intersection of the incoming and outgoing tracks with this plane. This ensures that there are always two intersections. The in-plane scattering angle is then calculated from the difference of the two intersection angles. Thus the algorithm does not provide a vertex position. However, the distance of the two intersection points on the plane (see fig. 3.1) is a measure of the distance of the true vertex from the plane (called `sepr` for separation in the analysis software). By applying cuts on this quantity events with vertices within the target can be selected. A detailed description of the beam-target-intersection algorithm can be found in [Jam99].
The distribution of reconstructed vertices in the x-y plane for events detected with the CFT blocks is shown in figure 3.2. The resolution is good enough to resolve the cylindrical outer windows of the target.

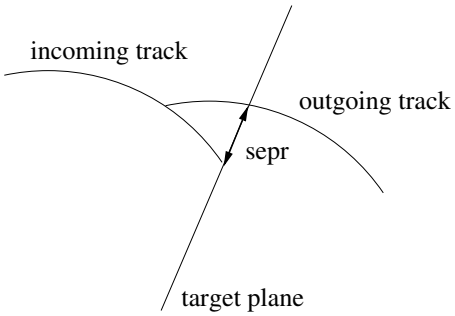

Figure 3.1: *Illustration of the* `sepr` *cut: for small scattering angles the separation of intersection points in the target plane is used as a measure of the distance of the vertex from the target plane.*

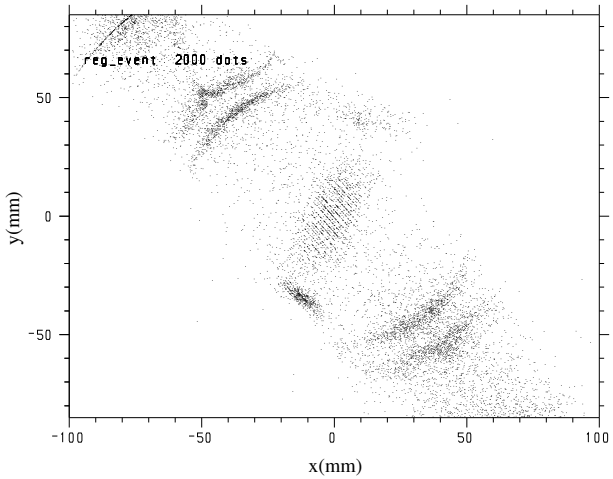

Figure 3.2: *Position of reconstructed vertices: The liquid hydrogen in the inner target cell is clearly visible, also the copper pillars of the target support structure and the outer windows of the target cell in the incoming and outgoing beam region.*

3.1.3 Scattering angle

The routines mentioned so far only calculate the in-plane (2-dimensional) scattering angle in the scattering plane defined by the CHAOS acceptance. For larger scattering angles, the out-of-plane acceptance of ± 7 degrees of CHAOS results in a negligible correction of the full (3-dimensional) scattering angle. However, at small in-plane angles (less than 17 degrees) the out-of-plane component has to be taken into account.
The out-of-plane angle is calculated by fitting two lines (incoming/outgoing track, 4 parameters) to the available z-information. This information is pro-

vided by the beam-defining finger counter, the cathode strips of the first 2 wire chambers, the resistive wires in WC4 and the first layer of the range telescope:

- *beam-defining finger counter:* A particle has to hit this detector to trigger the recording of the event. $\sigma_{\text{finger}} = 30$ mm, determined by tracing the incoming track to the position of the finger counter and looking at the z distribution.

- *WC2/WC1 incoming track z information:* The tilted cathode strips of the two inner chambers provide an information about the height at which a particle is passing through the chamber. The resolution is determined by the width of the cathode strips (4 mm for WC2 and 2 mm for WC1).

- *intersection of incoming and outgoing track in target:* In the analysis only events with an intersection of the incoming and the outgoing track in the target volume are selected. Therefore the intersection of the out-of-plane component of the incoming and outgoing track is also forced onto the target plane. The spread of the distribution is determined from the distribution of the `sepr` quantity. $\sigma_{\texttt{sepr}} = 3$ mm, which translates into a resolution of 17 mm for an event with 10 degrees in-plane scattering angle. The algorithm is used for in-plane scattering angles of less than 17 degrees, therefore the error for the vertex position is set to 20 mm.

- *WC1/WC2 outgoing track z information:* tilted cathode strips, same as for the incoming track

- *WC4 z information:* The vector drift chamber WC4 also contains 2 resistive wires. By measuring the charge at the top and bottom end of these wires, a z position can be determined. The resolution of the wires is set to $\sigma_{\text{RW}} = 30$ mm.

- *range telescope:* The z position is obtained from the TDC difference of top and bottom photomultiplier in the first layer of the range telescope. The error is set to $\sigma_{\text{RT}} = 50$ mm.

To be able to determine the z parameters of the tracks, 4 out of these 9 quantities have to be present, which is fulfilled for virtually all events.
The optimal parameters are determined by doing a least-square fit to the z information (see fig 3.3). In case the χ^2 of the fit is very high, a refitting without the range telescope information is attempted. This is necessary

because for some events the TDC information from the telescope cannot be used, for example when one of the 2 TDCs is missing. The full scattering

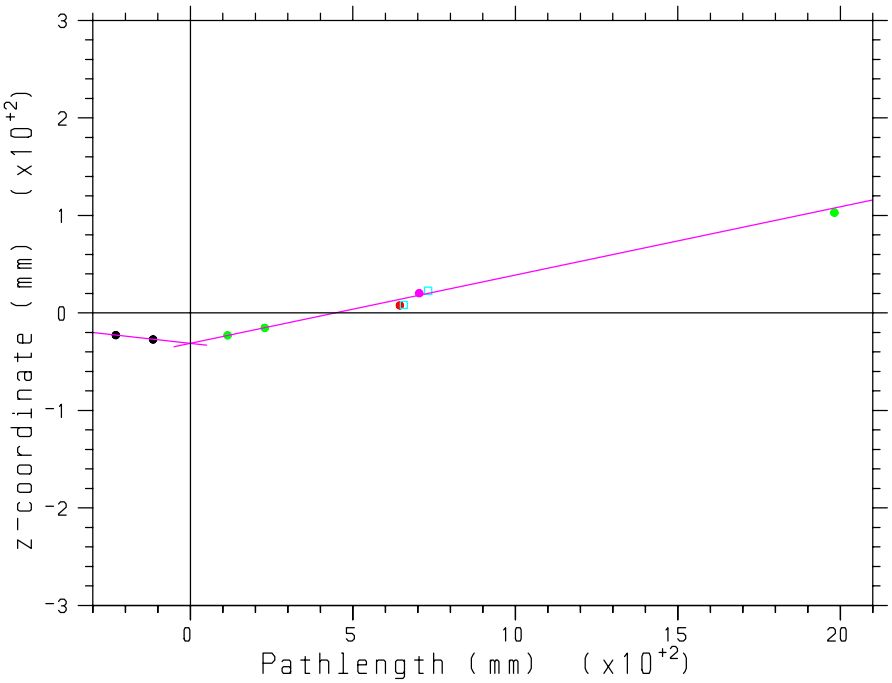

Figure 3.3: *Example of available z information and out-of-plane angle reconstruction. The finger counter requirement is not shown in the plot.*

angle is then calculated from the in- and out-of-plane angle components for events using the beam-target intersection algorithm.

3.2 Calibration

The calibration factors (TDC offsets, Lorentz angles, drift velocities, etc.) for the drift chambers (WC3 and WC4) and the CFT blocks are based on [Hof97]. Here only the calibration of the range telescope is discussed.
For this detector, the gains of the ADCs and the timing of the TDCs have to be properly corrected. This is done in the following way:

- *ADCs:* The photomultiplier signals of all scintillator layers are digitized by ADCs. To correct for different gains in the photomultipliers, these ADCs have to be calibrated. The calibration factors are obtained by looking at the signal of the electrons in training runs. In these runs,

the beam is steered directly onto the range telescope. Electrons are not stopped in the detector and pass through all layers. The momentum of these electrons is given by the channel momentum. Therefore they deposit a well-defined energy in each of the scintillator layers. These peaks are moved to channel 100 for the calibrated ADCs. In the analysis the 2 signals for each paddle of the first layer of the range telescope are summed to obtain the summed ADC for each paddle. For layers # 2 to 6, the 4 ADCs digitizing the signal of the 4 photomultipliers of each layer are summed.

- *TOF and position:* The timing information for the signals of the first layer of the range telescope is also recorded with TDCs. The TDCs are not directly calibrated. Instead the TOF (arithmetic mean of the TDCs of a paddle) and position information (obtained from the difference of the TDCs) are shifted. The TOF is set to be the same for all paddles, the shifts are determined from muon data recorded in the training runs. The position offset is determined from training data and data obtained in the reaction $\pi^+ \mathrm{d} \rightarrow \mathrm{pp}$.

3.3 Skimming

In a first analysis pass ("skimming") the amount of data is reduced by a factor of 10 by applying "soft" cuts. The data are separated into 2 data sets. Events with at least one track and a hit in the range telescope are stored in the range telescope data set, events with at least one track except those that consist of exactly one track with a two-dimensional scattering angle in the forward-angle region are stored in the CFT region data set. Events with exactly one track and a very small 2-dimensional scattering angle (cutoff at 3.2 or 3.6 degrees depending on energy) are removed. For the range telescope data, obvious decay events (based on the momentum of the particle) are removed.

3.4 Parallelization

A major technical problem in the analysis is the speed with which events can be processed. On one standard PC (e.g. using an AMD Athlon XP 1600+ processor) approximately 200 - 400 events/s can be analyzed. Since the total amount of data after the skimming still is about 500 GB or 500 million events, one analysis pass would take about 20 days. To overcome this problem, the analysis is set up in a way that each run is analyzed on

one of 15 available PCs. The distribution of tasks to computers which are not occupied by other jobs is achieved by submitting the tasks to a load management tool (Sun Grid Engine [Gen01]).

3.5 Selection of pion-proton scattering events

To select the elastically scattered pions in the measured data, cuts are applied in the analysis. Some of these cuts are used for all scattering angles, some only apply to the events detected by CFT blocks, and some only to the events detected by the range telescope. These cuts will be discussed in the following sections.

3.5.1 Common cuts

The cuts mentioned in this section are applied to both the events detected by the CFT blocks and the range telescope. The events are required to be trigger events with a pion TOF. Noise events due to noise in the finger counters are removed. The outgoing track has to originate from the target region, and the wire chamber hits chosen for the track have to align well to the resulting fit. The following cuts are used:

event type: Only trigger events (not beam sample events) are selected.

pion TOF: The incoming beam particles are identified as pions by time of flight in the channel (fig 3.4). The time measured is the timing difference between the signal from the finger counter and a signal of the capacitive probe (`tcap`) in the primary beam line which gives the timing of the proton bunches.

finger ADC noise: Noise in the finger counters (see fig 3.5) at very low ADC values is removed. This cut is set individually for each of the two finger counter ADCs.

target intersection cut: `rproj` is the position of the intersection of the incoming track with the target plane. This quantity shows the distribution of the beam on the target (fig. 3.6). Only the central region of the target cell is selected, and the pillar regions are removed.

cut perpendicular to the target plane: This cut restricts the data to events with a vertex in the target area (cutting away events that scattered in WC1 etc.). The cut depends on the algorithm used for the

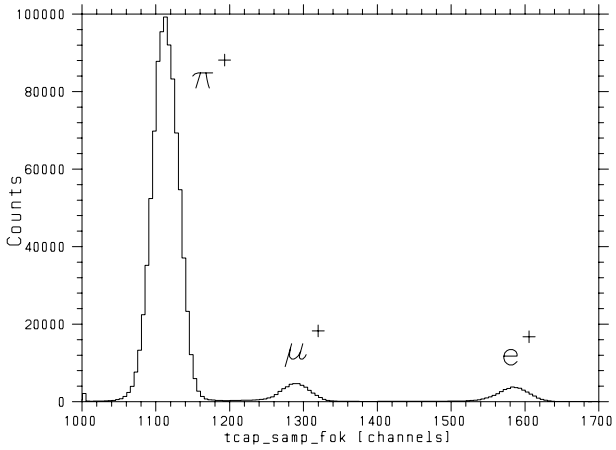

Figure 3.4: *Time of flight spectrum of beam particles measured at 32.0 MeV, positive charge: the different particle types can be clearly identified.*

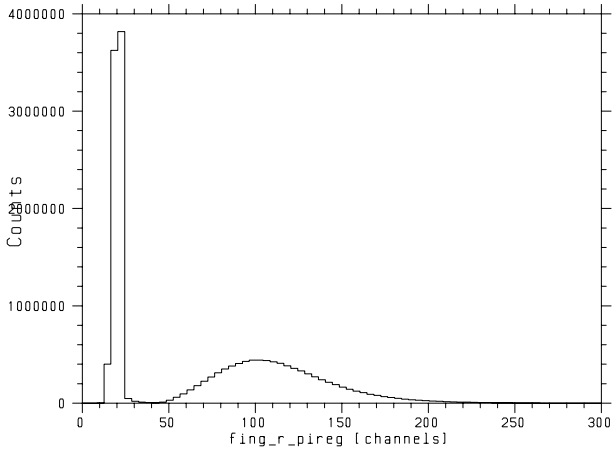

Figure 3.5: *Right finger ADC spectrum at 32.0 MeV, positive charge: the noise spike is removed by applying a cut at channel 55.*

vertex and scattering angle determination. For in-plane scattering angles of more than 17 degrees, the circle-circle intersection is used, and the distance (`verl`) between the vertex and the target plane is used for the cut. For smaller scattering angles, the beam-target-intersection algorithm is used, and the cut is done on the separation (`sepr`) of the incoming and the outgoing intersection point on the target plane.

good χ^2 for track fit: The requirement of a decent fit of the wire chamber hits to the reconstructed track removes tracks with non-aligned hits

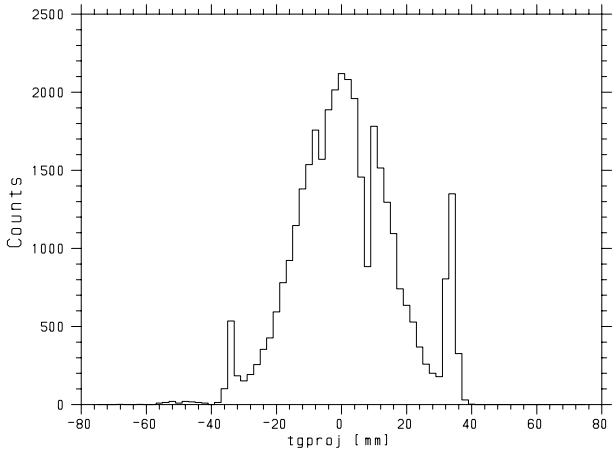

Figure 3.6: *Beam profile on target (32.0 MeV, positive charge): the distribution of pions scattered under 10 degrees on the target plane is shown. The events scattering off the pillars visible to the right and left of the Gaussian peak are removed by a cut. The shape of the Gaussian is affected by inefficiencies of the wire chambers.*

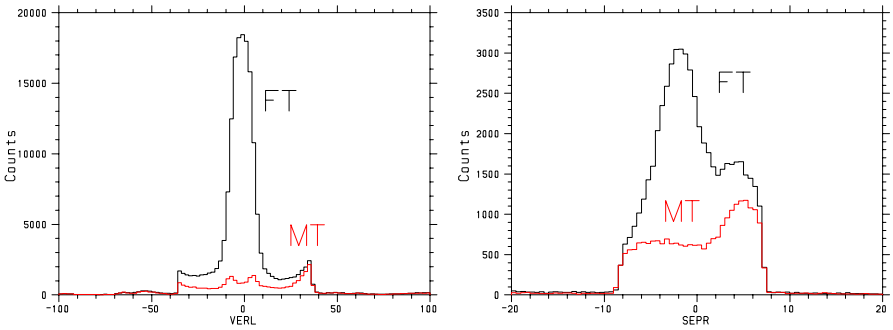

Figure 3.7: *Example of* `verl` *and* `sepr` *distributions at 32.0 MeV, positive charge: the data measured with full target (FT) are depicted in black, the data measured with empty target (MT) in red. The data are not normalized, the* `verl` *plot is generated with large angle scattering data, for the* `sepr` *plot only pions scattered around 10 degrees are plotted.*

(kinks) that are due to decays.

3.5.2 CFT region

In addition, for the data measured by the CFT blocks, a hit in a CFT is required. The event has to fulfill elastic pion-proton scattering kinematics

and has to be identified as a pion in the CFT blocks. This is achieved by the following conditions:

CFT scintillator hit: Check if the track has a CFT hit (signal in the first layer of the CFT block) in the corresponding active CFT region (blocks # 7 to 17)

momentum vs. scattering angle: Particles scattered according to pion-proton elastic scattering kinematics are identified by a two-dimensional box cut. The cut removes background scattering off heavier elements and also some decay events (fig. 3.8).

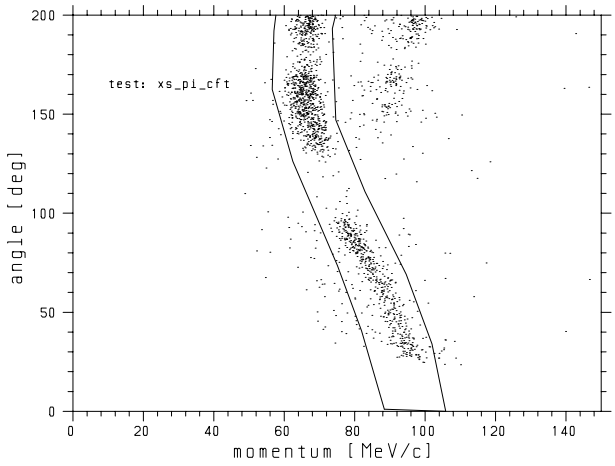

Figure 3.8: *Kinematic selection of events in angle-vs.-momentum plane (32.0 MeV, positive charge)*

pion particle identification: The particle is identified as pion in a two-dimensional box cut using the correlation between the deposited energy in the first scintillator layer DE1 of a CFT block and the momentum of the track (fig. 3.9).

3.5.3 Range telescope region

For particles detected in the range telescope, in addition to the common cuts described in section 3.5.1 the particle has to hit the telescope, the track has to hit the first layer of the range telescope in the paddle corresponding to the intersection of the extrapolated track and the first layer, the event has to fulfill elastic pion-proton scattering kinematics, and the particle hitting the telescope has to be identified as pion by the neural network:

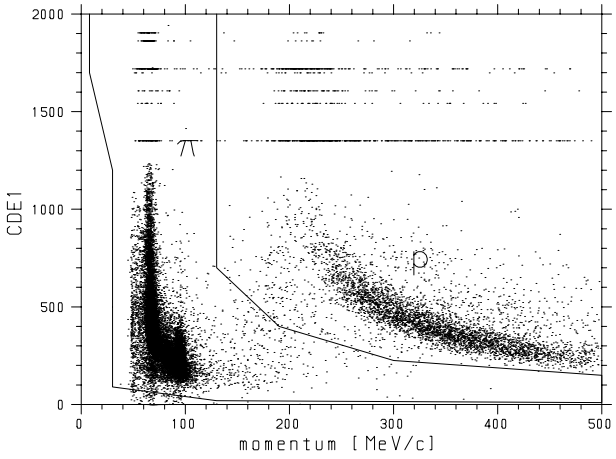

Figure 3.9: *Identification of pions in the DE1 vs. momentum plane (32.0 MeV, positive charge): the pions are selected with a wide box. Shown are events hitting CFT blocks # 7 to 17. The horizontal lines at higher ADC values are the overflows for several CFT blocks which are moved to differently calibrated ADC values by the calibration factors.*

range telescope hit: A coincidence of signals from the top and the bottom photomultiplier in at least one of the 8 scintillators of the first layer is required.

track extrapolation: The track extrapolated from WC4 has to hit the corresponding paddle of the range telescope. The cuts are adjusted to muon proton scattering data measured simultaneously because for this reaction there is no decay background and each paddle shows a nice peak in the intersection position histogram (fig 3.10). One cut is used for all energies, the limits for the single paddles are shown in table 3.1. The cuts accept a 18 cm wide window for each 10 cm wide paddle. This cut removes part of the decay events with decays occurring after the pion passed wire chamber 4.

tight χ^2 cut: A tighter version of the χ^2 cut, removes decay events which have a kink in their track.

momentum: The measured momentum of the track is modified by taking into account πp elastic scattering kinematics, i.e. the hypothetical beam momentum for the event assuming elastic πp scattering is calculated. This allows to use a one-dimensional cut selecting the same momentum range for all scattered pions instead of a box in the angle-

paddle number	low[mm]	high[mm]
1	-386.5	-106.5
2	-282.5	-2.5
3	-178.5	61.5
4	-74.5	165.5
5	29.5	269.5
6	133.5	373.5
7	237.5	477.5
8	341.5	581.5

Table 3.1: *Cuts used for the extrapolated intersection of the track with the first layer of the range telescope*

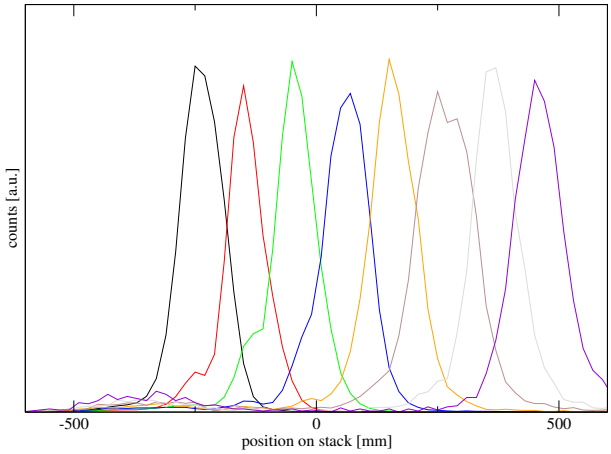

Figure 3.10: *Extrapolated intersection with range telescope (32.0 MeV, positive charge): the point of intersection of the track extrapolated from WC4 and the first layer of the range telescope is plotted for scattered muons. Shown are 8 peaks corresponding to hits in the 8 vertical scintillator bars of the first layer.*

momentum-plane. An example for the virtual beam momentum distribution of detected particles is shown in fig. 3.11.

response from neural network: particle identification (π/μ) according to neural network (see section 3.5.4). The range telescope provides crucial additional information to suppress background in the forward scattering angle region (fig. 3.12). The background due to muons from decays in the region affected most by the muon cone is 50 to 100 times

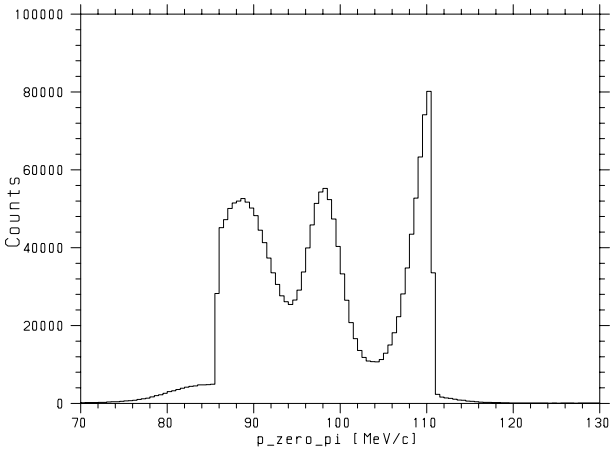

Figure 3.11: *Momentum distribution of scattered pions, corrected for kinematics (32.0 MeV, positive charge): the central peak is due to elastically scattered pions, the peaks at the left and right are remaining muon background events due to pion decays into muons in the target region which are misidentified as pions by the neural network.*

larger than the signal of scattered pions.

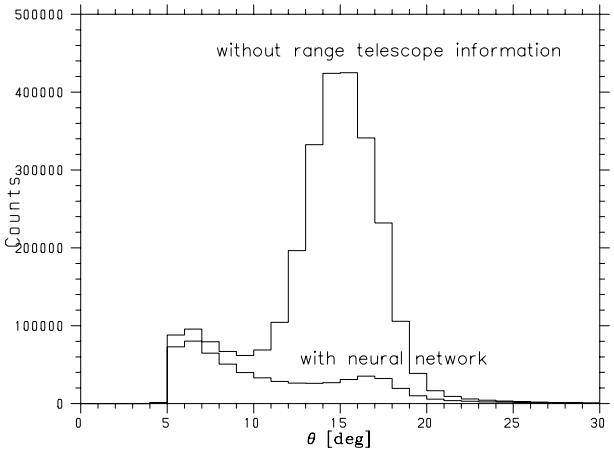

Figure 3.12: *Illustration of background suppression with the neural network (32.0 MeV, positive charge): Shown are events identified as πp scattering events by the CHAOS chamber information (upper graph) and the events remaining after using the range telescope information and the neural network decision (lower graph). For this illustration the histograms for the single paddles are summed without taking the correct pre-scale factors into account.*

3.5.4 Neural network

For the particle identification in the small scattering angle region a neural network code [Odo96] is used.

3.5.4.1 Principle

A feed forward neural network configuration with backward propagation in the training procedure is used for the classification of events. The concept of a neural network [Rum86] is motivated by our knowledge of the working and structure of the human brain and how information is propagated and processed in it. This is accomplished by a vast number of cells (neurons), which are interconnected. The main features of a neuron are:

- It receives input signals (impulses) from other neurons through its dendrites.
- The input signals are modified (enhanced or inhibited) by synapses.
- If the summed modified input signals exceed a threshold, the nerve cell is excited and fires (an output signal is generated).
- This output signal is propagated to other neurons via the axon.

This biological system is abstracted in neural networks in the following way: Each neuron has several input channels x_i. These inputs are modified by weights w_i and then summed. If the excitation exceeds a threshold s, the neuron "fires", i.e. provides a signal y at the output channel. This binary output is usually smoothed by a transfer function f, in this case $f = tanh(x)$ is used.

$$y = f(\sum_i w_i x_i - s)$$

The neural network used in the analysis is a feed-forward neural network consisting of 3 layers.
The available information (ADC values for the single layers, range of the particle in the telescope (number of layers passed by the particle), TOF from finger counter to first layer of telescope) are fed to 8 neurons in the first (input) layer. The neurons in this layer do not possess weights or thresholds. They are just used to distribute the inputs to the second (hidden) layer. This layer consists of 4 neurons, and the particle identification result is given by the output signal of a single neuron in the last layer.

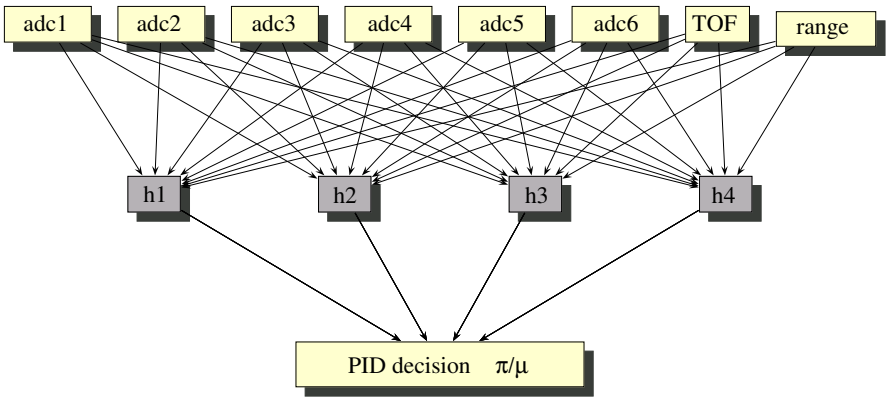

Figure 3.13: *Topology of neural network: the network used is a feed-forward network with 3 layers. The input layer is formed by 8 neurons corresponding to the number of inputs, the hidden layer (h1 - h4) consists of 4 neurons, and the response of the network is given by a single neuron in the last layer.*

3.5.4.2 Training procedure

To set the weights and thresholds of the neurons in the second and third layer, the neural net has to be "trained". Samples of pion and muon events (training data) are presented to the network, and in an iterative procedure the coefficients of the network are adjusted by backward propagation until an optimal identification of the 2 sample classes is reached.
To obtain the training data, special training runs have been recorded in the experiment. In these runs the magnetic field of the spectrometer was used to steer the beam directly onto the paddles of the range telescope. For each paddle, each energy and each charge training data at 3 different channel momenta corresponding to the nominal momentum in the experiment for the energy and this momentum plus and minus 4 % have been taken.
The pions and muons for the training are identified by their time of flight from the production target to the finger counter. The track of each event is extrapolated to the first layer of the telescope, and only tracks hitting the correct paddle (tracks without a kink due to decays) are used for the training. In addition, events where only one of the 2 TDCs for the paddle is present are discarded.
For the muon samples the time of flight of the particles from the finger counter to the telescope has to be corrected to reflect the situation in the actual experiment. Both pions and muons have the same momentum determined by the channel setting. However the mass of the muon is smaller than the mass of the pion, therefore the velocity of the muon is higher. Muons from

pion decays in the target region with a momentum similar to the channel momentum have a larger time of flight than muons from the channel. This difference stems from the fact that they are still pions on their way from the finger counter to the target region and therefore are traveling slower on that part of the trajectory.

The TDCs used have a resolution of 20 channels per ns. The corrections

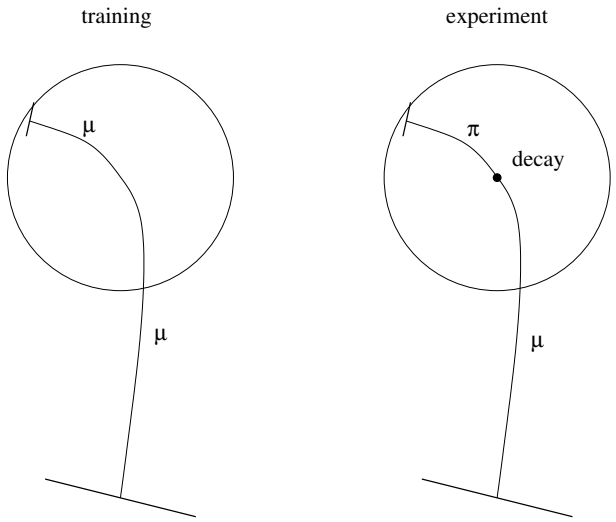

Figure 3.14: *Illustration of different time of flight for muons in the training runs and real data: in the training runs, muons from the channel are used, thus the particle type from the beam-defining finger counter to the first layer of the telescope is always a muon. This situation is different in the experimental data: Pions from the channel decay into muons in the target region and are detected in the range telescope. Therefore the time of flight has to be corrected for the different flight time for muons and pions from the finger counter to the target.*

given by the different inverse velocities of pions and muons for the flight path of 76.8 cm are given in table 3.2.

The samples are cleaned (events with 2 or more paddles hit in the first layer of the detector are removed). For each particle type the samples for the 3 different momentum settings are mixed and then the two classes are presented to the neural network. In the training procedure, the pion sample s_π and the muon sample s_μ are divided in two subsamples t and c of equal size. With the training subsamples t_π and t_μ the coefficients of the neurons are adjusted. This is achieved by minimizing the difference between true particle type and particle ID response from the neural network. With the

T_π [MeV]	correction [channels]
43.3	10.3
37.1	11.5
32.0	13.2
25.8	15.4
19.9	18.3

Table 3.2: *Corrections for muon time of flight measured in the training runs*

T_π [MeV]	charge	ϵ_π	ϵ_μ
43.3	+	0.950	0.983
43.3	-	0.948	0.981
37.1	+	0.968	0.991
37.1	-	0.946	0.984
32.0	+	0.946	0.990
32.0	-	0.954	0.989
25.8	+	0.962	0.980
25.8	-	0.963	0.979
19.9[1]	+	0.986	0.987
19.9[1]	-	0.987	0.990

Table 3.3: *Particle identification efficiency of the neural network judged by the control samples in the training: ϵ_π is the fraction of pion samples identified as pions, ϵ_μ the fraction of muon samples identified as muons.*

control subsamples c_π and c_μ the efficiency of the particle identification is checked.
This procedure is repeated until the PID efficiency converges.

3.5.4.3 Efficiency

The efficiency of the particle identification as judged by the control samples is given in table 3.3. At 19.9 MeV only training data for the central momentum are used, since the other 2 data sets were accidentally clipped by hardware vetoes (electron veto and muon tcap cut).
Although these values are an indication of the performance of the neural network, they do not necessarily reflect the true PID efficiency in the experiment, since the samples might not be fully representative for the pions and muons from pion decays in the experimental situation. However, by train-

[1] training at 19.9 MeV done only with central momentum setting training data

ing the neural network with samples at 3 different momenta, the momentum range in which the muon background is efficiently suppressed is extended.

3.5.5 Background subtraction

After applying the cuts discussed in sections 3.5.1, 3.5.2 and 3.5.3, there is still some background left. One major source is the background from scattering off the thin innermost target foils of the liquid hydrogen vessel. These foils cannot be removed by a vertex cut because they are not resolved from the LH_2 volume. The second source of background are muons from pion decays in the target region which are misidentified as pions by the neural network. For this reason, data with an empty target have also been taken. The normalized yield obtained from empty target runs is subtracted from the normalized yield obtained from the full target data. If the background to foreground ratio is larger than 0.4, the angular bin is removed from the analysis, because the background correction becomes too large to still be reliable. This only happens at forward angles in the area where the muon cone hits the range telescope (see figure 3.15).

3.6 Selection of muon-proton scattering events

The differential cross sections for $\mu^{\pm}$p elastic scattering are simultaneously measured with the pion data. Since the μp cross sections drop very steeply with angle, a measurement with meaningful statistical accuracy is only feasible at forward angles, in the region covered by the range telescope.
The measured cross sections give a cross check of the normalization and understanding of the analysis at forward angles. The problems in reconstructing scattered muons are very similar to the analysis of pion-proton scattering events, but there is no background from decays.

Most of the cuts used to extract the yield are the same as in the πp analysis:

- event type (trigger event)
- finger ADC noise cut
- vertex cuts (`sepr` and `verl`)
- `rproj` cut
- range telescope hit

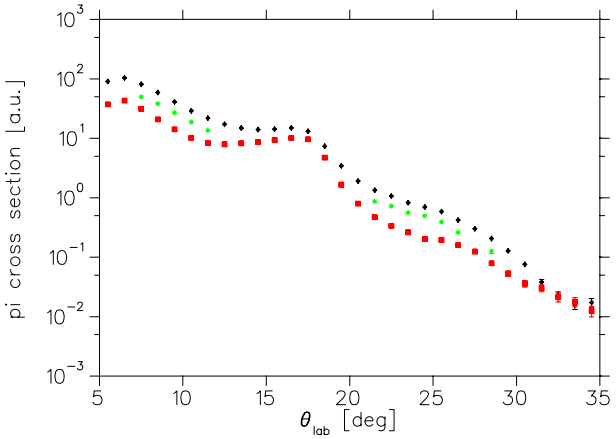

Figure 3.15: *Background subtraction at forward angles (32.0 MeV, positive charge): the black data points are data measured with a full target, the red data points data measured with an empty target. The background-subtracted data are shown in green points. The data are not normalized to a realistic acceptance, but to a constant geometric acceptance of 0.0036 sr for each 1 degree bin. The bump-like structure around 18 degrees is due to remaining events which stem from decays in the target region. If the background to foreground ratio is larger than 0.4, the angular bin is removed from the analysis. Therefore there is a hole in the green distribution in the region affected most by decays.*

- tight χ^2 cut

The following cuts are different:

muon time of flight: To select the muons in the beam, a muon time of flight from the production target to the finger counter is required.

momentum: The measured momentum is also extrapolated to 0 degrees, but a wide cut assuming μp kinematics is applied.

one track: Requiring exactly one outgoing track is a safe cut at forward angles, there is no danger of rejecting good two-track events with a muon scattered at backward angles and a proton detected at forward angles in μp scattering.

range cut: The first layer of the range telescope is used as a veto layer for these events. Scattered muons never stop in this layer.

The following cuts are not applied because they are specifically targeting pion decays:

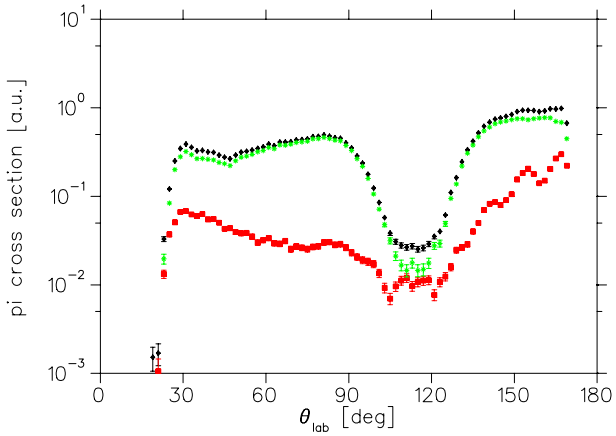

Figure 3.16: *Background subtraction at larger angles (32.0 MeV, positive charge): the black data points are data measured with a full target, the red data points data measured with an empty target. The background-subtracted data are shown in green points. The data are not normalized to a realistic acceptance, but to a constant geometric acceptance of 0.0085 sr/2 deg. The hole seen around 120 degrees is due to the copper target pillar shadowing this region.*

- track extrapolation to range telescope
- response from neural network

Chapter 4

Normalization

4.1 Introduction

To determine the absolute differential cross sections $\frac{d\sigma(\theta)}{d\Omega}$, the measured yield $Y(\theta)$ has to be normalized:

$$\frac{d\sigma(\theta)}{d\Omega} = \frac{Y(\theta)}{N_{beam} N_{target} f_\pi \epsilon_{DAQ} \epsilon_{WC} \epsilon_{decay} d\Omega_{eff}}$$

where

N_{beam}: number of incident beam particles

N_{target}: number of target atoms per unit area

f_π: fraction of pions in beam

ϵ_{DAQ}: life-time of data acquisition

ϵ_{WC}: wire chamber efficiencies

ϵ_{decay}: corrections for pion decay

$d\Omega_{eff}$: effective solid angle

The number of incident particles N_{beam} is taken from the recorded scaler values. It is corrected by the fraction of the beam hitting the target in the central region as defined by the `rproj` cut (see fig. 3.6).
The number of target atoms per unit area N_{target} projected into the plane normal to the beam is calculated from the target thickness d, the target angle β (angle between target normal and beam direction in the target) and the density ρ of the liquid hydrogen given by the temperature of the liquid. m_H is the mass of a hydrogen atom.

$$N_{target} = \frac{\rho * d}{m_H cos(\beta)} = \frac{72.9\text{mg/cm}^3 * 1.25\text{cm}}{1.673 * 10^{-21}\text{mg} cos(\beta)} = 5.447 * 10^{-5} \frac{1}{\text{mb}} \frac{1}{cos(\beta)}$$

The density of the LH_2 is looked up for the measured target temperature of 19.1 K.

The fraction of pions in the beam f_π is determined from beam sample events using the time of flight of the particles from the production target to the finger counter (see fig. 3.4).
The data acquisition lifetime ϵ_{DAQ} is monitored by scalers which count the number of events passed to the second level trigger circuit and the number of events fulfilling the first level trigger requirements.
The wire chamber efficiencies are determined from detected events as described in section 4.3.1.
ϵ_{decay} is a correction for pion decays before the target. It consists of 2 parts. The first part (ϵ_{dc_u}) corrects for the decay of pions into muons right before the finger counter. If these muons hit the finger counter, they are misidentified and counted as pions due to their pion time of flight in the beam line. The second part (ϵ_{dc_d}) is a correction for decays of pions into muons on the way from the finger counter to the target. The decays of scattered particles are treated in the effective solid angle $d\Omega_{eff}$. Some additional corrections are discussed in section 4.4.
$d\Omega_{eff}$ is calculated using Monte-Carlo simulations.

4.2 Acceptance simulations

The effective solid angle $d\Omega_{eff}$ is determined by a GEANT[1] Monte-Carlo simulation based on the CERN[2] GEANT3 package. To get a reliable effective solid angle that reflects the acceptance in the experiment, the simulation has to reflect the true experimental conditions as closely as possible.
A full model of the detector is included in the simulation (fig. 4.1). Particles are generated with a Gaussian distribution in the position, angle and momentum in a region of the beam pipe close to the beam pipe exit, traced to the target, undergo a reaction (elastic scattering) in the sensitive volume describing the LH_2 target, and the outgoing particles are tracked. Energy loss in the detector material and possible decays are considered. In sensitive detector elements (e.g. wire chambers, scintillators) the corresponding detector signals are generated, and the signals generated by the events are written to disk. Trigger conditions can be set so that only events that produce a hit in a CFT block or the first layer of the range telescope are recorded.

The reaction mechanism in the target volume is either pion-proton elas-

[1] GEometry ANd Tracking

[2] Conseil Européen pour la Recherche Nucléaire: European Organisation for Nuclear Research

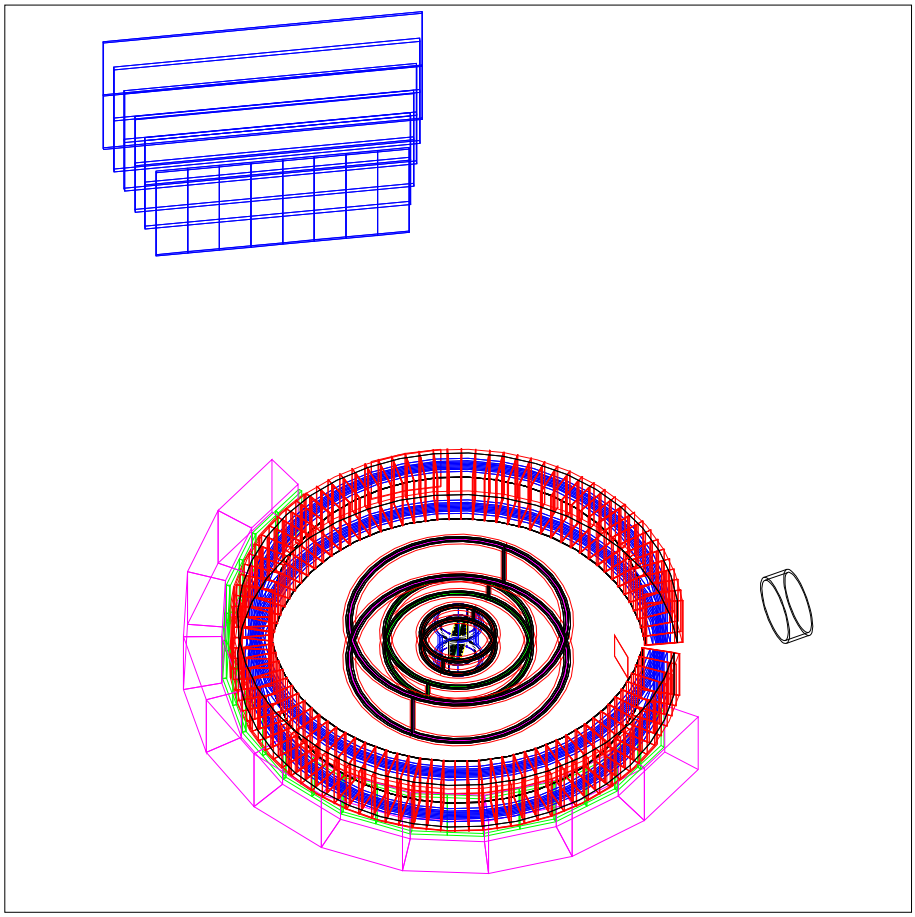

Figure 4.1: *Visualization of the experimental setup as implemented in the GEANT simulation*

tic scattering or muon-proton elastic scattering. Events can be generated in a subset of the phase space.This is typically done limiting the out-of-plane angle to values between $-15°$ and $+15°$, since the CHAOS out-of-plane acceptance is very limited anyway. It is also possible to generate events with an angular distribution according to realistic cross sections. This is used to determine the acceptance at small scattering angles weighted by the very steep differential cross sections.
The generated events are then analyzed by the same analysis software as the real experimental data, and the acceptance is determined from the fraction of reconstructed events to generated events.

4.2.1 GEANT input parameters

The parameters describing the beam, the range telescope position and the rotation of the LH_2 target have been varied in the simulations to match the experimental conditions.

4.2.1.1 Beam parameters

For each energy and charge, the following parameters have been optimized to get a good description of the experimental beam conditions in the GEANT simulation:

angle of generation `KINE(4)`**:** this parameter varies the angle of generation of particles at the beam pipe exit in the CHAOS plane.

CHAOS rotation `EXP1(2)`**:** defines the rotation of the detector with respect to the beam pipe. A change of this parameter is equivalent to moving the beam position in the beam pipe.

CHAOS field `BFLD`**:** magnetic field of the detector

To assess the agreement between experiment and simulation for the beam definition, the position of the through-going beam on the first two wire chambers, the curvature of the track, the intersection angle of the beam with the target and the beam profile on the target plane are used (fig. 4.2). There is good agreement between the simulation and the experimental data in all quantities.

4.2.1.2 Range telescope position

The distance of the range telescope from the center of the CHAOS detector is set to the value of 192.20 cm which was measured during the experiment. The determination of the angular position and rotation of the range telescope with respect to CHAOS have been improved by looking at the calculated intersection point of the track with the front layer of the range telescope for μp scattering data detected with one of the 8 paddles of the telescope. In the GEANT simulation, the generator for the μp scattering data uses calculated μp cross sections for the distribution of the scattering angles. This ensures that the steeply falling cross sections are taken into account. The position of the range telescope used in the simulation is found to be in good agreement with the experimental data when using the following parameters: `EXP1(5)`=-98.27 (rotation of of the range telescope around its center), `EXP1(6)`=192.20 (distance from the center), `EXP1(7)`=-88.62 (rotation of the range telescope around the CHAOS center).

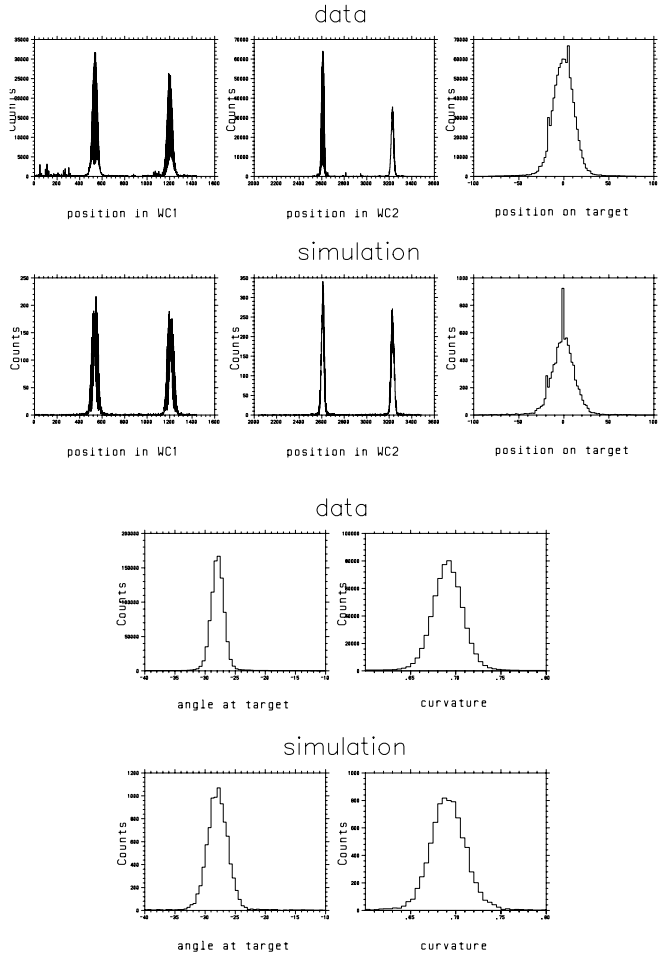

Figure 4.2: *Example of tuning beam parameters (37.1 MeV, positive charge): the first and third line depict measured data, the second and fourth line the results of a GEANT simulation. The histograms shown in the first two lines are (from left to right) the wire numbers in WC1, the wire numbers in WC2 and the beam profile on the target plane, shown in the third and fourth line are histograms of the angle between the beam at target plane intersection and the target normal and a measure of the curvature of the track.*

4.2.1.3 Target rotation

The nominal target rotation (orientation of the target plane normal vector to the x-axis in the CHAOS coordinate system) is -24 degrees (fig. 2.11) (and -64 degrees for a second set of measurements at 43.3 MeV). However, the hole in the effective solid angle due to the target pillars obtained with this acceptance does not match the hole observed in the data of the experiment.

After a variation of various target parameters, an optimal description of the experimental acceptance is found to be a target angle of -28 degrees, the outer pillar of the target rotated by -6 degrees (see fig. 4.3) and an offset of the target vessel along the target plane normal of 3 mm [Mei02]. Similarly, for the data measured at a nominal target rotation of -64 degrees a target angle of -68 degrees is used.

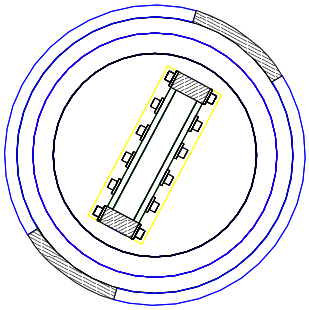

Figure 4.3: *Illustration of target pillars: The target vessel is shown in a top view, the target pillars are hatched. The outer pillars of the target support structure are rotated by -6 degrees with respect to the inner pillars and the target cell.*

4.2.2 Realistic implementation of the detector geometry

Modifications have been made to the detector geometry in the simulation to describe the acceptance observed in the experiment. Especially for the acceptance at 19.9 MeV incident pion energy various checks have been made trying to determine the effects of structural elements on the acceptance in the GEANT simulation. A hole in the acceptance is seen at all energies when looking at the intersection point of the outgoing track with the first layer of the scintillator (see figure 4.4):

tilted DE1 scintillator: the hole seen in fig. 4.4 lies near 315° between the CFT blocks # 7 and 8 and is due to a displaced scintillator. After the experiment this scintillator was found to be shifted and tilted with respect to its neighbors, leaving a triangular gap between blocks # 7 and 8. The width of the hole in the simulation is set to be 1 degree which matches the effect seen in the data. For the 19.9 MeV data there is also a hole visible between blocks # 8 and 9. Therefore a hole with the same dimension was included in the simulation.

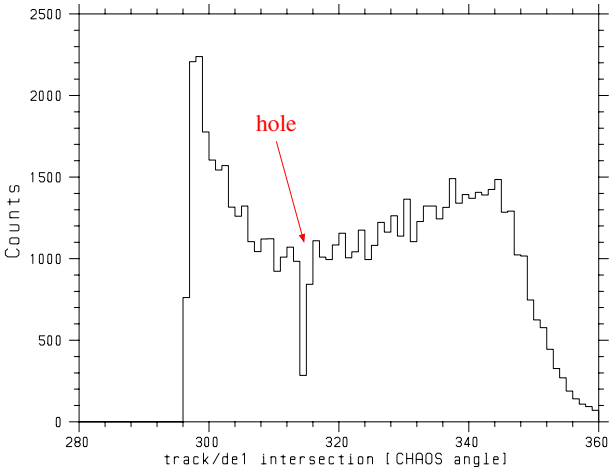

Figure 4.4: *Intersection of outgoing tracks with the first scintillator layer (DE1) of the CFT blocks (at 25.8 MeV, positive charge) measured as angle in a polar coordinate system. Clearly visible is a hole which is due to a displaced DE1 scintillator.*

In addition, at low energies many effects which where not important in previous CHAOS experiments could affect the acceptance of the detector. The following checks and modifications have been introduced to investigate possible effects:

radial support structure of WC4: Wire Chamber 4 is built of cells which are repeated every 3.6 degrees. The vertical support structure consists of a 2 mm thick rib of Rohacell[3] extending from r=59.75 cm to r=68.55 cm, the back of the C-shaped clamp of G10[4] holding the Rohacell from r=68.55 cm to r=69.75 cm, and the G10 spine glued to the back wall extending from 69.75 cm to 71.25 cm (see fig. 4.5). Since WC4 is built in sections of 36 degrees (10 cells) and 54 degrees (15 cells), at the junction of 2 sections (CHAOS angle 0, 36, 90, 126, 180, 216, 270, 306 degrees relative to the x-axis) 2 ribs are placed.

The inclusion of this support structure leads to a significant reduction of 25 % of the acceptance at 19.9 MeV for the backward scattering events. The effects of the changes are shown in reconstructed events of a GEANT acceptance simulation (fig. 4.6).

variation of glue layer thickness: The windows of the wire chambers consist of 1 mm thick Rohacell layers which are sandwiched between a

[3]polymethacrylimide (PMI) hard foam made by Röhm Performance Plastics
[4]glass epoxy laminate

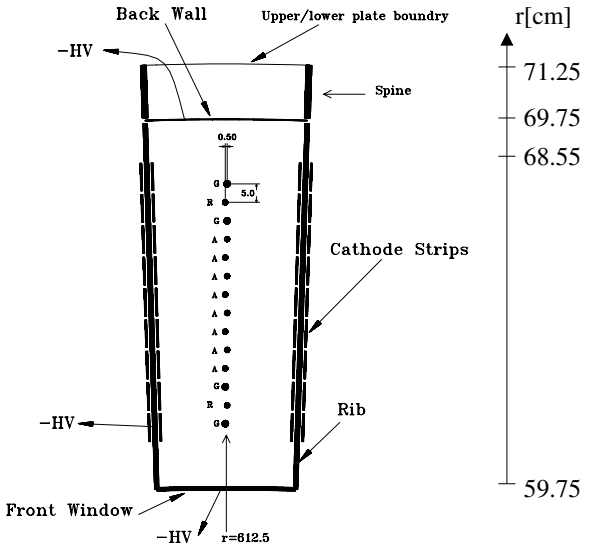

Figure 4.5: *Illustration of a WC4 cell. The chamber is built of such cells with an angular spacing of 3.6 degrees. The radial support structure (rib, spine) has to be included in the simulation to account for the loss in acceptance at low energies.*

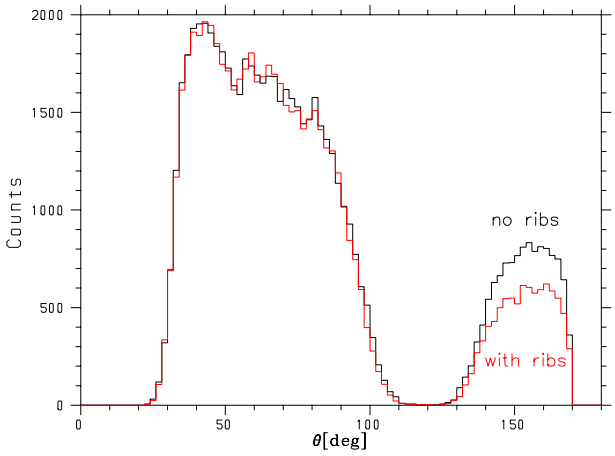

Figure 4.6: *Effect of ribs on GEANT acceptance at 19.9 MeV, positive charge: reconstructed events without radial support structure (black) and with the ribs and spines (red). The acceptance at backward angles is reduced by 25 %.*

mylar window on the outside and a Copper-plated kapton foil on the inside. These materials are already included in the simulation. The foils are glued to the Rohacell. The glue was not included in the simulation up to now, and a particle is crossing about 15 layers of glue while passing through the detector. Thus the effect of these glue layers on the acceptance was studied. Each glue layer was estimated to be around 10 μm thick [Ama03], simulations have been performed with layer thicknesses of 0, 10 and 20 μm. The acceptance at 19.9 MeV at backward angles changes by about 3 % between each of these thicknesses. For the final acceptance simulations, a value of 10 μm was chosen for the glue layers.

variation of rib and spine thickness: To determine the effect of an uncertainty in the rib and spine thickness of the radial support structure of WC4, the thickness was changed by a factor of 1.5 and 2.0. The corresponding drop in acceptance at 19.9 MeV is 10 % for the first modification and another 2 % for the second modification. The rib and spine thickness for the acceptance simulations was kept at the original value.

variation of spine length: For completeness, the effect of a variation of the length of the spine glued to the back wall of wire chamber 4 was also studied. The spine was extended by up to 2 cm, however the resulting change in the acceptance was only of the order of 3 %. Finally, the design value for the spine length was used in the simulation.

4.2.3 Veto counter position

The movable veto used in the experiment is also included in the GEANT simulation. It has exactly the same dimensions and is placed like a DE1 scintillator, but at an adjustable polar angle δ (measured counterclockwise from the y-axis of the CHAOS coordinate system, 180 degrees means positioned exactly as the DE1 scintillator of missing block number 5, see fig. 4.7). Since the position of the movable veto counter has been adjusted for each energy and charge during data taking, the counter position is adjusted in the simulation by looking at very forward angle muon proton scattering data. If the muon cross section drops below the theoretical calculation at very forward angles, the counter position is shifted anticlockwise to cut into the acceptance until the muon cross sections are corrected to the theoretical values. In case there is no visible effect of a veto in the data, the veto is not used in the simulation. The results of this procedure are summarized in

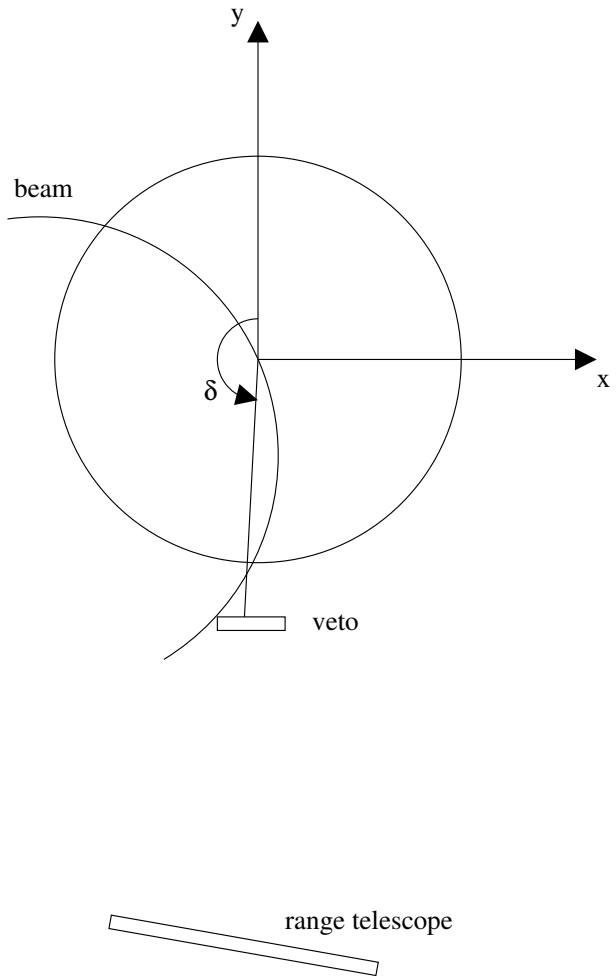

Figure 4.7: *Illustration of veto counter position*

table 4.1.

In the experiment the veto is suppressed for events with a high energy deposition in the counter. These events correspond to forward-scattered protons leaving the target when a pion is scattered into the backward angle region and only occur at higher energies and in the π^+p case. To account for this in the simulation, the pion acceptance at backward angles is determined without using the downstream veto counters.

T_π [MeV]	charge	veto position δ [deg]
43.3	+	none
43.3	-	177
37.1	+	178
37.1	-	178
32.0	+	178
32.0	-	179
25.8	+	177
25.8	-	176
19.9	+	none
19.9	-	none

Table 4.1: *Veto counter position δ used in the simulation: Note that the veto position is measured relative to the y-axis of the CHAOS coordinate system.*

4.2.4 Acceptance results

4.2.4.1 Acceptance for pion-proton elastic scattering in the CFT region

To determine the acceptance, events are generated in a region close to the beam pipe exit and tracked to the detector. If the incoming pion hits the liquid hydrogen volume, a scattered pion is generated by the event generator. As mentioned above, for the CFT region a phase space distribution is assumed, i.e. the distribution of the pions in the center of mass frame which is used in the event generator is isotropic.
The effective solid angle is then given by

$$\Delta\Omega_{eff}(\theta) = \frac{Y_A(\theta)}{Y_G(\theta)}\Delta\Omega_{MC}(\theta)$$

where θ is the real scattering angle (including out-of-plane components), $Y_A(\theta)$ the number of events reconstructed in the analysis, $Y_G(\theta)$ the number of events generated in the sensitive target volume, and $\Delta\Omega_{MC}(\theta)$ the geometric solid angle into which the events are generated. In the absence of additional constraints, this geometric solid angle is

$$\Delta\Omega_{MC}(\theta) = 2\pi sin\theta\Delta\theta.$$

An integration of this function over the scattering angle θ gives the full solid angle of 4π.

However, since the geometric out-of-plane acceptance of the CHAOS detector is ± 7 degrees, this distribution is clipped arbitrarily at out-of-plane

angles of ±15 degrees in the laboratory system to save computing time. Therefore in the region where the out-of-plane angle can be larger than 15 degrees (for $15^\circ < \theta < 165^\circ$) the geometric solid angle $\Delta\Omega_{MC}(\theta)$ used in the generation of events is modified to

$$\Delta\Omega_{MC}(\theta) = 2sin\theta\Delta\theta(\pi - 2arccos(\frac{sin15^\circ}{sin\theta})).$$

This function is depicted in the upper left graph of fig. 4.8.

Since $\Delta\Omega_{MC}(\theta)$ is the solid angle of generation in the laboratory system, and $Y_G(\theta)$ are the events generated isotropically in the center of mass system, the connection between the two functions is given by the Jacobian $J(\theta)$ for the transformation from the laboratory system to the center of mass system:

$$\frac{\Delta\Omega_{MC}(\theta)}{Y_G(\theta)} = k \cdot J(\theta)$$

with k being a normalization factor depending only on the number of generated events. k is determined by fitting the Jacobian to the fraction in the left hand side of the last equation. Then in the formula for the effective solid angle $\Delta\Omega_{MC}(\theta)/Y_G(\theta)$ can be replaced by $k \cdot J(\theta)$:

$$\Delta\Omega_{eff}(\theta) = Y_A(\theta) \cdot k \cdot J(\theta)$$

The advantage of this method over directly using the fraction $\frac{Y_A(\theta)}{Y_G(\theta)}\Delta\Omega_{MC}(\theta)$ is that artifacts generated by the non-smooth behavior of the Monte-Carlo solid angle are removed by this procedure [Wro01].
The method is illustrated in fig. 4.8: In the upper left plot the Monte Carlo window function $\Delta\Omega_{MC}(\theta)$ is shown. The upper right graph depicts the distribution of generated events $Y_G(\theta)$ in the laboratory system. The lower left plot shows the Jacobian obtained by dividing $\Delta\Omega_{MC}(\theta)$ by $Y_G(\theta)$. The spikes at 15 and 165 degrees are artifacts caused by the non-smooth behavior of $\Delta\Omega_{MC}(\theta)$ at these angles due to the clipping procedure. The lower right graph shows the calculated Jacobian function, the constant k is obtained by fitting this function to the lower left graph.

An example of the normalization procedure is shown in fig. 4.9. The effective solid angle $\Delta\Omega_{eff}(\theta)$ of the experiment (upper right plot) is determined from the reconstructed events $Y_A(\theta)$ (upper left plot) that have been generated by a GEANT simulation and have passed the cuts in the analysis. The yield normalized by all other factors (e.g. target density, beam, efficiencies) except the effective solid angle (lower left plot) is normalized by the

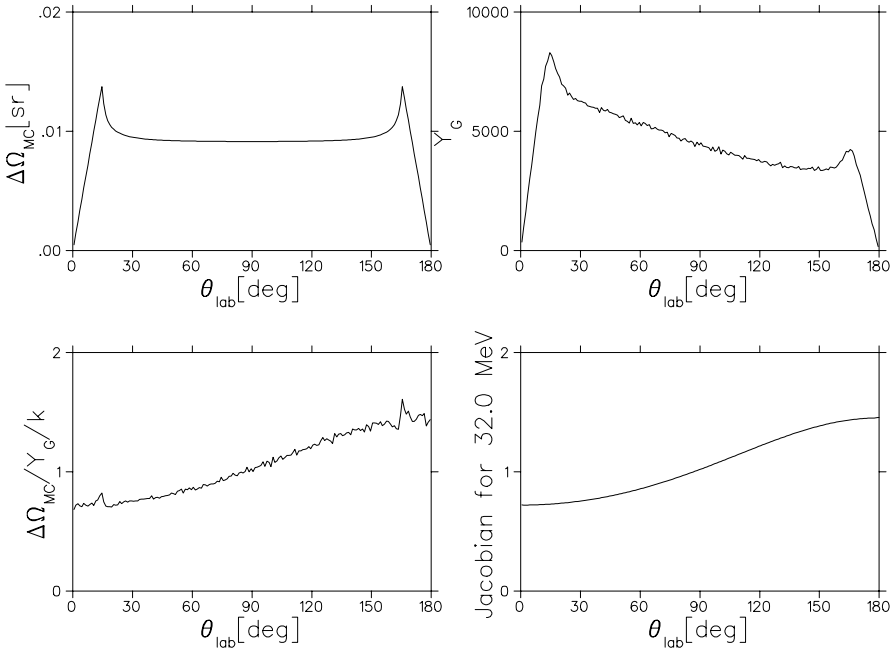

Figure 4.8: *Illustration of solid angle and Jacobian in the simulation:* upper left: *Monte Carlo window* $\Delta\Omega_{MC}(\theta)$, upper right: *distribution of generated events* $Y_G(\theta)$, lower left: *Jacobian obtained from the simulation (note the artifacts at 15 and 165 degrees),* lower right: *calculated Jacobian. The pictures are taken from a simulation at 32.0 MeV kinetic energy.*

effective solid angle, the resulting normalized cross sections $\frac{d\sigma(\theta)}{d\Omega}$ are depicted in the lower right plot.

The acceptance of the experiment is energy-dependent. It is significantly reduced due to decay and absorption at low energies and backward angles (fig. 4.10).

4.2.4.2 Acceptance for pion-proton elastic scattering in the range telescope region

The acceptance for pion-proton elastic scattering for the small scattering angle region covered by the range telescope is determined by a procedure similar to the case described in 4.2.4.1. Since the cross sections drop steeply in this region, the acceptance is determined taking into account the effects of varying cross sections. Instead of clipping the event generation at larger out-of-plane angles, events are only generated with a scattering angle θ of 5 to 35 degrees. The angular distribution of events is chosen according to cross

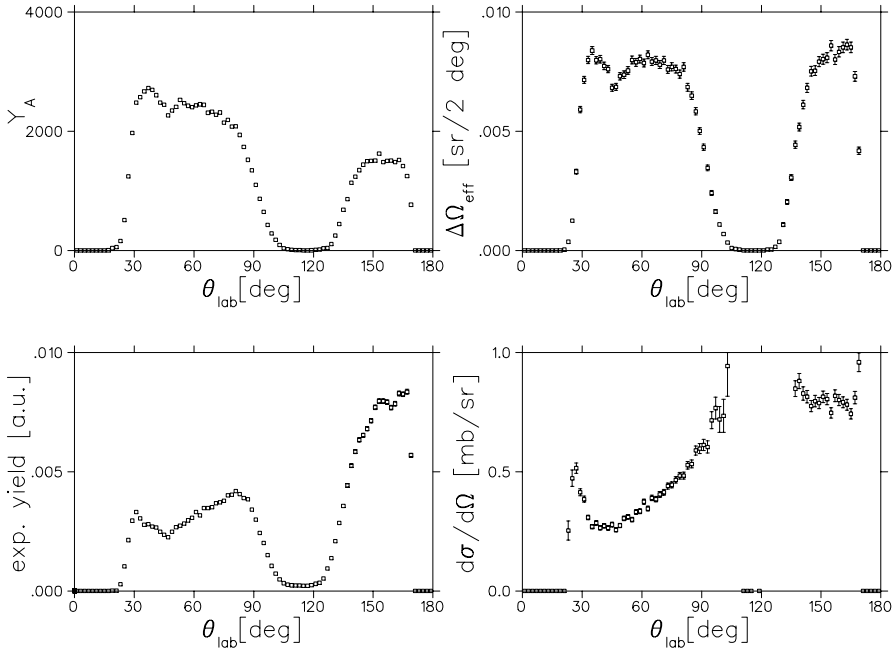

Figure 4.9: *Normalization procedure (32.0 MeV, positive charge): from the reconstructed events Y_A (upper-left plot) the effective solid angle $\Delta\Omega_{eff}(\theta)$ is calculated. This solid angle describes the CHAOS acceptance for detecting events with a scattering angle θ and is shown in the upper-right plot. With the solid angle, the yield can be normalized. The semi-normalized experimental yield is shown in the lower-left plot. The factors for target density, incident beam etc. have already been applied to the yield, however it is not yet corrected for the acceptance of the detector. The cross sections after the correction with the CHAOS acceptance $\Delta\Omega_{eff}$ are shown in the lower-right plot.*

sections taken from the SAID phase shift analysis [Arn02]. The effective solid angle is then calculated by

$$\Delta\Omega_{eff}(\theta) = \frac{Y_A(\theta)}{Y_G(\theta)}\Delta\Omega_{MC}(\theta)$$

with

$$\Delta\Omega_{MC}(\theta) = 2\pi sin\theta\Delta\theta$$

4.2.4.3 Acceptance for muon-proton elastic scattering

The acceptance for muon-proton elastic scattering is determined by a procedure similar to the pion case described in the previous section. However,

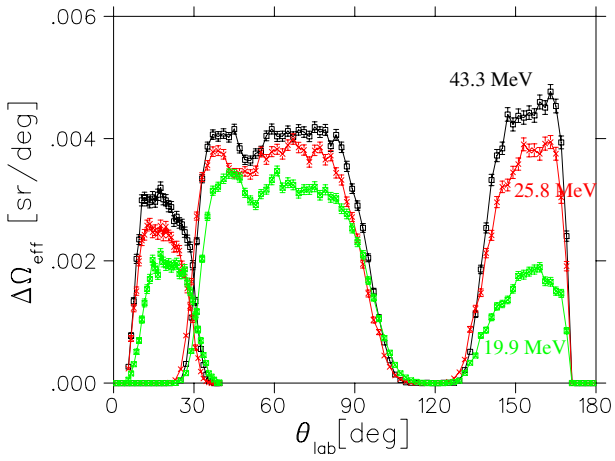

Figure 4.10: *Effective solid angle $\Delta\Omega_{eff}(\theta)$ for 3 energies at positive charge: Shown in black is the acceptance for 43.3 MeV, in red the acceptance for 25.8 MeV and in green the acceptance for 19.9 MeV. The first curve for angles up to 35 degrees gives the acceptance for the data measured with the range telescope, the second curve the acceptance for the data measured with the CFT blocks. The hole in the second curve around 120 degrees is due to the target pillars shadowing this region.*

calculated muon cross sections [Pok98] for the corresponding muon momenta in the middle of the target cell are used for the angular distribution of events.

4.2.5 Corrections to the GEANT acceptance

The GEANT acceptance obtained as described in 4.2.4.1 and 4.2.4.3 has to be corrected for the `rproj` cut which is applied. In the analysis of the simulated events an `rproj` cut is used, restricting good events to the central region of the target. However in the normalization of the experimental yield this cut is already corrected for by multiplying the number of incoming beam particles with the fraction of beam particles hitting the target in the region defined by the `rproj` cut. Therefore the GEANT acceptance has to be corrected for the number of particles generated within the gates of the `rproj` cut divided by the number of particles generated in the sensitive volume. This is done in two steps:

inverse `rproj` cut: The fraction f_1 of incoming beam events inside the gates of the `rproj` cut divided by the fraction of total incoming beam events in the simulation is determined (fig. 4.11).

sensitive volume cut: The incident beam particles are generated in a spot at the beam pipe exit. Not all incident beam particles pass through the sensitive volume where the event generator creates scattered tracks. The fraction f_2 is the number of incoming beam particles hitting the sensitive volume and triggering the generation of a scattered track divided by the number of incoming beam particles. For the pions this correction is determined without decay processes enabled in the simulation.

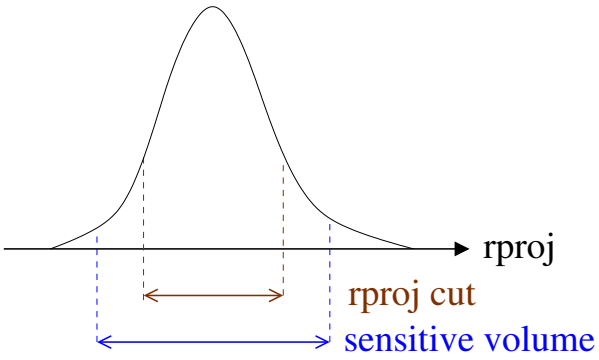

Figure 4.11: *Illustration of the corrections due to the limited sensitive volume and the* `rproj` *cut. Shown is the beam profile on the target. The effect of the* `rproj` *cut (brown) in the reconstruction of GEANT events has to be undone, taking into account the limited sensitive volume (blue) in which scattered tracks are generated.*

The correction which is applied to the GEANT acceptance to remove the effect of the `rproj` cut is then f_1/f_2.

4.3 Efficiencies

Corrections due to inefficient wire chambers and dead time of the data acquisition system have to be applied in the normalization process.

4.3.1 Chamber efficiencies

The chamber efficiencies are determined directly from measured data. The efficiencies of WC2 and WC1 for the incoming track are determined by using beam sample events. These events only require a hit in the finger counter to be recorded. For beam sample events with a least 3 hits in the 4 windows defining the incoming region for WC2 and WC1 and the outgoing region for

T_π [MeV]	charge	target	ϵ_{WC1i}	ϵ_{WC2i}
43.3	+	full	0.9984	0.8771
43.3	+	empty	0.9973	0.8890
43.3	-	full	0.9976	0.9387
43.3	-	empty	0.9966	0.9386
43.3	+	-64 deg., full	0.9982	0.9363
43.3	+	-64 deg., empty	0.9975	0.8897
43.3	-	-64 deg., full	0.9982	0.9363
43.3	-	-64 deg., empty	0.9970	0.9480
37.1	+	full	0.9979	0.9961
37.1	+	empty	0.9981	0.9963
37.1	-	full	0.9978	0.9965
37.1	-	empty	0.9978	0.9966
32.0	+	full	0.9973	0.8641
32.0	+	empty	0.9968	0.8517
32.0	-	full	0.9968	0.9296
32.0	-	empty	0.9963	0.9155
25.8	+	full	0.9971	0.8234
25.8	+	empty	0.9973	0.8155
25.8	-	full	0.9969	0.9196
25.8	-	empty	0.9965	0.9186
19.9	+	full	0.9970	0.9605
19.9	+	empty	0.9970	0.9938
19.9	-	full	0.9961	0.9652
19.9	-	empty	0.9962	0.9926

Table 4.2: *Wire chamber efficiencies for the incoming beam: the efficiency of wire chamber 2 is lower because it had some dead wires in the incoming beam region region. The chamber was repaired during the experiment, which improved the efficiency significantly.*

WC1 and WC2, a through-going track is fitted to the hits. Thus, in case of an inefficient chamber, the location of the missing hit can be calculated. The efficiencies ϵ_{WC2i} and ϵ_{WC1i} of WC2 and WC1 in the incoming beam region are then given by the fraction of detected hits in the window divided by the number of expected hits in the window (see table 4.2).

The efficiencies of the first 3 chambers for the outgoing tracks can be determined separately for each angular bin. Since the sort-leftover track finding routine only requires 3 out of 4 hits and chamber 4 consists of 8 separate wires and thus is assumed to be 100 % efficient, the fraction of tracks containing a hit in a chamber divided by the total number of tracks for each

angular bin yields an angle-resolved wire chamber efficiency ϵ_{WC1}, ϵ_{WC2} or ϵ_{WC3} for the corresponding chamber. The total wire chamber efficiency for the track can then be calculated [Wro01] as:

$$\begin{aligned}\epsilon_{track} &= \epsilon_{WC1}\epsilon_{WC2}\epsilon_{WC3} + \epsilon_{WC1}\epsilon_{WC2}(1-\epsilon_{WC3}) + \epsilon_{WC1}(1-\epsilon_{WC2})\epsilon_{WC3} \\ &\quad +(1-\epsilon_{WC1})\epsilon_{WC2}\epsilon_{WC3} \\ &= \epsilon_{WC1}\epsilon_{WC2} + \epsilon_{WC1}\epsilon_{WC3} + \epsilon_{WC2}\epsilon_{WC3} - 2\epsilon_{WC1}\epsilon_{WC2}\epsilon_{WC3}\end{aligned}$$

The resulting efficiencies for the outgoing track are shown in fig. 4.12. The efficiency is always larger than 0.97.

4.3.2 DAQ lifetime

The lifetime of the data acquisition system is determined from the fraction of events passed to the second level trigger circuit (`passed_events`) divided by the number of events fulfilling the first level trigger requirements (`dmo.por`). These two numbers are recorded in scalers for each run during the experiment. The lifetime is less than 1 because the data acquisition and acceptance of the second level trigger are blocked while reading out an event. Since beam sample events are only taken when the data acquisition is not busy and thus always accepted by the trigger logic, the lifetime is computed as:

$$\epsilon_{DAQ} = \frac{\texttt{passed\_events} - \texttt{beam\_samples}}{\texttt{dmo.por} - \texttt{beam\_samples}}$$

Typical lifetimes range between 0.4 and 0.7, depending on the energy and the beam rate used in the measurement.

4.3.3 Neural network detection efficiency

The πp scattering data measured with the range telescope have to be corrected for the efficiency ϵ_π with which the pions are identified by the neural network. The efficiency is determined from the particle identification results for control samples c_π in the training (see table 3.3). The average efficiency (excluding the results for 19.9 MeV since the training samples there are only at one momentum) is $\epsilon_\pi = 0.955$. Therefore, the pion yield measured with the range telescope is corrected by this factor.

4.4 Other corrections

In addition, the decay of pions right in front of the finger counter and between the finger counter and the target region is not included in the GEANT

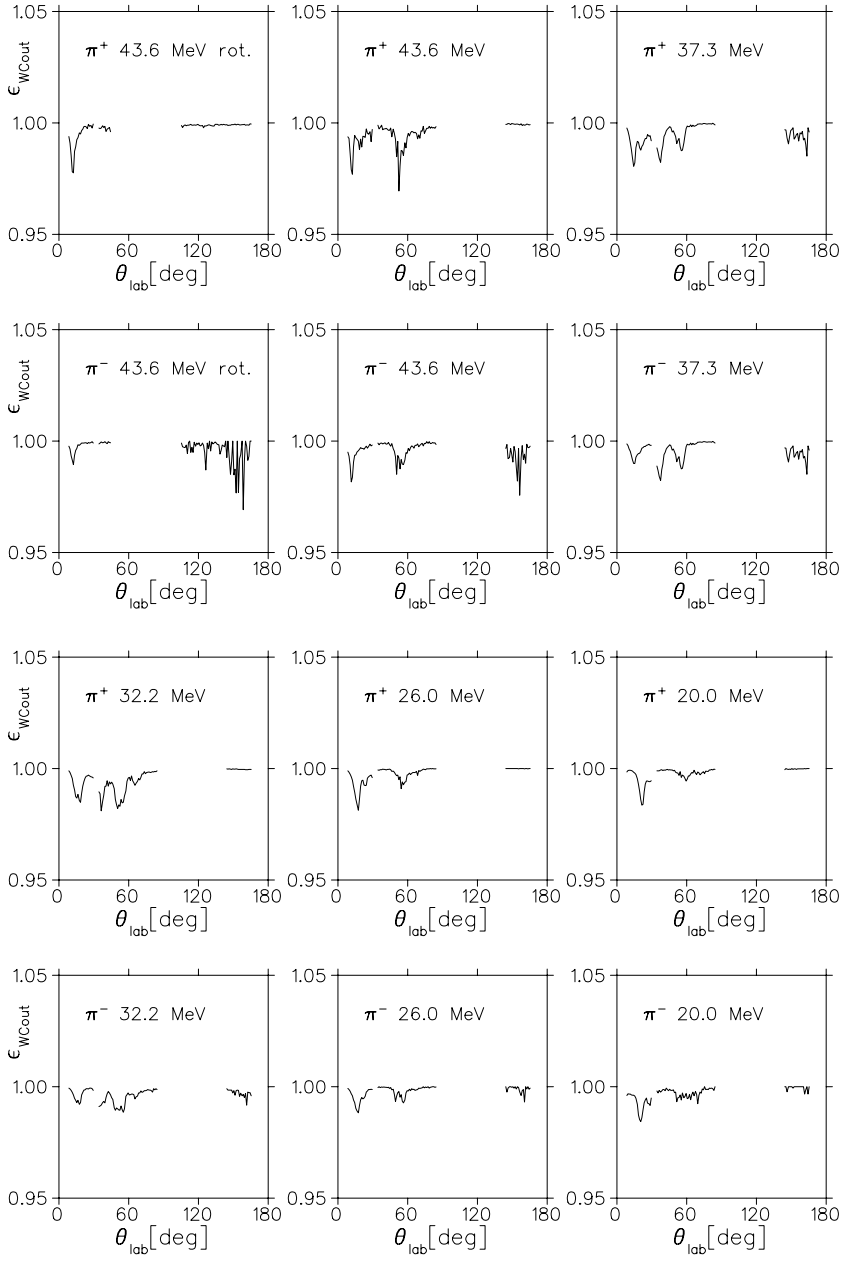

Figure 4.12: *Total wire chamber efficiencies for the outgoing track: the efficiency is always larger than 0.97*

acceptance and has to be explicitely taken into account. The loss of pion flux due to hadronic interactions of pions with detector materials is estimated and corrected for.
Furthermore, for some data a hardware problem in the second level trigger

T_π [MeV]	ϵ_{dc_d}
43.3	0.893
37.1	0.884
32.0	0.876
25.8	0.863
19.9	0.847

Table 4.3: *Pion decay between finger counter and target: fraction of surviving pions* ϵ_{dc_d}

caused events with a missing event type. The fraction of these events is taken into account.

4.4.1 Pion decays before the finger counter

Muons from pion decays right in front of the finger counter might still hit the counter and be counted as pions. To correct for this effect, in a GEANT simulation pions are generated in a spot near the end of the beam pipe, and the the particle type of the particle hitting the finger counter is recorded. From the number of muons N_μ and and pions N_π the correction for this effect is determined.

$$\epsilon_{dc\_u} = \frac{N_\pi}{N_\pi + N_\mu}$$

The effect is nearly independent on the incident pion energy, since two effects work in opposite directions. At lower energies, the probability for a decay increases, but the maximum angle of the muon cone also opens up and more decay muons miss the finger counter. The correction factor ϵ_{dc_u} is found to be 0.964.

4.4.2 Pion decays between finger counter and target

Some pions decay between the finger counter and the target region, thus the pion flux on the target has to be corrected for decays. The fraction of surviving pions ϵ_{dc_d} for the incident energies used is given in table 4.3.

4.4.3 Pion flux reduction by hadronic interactions

The total material crossed by a pion in the CHAOS spectrometer is equivalent to about $\Delta x = 1$ cm of CH_2. The total cross sections for hadronic πC interactions at low energies are not well known. From data measured down to about 80 MeV [Clo76, Car76] an estimate of 228 mb at 50 MeV and 158 mb

T_π	charge	f_{hdr}
43.3	+	0.991
37.1	+	0.992
32.0	+	0.993
25.8	+	0.994
19.9	+	0.995
43.3	-	0.988
37.1	-	0.989
32.0	-	0.990
25.8	-	0.991
19.9	-	0.991

Table 4.4: *Pion flux reduction due to hadronic reactions in detector materials*

at 30 MeV for positively charged pions and 290 mb at 50 MeV and 232 mb at 30 MeV for negatively charged pions is obtained[Str79]. The reaction cross sections calculated there also agree well with a later measurement [Mei87]. The total hadronic cross section for πp scattering in this energy range is less than 10 mb and can be neglected in this consideration.
The loss of flux ΔB/B due to the reactions on Carbon is given by

$$\frac{\Delta B}{B} = -\sigma_L \frac{\rho_{CH_2}}{14\ g} \Delta x N_A$$

where $N_A = 6.02 \cdot 10^{23}$ is the Avogadro constant and $\rho_{CH_2} = 1$ g/cm^3. Therefore the beam after crossing x cm of material is

$$B(x) = B_0 e^{-\sigma_L \frac{\rho_{CH_2}}{14g} N_A x}.$$

The hadronic reaction cross sections used are linearly interpolated. Table 4.4 gives the correction factors used. The absolute error on the correction factor f_{hdr} is estimated to be 0.5 % due to the uncertainties on the cross sections.

4.4.4 2LT trigger correction

For the data measured at 25.8 MeV, a sizable number of events do not contain a valid event type (e.g. "beam sample" or "trigger event") because of a hardware problem in the second level trigger. The number of these "screwball" events is determined from the skim test results. The correction applied to the yield was:

$$\epsilon_{bad2LT} = 1 - \frac{\texttt{screwball}}{\texttt{any\_event}}$$

The correction is only sizable for the full target runs at 25.8 MeV kinetic energy and is 0.948 for the π^+ runs and 0.947 for the π^- runs.

Chapter 5

Results

In this chapter the results of the experiment are presented. Angular distributions for $\pi^{\pm}$p differential cross sections at incident pion energies of 43.3, 37.1, 32.0, 25.8 and 19.9 MeV are shown.

5.1 $\pi^{\pm}$p differential cross sections

Fig. 5.1 depicts π^{+}p differential cross sections, fig. 5.2 π^{-}p differential cross sections. Shown are the results of this experiment for 5 different incident pion energies between 43.3 and 19.9 MeV and scattering angles between 10 and 170 degrees. The error bars only represent the statistical errors of the data points, systematic errors (especially overall normalization uncertainties) will be discussed in section 5.2. Tables of these cross sections can be found in appendix B. The data are compared to two partial wave analyses, the SAID fall 2002 solution [Arn02] and the KH80 solution [KH80].

The measurements covered an angular range between 10 and 180 degrees. However, for the presentation of the data only the regions are selected in which the acceptance and background subtraction are fully under control. Since the acceptance curves drop steeply at the edges of the single detectors (range telescope or CFT blocks, see fig. 4.10) and also at the acceptance hole which is due to the copper target pillars shadowing a region of the CFT blocks, the data points have been selected by the following criteria:

1. Only angular bins with an acceptance of at least 80 % of the maximum acceptance in that region are selected. This removes the large acceptance uncertainty of points in regions where there is a steep rise or fall of the acceptance curve.

2. At forward angles the region most affected by muon decays has been excluded. Even after applying all cuts, the remaining background in the region directly affected by the muon cone is too large to be reliably

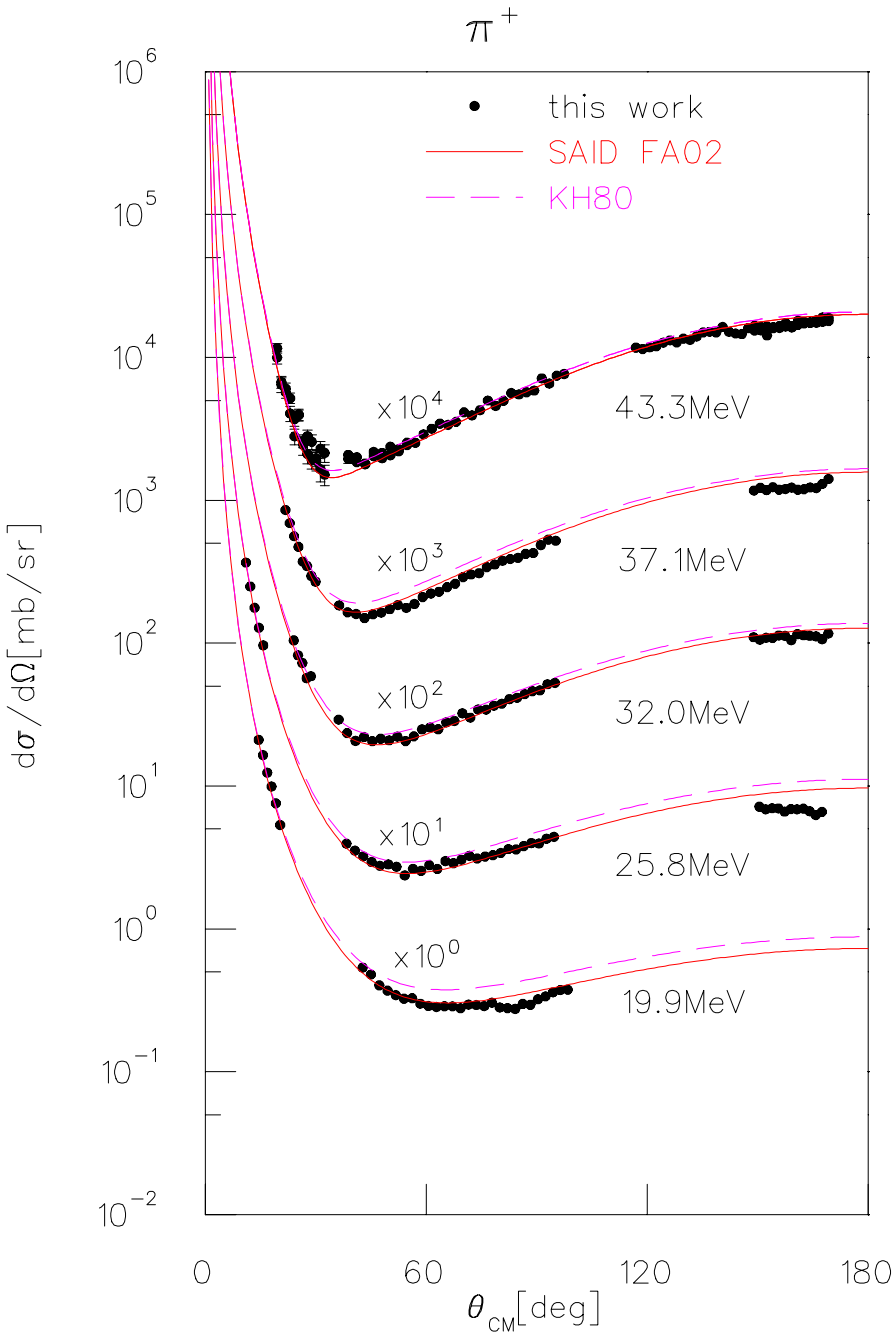

Figure 5.1: *π^+p differential cross sections: shown are the results of this experiment (black filled circles) compared to the SAID FA02 solution (red solid line) and the KH80 solution (magenta dashed line). The error bars shown depict the statistical errors only.*

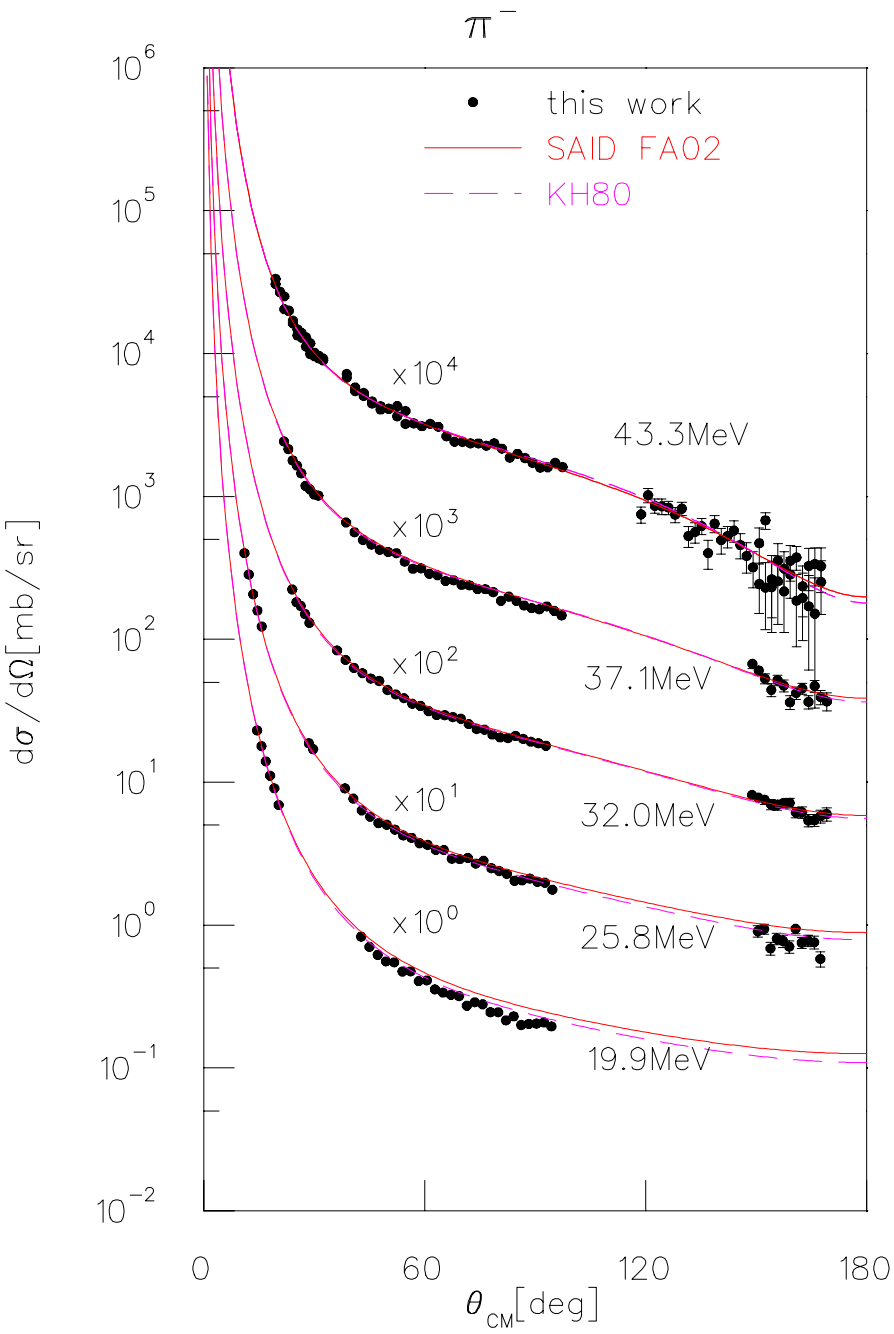

Figure 5.2: *$\pi^- p$ differential cross sections: shown are the results of this experiment (black filled circles) compared to the SAID FA02 solution (red solid line) and the KH80 solution (magenta dashed line). The error bars shown depict the statistical errors only.*

treated by background subtraction. The region removed is determined by the crossover point of the muon cone and the elastic scattering band. A region of ± 4 degrees from this point for the data at 43.3 MeV and 37.1 MeV and ± 5 degrees for the lower energies has been removed from the data sets. For the data at 25.8 MeV and 19.9 MeV, the region is shifted by 1 degree towards larger angles to account for the different energy loss of pions and muons in the liquid hydrogen and the chambers. In cases where after this procedure of exclusion one single point without direct neighbors remains, this point has also been removed.

3. In addition, the backward angle data between 150 and 180 degrees at 19.9 MeV have been rejected, since the acceptance obtained in the GEANT simulation is very sensitive to changes of detector materials (e.g. structural elements or the thickness of glue layers) and therefore cannot be reliably determined (see section 4.2.2).

The properly weighted scattering angle averages for the bins of data points measured with the range telescope (up to 35 degrees) are determined taking into account the weighting effect of the steeply falling cross sections. The angles are calculated by splitting each angular bin at the true scattering angle into two parts requiring that the integrated SAID cross sections for both parts of the bin are equal in size. The difference between the SAID cross sections and the true measured cross sections is sufficiently small to be neglected in this correction.
The data measured in this work will be compared to previously available data and partial wave analyses in chapter 6.

5.2 Discussion of systematic errors

5.2.1 Direct estimates for systematic errors

The following sources of systematic errors contribute significantly to the total systematic error and have been investigated:

- *Yield*: Variations of cuts have been studied to test the sensitivity of the yield to different cuts (for a definition of the cuts, see chapter 3). The following cuts have been varied both in the reconstruction of real data and in the analysis of the GEANT data, and the effects of variations of the cuts are used to estimate the systematic errors which should be quoted. The variations used are sizable and give an upper limit for the uncertainties due to the cuts.

- *finger ADC*: An increase of the threshold for the ADC signal by 5 % changes the cross sections by 1 %.
- `sepr` *and* `verl`: Depending on the algorithm used in the reconstruction of the vertex, the vertex is restricted to the target region along the beam axis by the `sepr` or `verl` cut. A variation of the width of these cuts by 10 % changes the yield by 0.5 % for the larger angle data measured with the CFT blocks and by 1 % for the forward angle data measured with the range telescope. The effect is larger at forward angles because the uncertainty in the reconstruction of a vertex is larger for small scattering angles.
- `rproj`: A change of the width of the `rproj` cut by 10 % changes the yield by 0.5 % for the CFT region and 2 % for the range telescope region.
- *momentum cut* for muons: The yield changes by 1 % when varying the momentum cut for muons by 10 %.
- *momentum cut* for pions detected with the range telescope: The yield for pions detected with the range telescope changes by 3 % when modifying the width of the cut on the pion momentum by 10 %. This cut is quite tight to suppress decay background.
- *p-θ box* for pions detected with the CFT blocks: A variation of the width of the p-θ-box cut by 10 % results in a change of yield by 0.5 % for the pions detected with the CFT blocks.
- *track extrapolation cut* for pions detected with the range telescope: A change in the width of this extrapolation cut by 10 % (from 18 to 16 cm) changes the yield by 2 % .

- N_{beam}: Two scalers were used to record the number of beam particles, the maximum difference observed between the scalers is 0.5 %.

- N_{target} (*target angle and thickness*): The target angle is known with an accuracy of 1 degree, this uncertainty translates into a systematic error for the thickness of 1 %. The thickness of the cell containing the LH_2 is 12.5 mm, the estimated precision is 250 μm. This implies an uncertainty of 2 %.

- *Particle fractions* f_π, f_μ: The uncertainties in these fractions are due to the limited number of particles in the beam samples. The resulting uncertainty for pions is always less than 0.5 %, for the muons the uncertainty is 5 % for $T_\pi = 43.3$ MeV and less than 1.5 % for the other energies.

- *Decays between finger counter and target*: The path from the finger counter to the target is 76.8±2 cm. The variation in the distance is mainly due to different trajectories for the incoming beam particles. This variation translates into an uncertainty due to the decay correction of 0.4 %.

- *pion flux correction due to hadronic interactions*: The uncertainty of this correction is estimated to be 0.5 % (the total hadronic cross sections for πC scattering are not well known at low energies, see section 4.4.3).

- *neural network efficiency*: The efficiency of the neural network is determined by control samples in the training runs. The efficiency given for the identification of muons can be verified by looking at μp scattering events. For these muon events the neural network decision can be checked. The observed efficiency for muons in the actual experiment is about 1 % lower than the efficiency claimed by the control samples, therefore the uncertainty of the particle identification efficiency for pions is also assumed to be 1 %.

- *Solid angle* $d\Omega_{eff}$: Moderate variations of the geometry used in the GEANT simulation show no significant change in the calculated acceptance. The acceptance hardly changes with a change of the radius where the triggering scintillators (DE1 and first layer of the range telescope) are placed. This is due to the focusing effect of the CHAOS fringe field. Also a rotation of the target in the simulation changes the acceptance only at the edges of the acceptance hole due to the target pillars. All effects seen are in the order of 0.5 %. Therefore the total systematic error on the effective solid angle $d\Omega_{eff}$ is estimated to be of the order of 1 % .

The results of these considerations are summarized in table 5.1. The total systematic errors obtained by adding up the errors quadratically are 2.9 % for pions at larger angles, 5.2 % for pions detected at small angles with the range telescope, 6.2 % for muons at T_π=43.3 MeV and 4.2 % for muons at the other energies.

5.2.2 $\mu^{\pm}$p differential cross sections

The absolute normalization used for the πp scattering data can be checked by analyzing the μp scattering events recorded simultaneously during the experiment. Uncertainties in quantities like the target density, target thickness, beam scalers, or cuts used will affect both πp and μp cross sections in

quantity or cut	systematic error for		
	π CFT [%]	π RT [%]	μ RT [%]
finger noise	1	1	1
`sepr/verl`	0.5	1	1
`rproj`	0.5	2	2
momentum	0.5	3	1
track extrapolation		2	
neural network		1	
N_{beam}	0.5	0.5	0.5
target rotation	1	1	1
target thickness	2	2	2
particle fraction	0.5	0.5	5 (T_π=43.3 MeV)
			1.5 (other energies)
decay ϵ_{dc_d}	0.4	0.4	
hadronics	0.5	0.5	
GEANT	1	1	1
total	2.9	5.2	6.2 (T_π=43.3 MeV)
			4.2 (other energies)

Table 5.1: *Systematic error estimates: shown are the systematic errors for pions detected with the CFT blocks (scattering angles greater than 35 degrees), pions detected with the range telescope (RT) and muons detected with the range telescope.*

the same way.
The results for μp scattering are shown in fig. 5.3 for positive charge and fig. 5.4 for negative charge.

Plotted are measured muon-proton cross sections (filled black circles) at the 5 corresponding muon energies (see table 2.1) compared to a QED calculation with the proton electric and magnetic form factors as input (red line) [Pok98]. There is good agreement between the measured data and the calculation down to very small scattering angles. This demonstrates that the reconstruction of the full three-dimensional scattering angle is implemented correctly in the analysis.
Plots showing the measured μp cross sections divided by the prediction of the calculation are shown in fig. 5.5 for μ^+p and 5.6 for μ^-p scattering. The predicted cross sections are integrated over the 1 degree wide angular bins to account for weighting effects due to the steeply falling cross sections.

The ratios of measured μp cross sections divided by the electroweak predictions are determined by fits to the data points in the ratio plots. Horizontal lines are fitted to the ratios of measured cross sections divided by

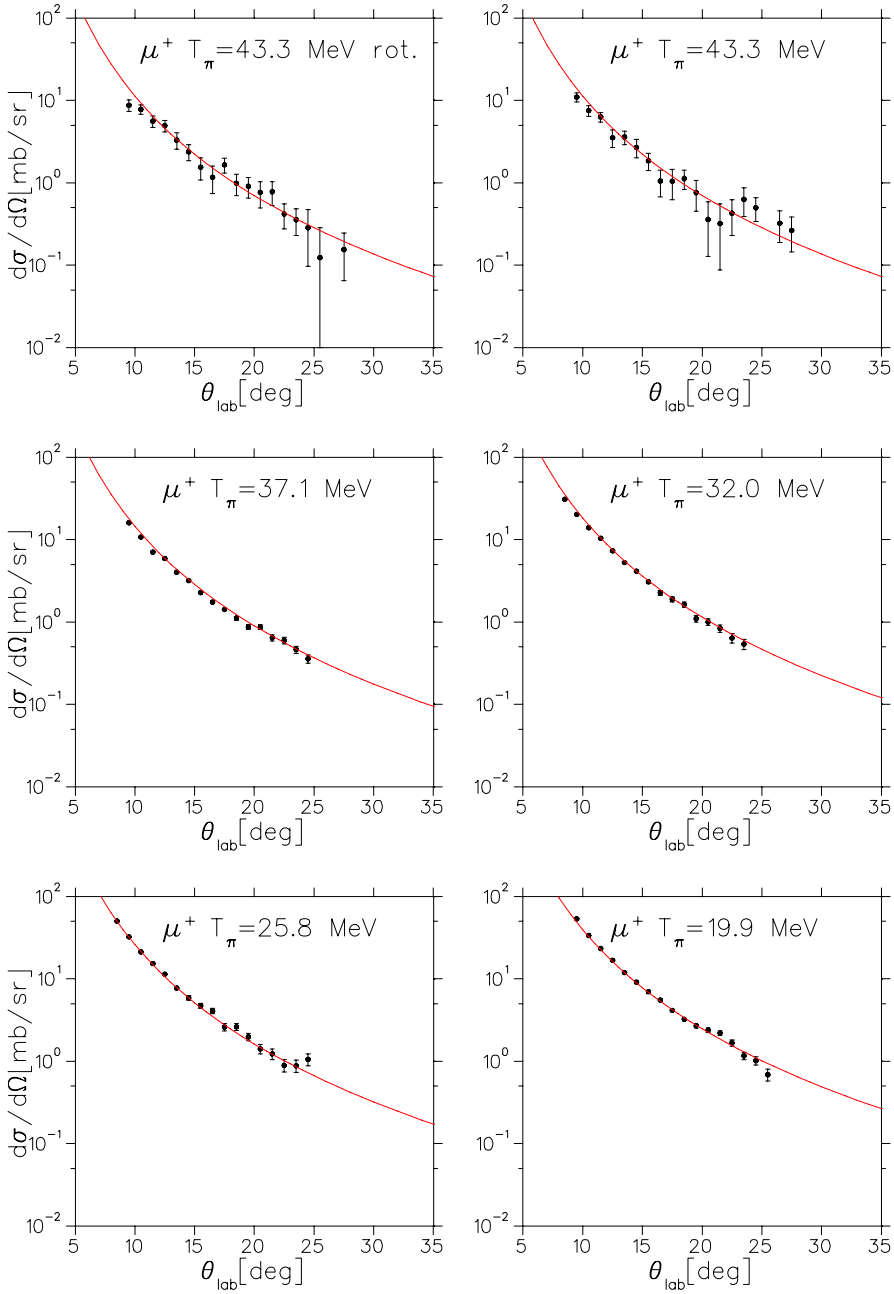

Figure 5.3: *Results for differential cross sections in μ^+p scattering: the energy given is the corresponding pion energy in the center of the target, the kinetic energies of the muons are 53.5 MeV, 46.2 MeV, 40.5 MeV, 33.3 MeV and 26.4 MeV (see table 2.1). The black filled circles depict the measured cross sections, the red curve is the result of a calculation. The error bars shown depict the statistical errors only.*

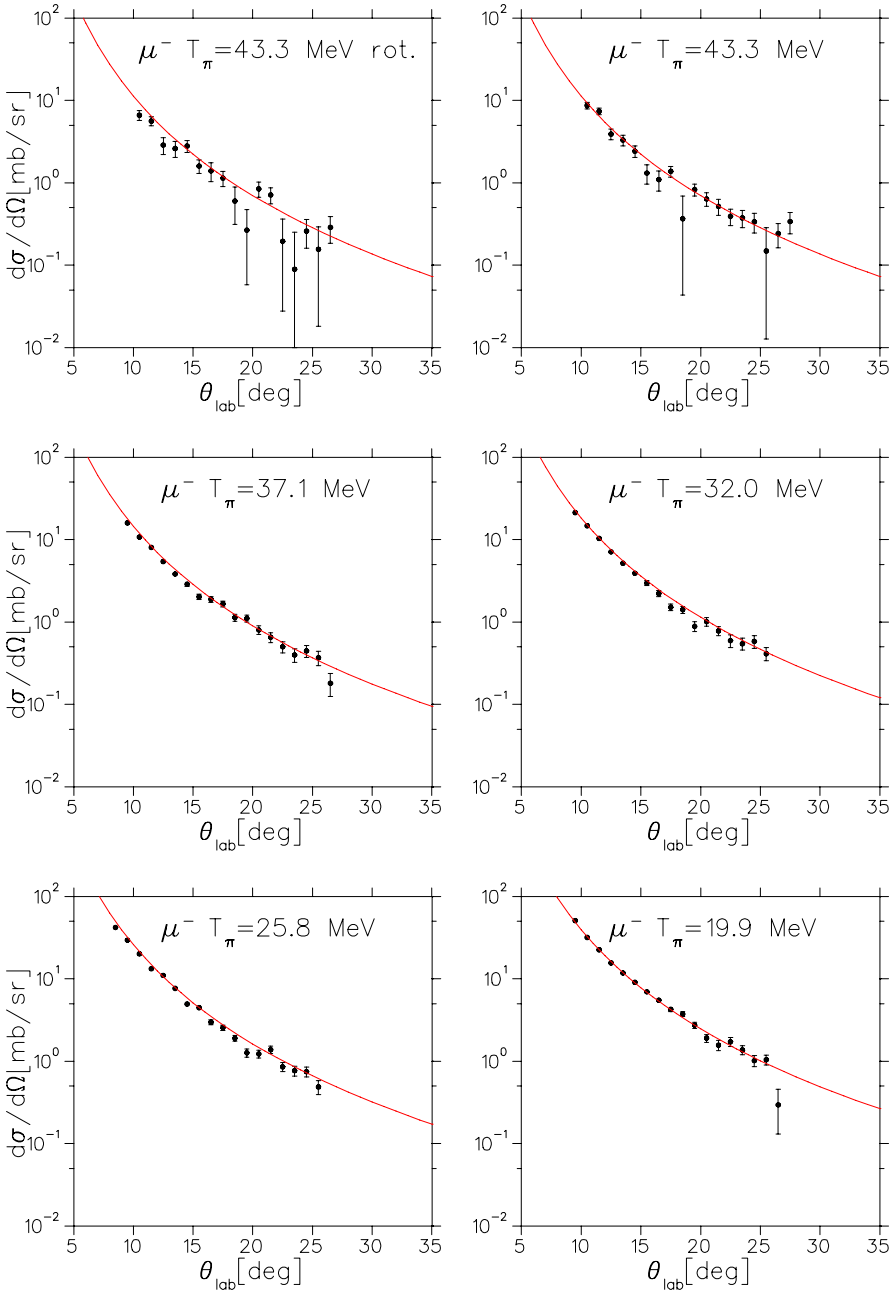

Figure 5.4: *Results for differential cross sections in $\mu^- p$ scattering: the energy given is the corresponding pion energy in the center of the target, the kinetic energies of the muons are 53.5 MeV, 46.2 MeV, 40.5 MeV, 33.3 MeV and 26.4 MeV (see table 2.1). The black filled circles depict the measured cross sections, the red curve is the result of a calculation. The error bars shown depict the statistical errors only.*

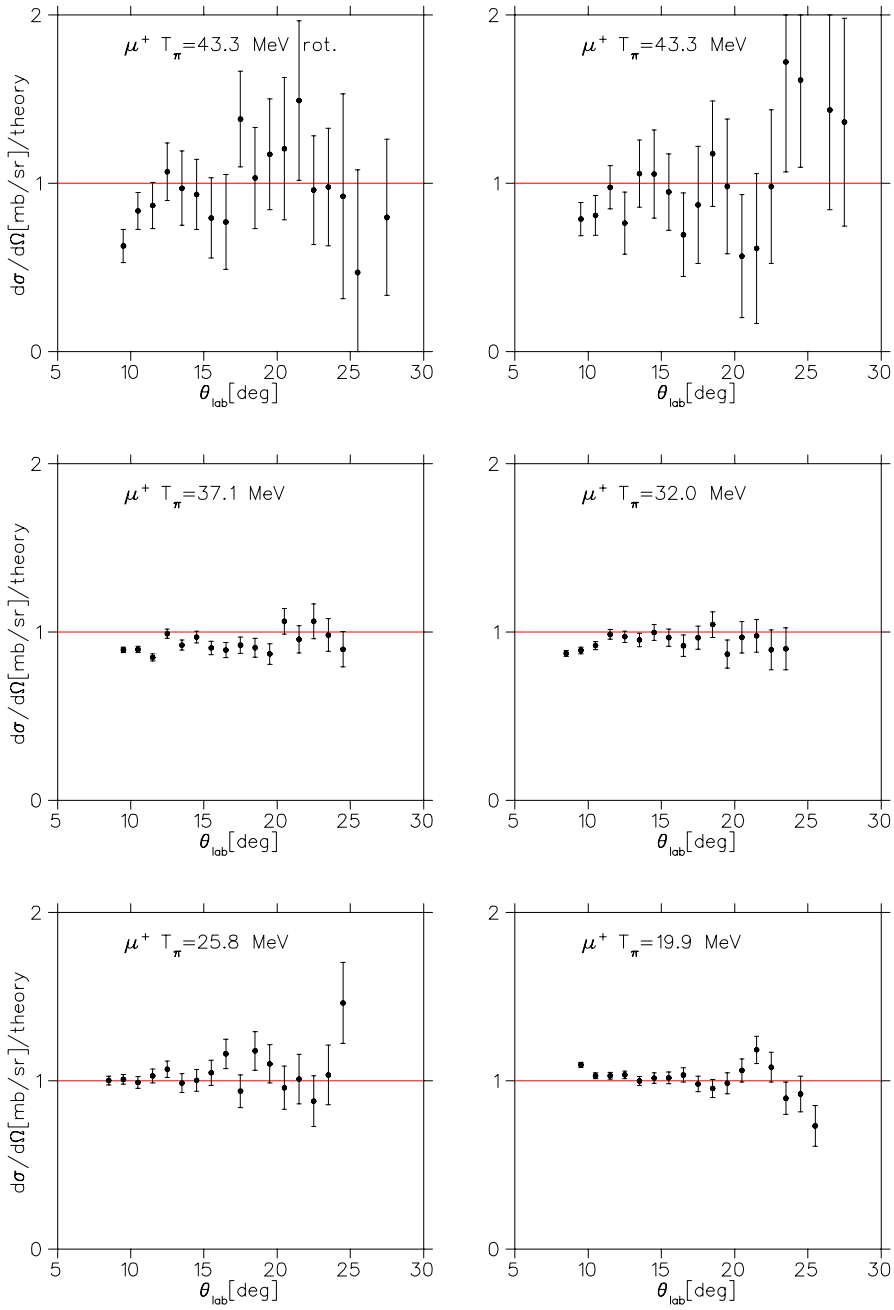

Figure 5.5: *Ratios of μ^+p cross sections divided by the prediction from a theoretical calculation*

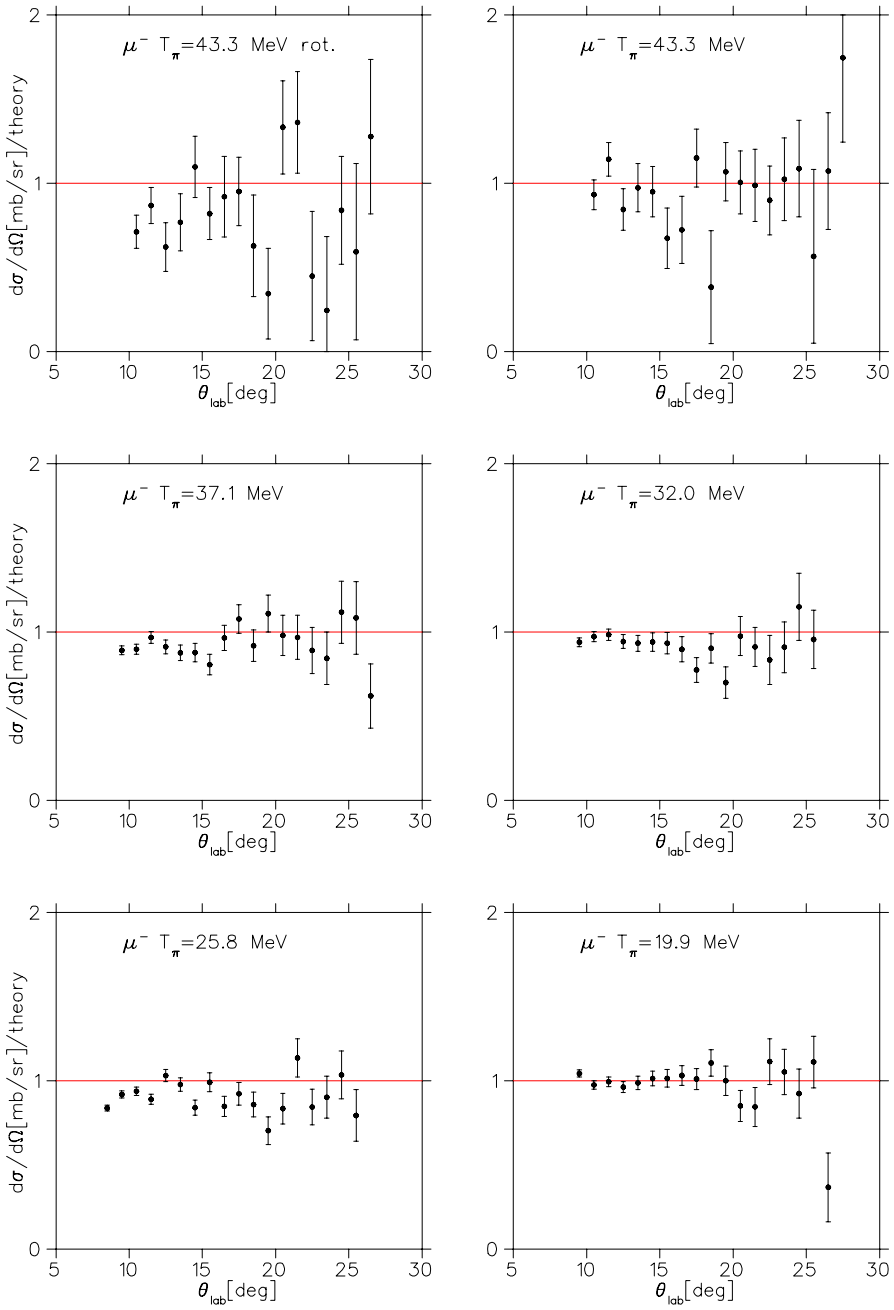

Figure 5.6: *Ratios of $\mu^- p$ cross sections divided by the prediction from a theoretical calculation*

T_π [MeV]	charge	$r \pm \Delta(r)_{stat} \pm \Delta(r)_{syst}$
43.3 (rot.)	+	$0.86 \pm 0.05 \pm 0.06$
43.3	+	$0.88 \pm 0.04 \pm 0.06$
37.1	+	$0.90 \pm 0.01 \pm 0.04$
32.0	+	$0.99 \pm 0.01 \pm 0.04$
25.8	+	$1.01 \pm 0.02 \pm 0.04$
19.9	+	$1.04 \pm 0.01 \pm 0.04$
43.3 (rot.)	-	$0.80 \pm 0.05 \pm 0.06$
43.3	-	$0.96 \pm 0.04 \pm 0.06$
37.1	-	$0.91 \pm 0.01 \pm 0.04$
32.0	-	$0.93 \pm 0.01 \pm 0.04$
25.8	-	$0.89 \pm 0.02 \pm 0.04$
19.9	-	$1.00 \pm 0.01 \pm 0.04$

Table 5.2: *Average ratio r between measured μp cross sections and the theoretical prediction.*

the theoretical expectation. The average factors r obtained are given in table 5.2. At $T_\pi = 43.3$ MeV, the statistical uncertainty of the muon flux is rather high and therefore the statistical uncertainties are large. For the other energies, the ratios obtained are compatible with 1, and the normalization uncertainty is estimated to be less than 5 %. A notable exception are the data at $T_\pi = 37.1$ MeV: The data are consistently low by about 8 %. A corresponding effect is observed in the pion data. Therefore a renormalization of this data set by 8 % should be considered.

Chapter 6

Discussion

In this chapter the results of the experiment are discussed. In section 6.1 they are compared to data from previous experiments and two existing partial wave analyses. Section 6.2 gives the results of single energy partial wave analysis fits to the data. The phase shifts obtained are compared to the SAID FA02 solution, the KH80 solution and at two energies to single energy fits to data from a previous experiment.

6.1 Comparison to previous results

6.1.1 Comparison to previous data

The comparison to previously available data is most easily done using plots showing measured data points divided by the SAID FA02 partial wave analysis prediction for the corresponding energy. These plots give a more sensitive and linear representation of the data and their deviations from the SAID FA02 solution. For the forward angle data measured with the range telescope, the SAID cross sections are interpolated and integrated to get the averaged cross sections for the 1 degree wide bins in which the data points are shown. The ratios for data measured in this experiment are presented in fig. 6.1 for the π^+p channel and in fig. 6.2 for the π^-p channel. For the data measured at 43.3 MeV, the two data sets corresponding to the measurement with a target angle of -64 degrees (denoted "rot.") and -24 degrees relative to the x-axis of the CHAOS coordinate system are displayed in two separate graphs. The data measured in previous experiments at close-by energies[1] are also divided by the SAID predictions to their respective energies and shown in these plots in the right column. Data in the quoted narrow energy regions (e.g. 44.6 MeV to 45.1 MeV) are plotted in one single ratio plot. Similar plots for all existing $\pi^{\pm}$p differential cross section measurements below 50 MeV can be found in appendix C. These plots allow to investigate

[1] Only data that were taken at kinetic energies that agree within ±5 % with the energies from this experiment are used for the comparison.

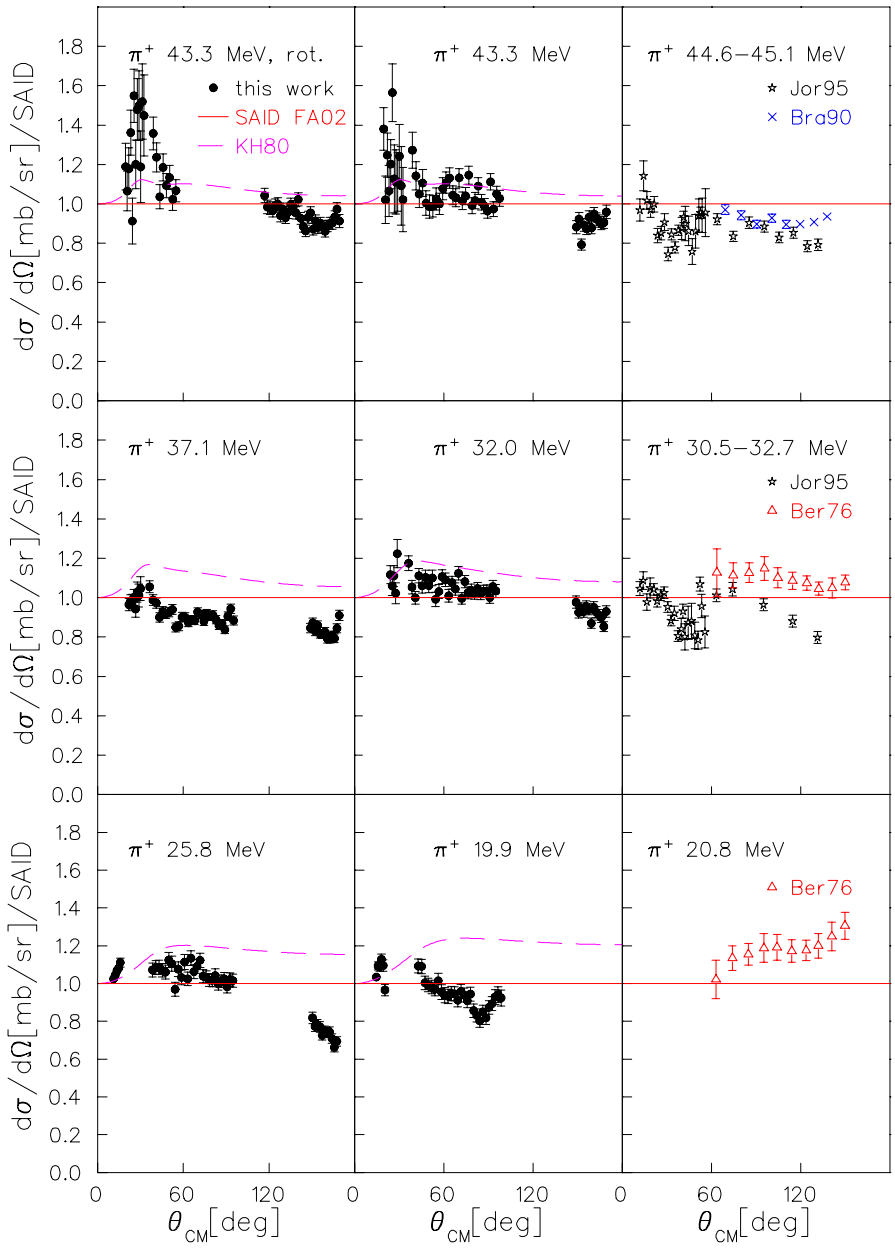

Figure 6.1: *Ratios of measured π^+p cross sections and the SAID FA02 solutions for the corresponding energies. The first two columns show the results of this work. The dashed lines shown are the KH80 solutions also divided by the SAID FA02 solutions. "rot." denotes the measurement at 43.3 MeV with a target angle of -64 degrees relative to the x-axis of the CHAOS coordinate system. All other data sets have been measured with a target angle of -24 degrees. The third column depicts previously measured data at close-by energies divided by the corresponding SAID FA02 solutions.*

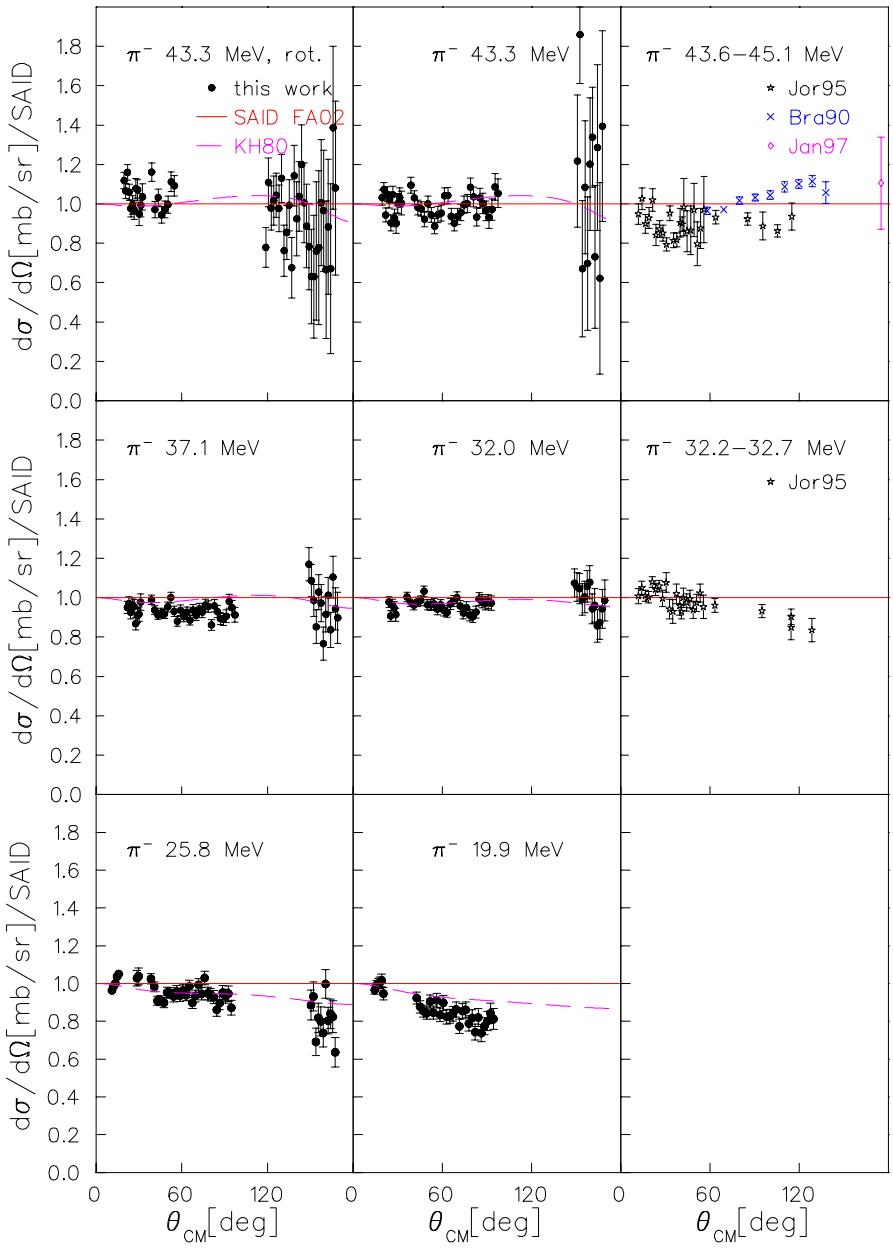

Figure 6.2: *Ratios of measured $\pi^- p$ cross sections and the SAID FA02 solutions for the corresponding energies. The first two columns show the results of this work. The dashed lines shown are the KH80 solutions also divided by the SAID FA02 solutions. "rot." denotes the measurement at 43.3 MeV with a target angle of -64 degrees relative to the x-axis of the CHAOS coordinate system. All other data sets have been measured with a target angle of -24 degrees. The third column depicts previously measured data at close-by energies divided by the corresponding SAID FA02 solutions.*

deviations from the SAID partial wave fit in detail. An additional advantage of these plots is that data measured at not exactly the same energy can be directly compared. However, one has to keep in mind that the SAID curve is not the result of a theoretical calculation, but a fit to the data available before this experiment.

For the **π^-p channel**, at 43.3 MeV our data lie in-between the data by Brack et al. [Bra90] (measured at 45.0 MeV) and the data by Joram et al. [Jor95, Jor95b] (measured at 44.6 and 45.1 MeV). The backward angle data is compatible with the point at 175 degrees measured by Janousch et al. [Jan97] (at 43.6 MeV). The suppression around 40 degrees seen by Joram et al. is not confirmed.
At 32.0 MeV, there is good agreement between the data measured by Joram et al. (at 32.2 MeV) and this work for angles up to 80 degrees, however for our data towards the largest angles there is no deviation from the SAID FA02 solution seen as observed for the data by Joram et al.

In the **π^+p channel** there are larger discrepancies between data.
At 43.3 MeV, the results from this work have larger values than the data from Brack et al. (at 45.0 MeV) and Joram et al. (at 44.6 MeV and 45.1 MeV). Towards backward angles the data approach the results by Brack et al., the strong suppression at backward angles seen by Joram et al. is not observed. At forward angles around 40 degrees, the minimum seen in the Coulomb-nuclear interference region is found to be far less pronounced than seen by Joram et al.
At 32.0 MeV, again the comparison with the Joram et al. data (measured at 32.2 MeV) yields similar results. The data at forward angles around 40 degrees do not show the suppression observed in the previous experiment, also towards large angles the data are higher than the Joram et al. results. Compared to the results from Bertin et al. [Ber76] (measured at 30.5 MeV), the cross sections are about 10 % lower, the shape of the distribution is similar.
At 19.9 MeV the cross sections measured are about 20 % lower than the results from Bertin et al. (taken at 20.8 MeV). Also the shape of the angular distribution is different at this energy.
The findings that the data by Joram et al. (at 32.7 MeV) and the Bertin et al. data (at 20.8 MeV) are problematic are in agreement with the results of a statistical analysis [Mat97] of the πp low energy database.

6.1.2 Comparison to partial wave analyses

In this section, the results from this work are compared to two partial wave analyses, the SAID FA02 solution and the KH80 solution.

In the **π^-p channel**, the data show good agreement with the SAID FA02 solution for energies from 43.3 MeV to 32.0 MeV (fig. 6.2). At 25.8 MeV, for the backward angle region significant deviations are observed. At 19.9 MeV, the shape of the angular distribution is different, and the cross sections at larger angles are lower than given by SAID FA02. At higher energies, the KH80 solution is very similar to the SAID FA02 solution in this channel, at 25.8 and 19.9 MeV the KH80 result gives a better description of the data. Overall, the KH80 solution is superior for π^-p.

In the **π^+p channel** there is a systematic deviation from the SAID partial wave analysis (fig. 6.1). For all energies, at forward angles the cross sections are higher than predicted by the SAID FA02 solution, at very backward angles the data are systematically 10 to 20 % lower than the partial wave solution. The discrepancy at backward angles is increasing towards lower energies.
A possible reason for this behavior could be that the cross sections reported by Joram et al. are low at small angles (see section 6.1.1) and may have pulled down the SAID partial wave analysis. Also, there has been very little data with good statistics at very backward angles between 150 and 180 degrees up to now.
Significantly, the KH80 solution which does not include the results by Joram et al. and which has a higher predictive power due to more rigorous analytical constraints is superior to SAID at small angles, but drastically worse (too high) at large angles.

One might suspect that the deviations towards the lowest energies are due to experimental problems with the energy loss of pions in detector materials and corresponding uncertainties in the acceptance (as discussed for the 19.9 MeV data between 150 and 180 degrees which therefore have been removed from the analysis). However, for two reasons this explanation is unlikely. Firstly, the observed behavior is quite different for positive and negative charge. Since the two data sets were measured with exactly the same setup, just reversing the polarity of all magnets, the effect should be the same in both cases. Secondly, at 25.8 MeV incident pion energy, the kinetic energy of a pion scattered under 160 degrees is 14 MeV. At 19.9 MeV incident pion energy, the same energy for the scattered pion is already reached

at 95 degrees. Yet, judging from the measured data, there is no apparent acceptance problem at 19.9 MeV for scattering angles up to 110 degrees: The π^+p data show no significant deviations from the SAID expectations, while the π^-p data are lower towards larger angles. As a conclusion, attributing the low cross sections observed at 25.8 and 19.9 MeV to problems due to energy losses does not provide a consistent explanation of the effects seen. The shape of the SAID curve at 19.9 MeV is probably also influenced by the π^+p data set measured by Bertin et al. at 20.8 MeV. However, the data from this experiment do not agree with the distributions measured by Bertin.

Overall, there is better agreement between the data and partial wave analyses in the π^-p channel than in the π^+p channel.

6.2 Results of single energy fits

Single energy fits adjusted simultaneously to the π^+ and π^- data have been performed for the 5 measured energies [Sta04], the results are summarized in this section. In the fits the phase shifts for s- and p-waves are adjusted, higher partial waves ($l = 2$ and $l = 3$) are fixed and taken from the KA84 solution [Koc85]. The results of the fits are given in table 6.1.

The results of the single energy partial wave fits are shown in ratio plots, for π^+p in fig. 6.3 and for π^-p in fig. 6.4. The fits give a better description for the π^-p channel than for the π^+p channel. This may be understood because the π^+p channel is pure isospin 3/2 and therefore has to be described by only 3 amplitudes, while for the description of the π^-p channel 6 amplitudes can be varied in the fit. The fact that the partial wave fits do not describe both channels equally well might also be a hint towards isospin violation in the pion-nucleon system.

Overall, the fits give a good description of the data. In particular, it is possible to describe the very backward angle behavior observed in the π^+p channel which presented problems to the SAID and KH80 predictions as we have seen. Only at 19.9 MeV, the fit does not give a good description of the data for the π^+p channel. Correspondingly, there is a smooth behavior of the phases with energies going from 43.3 MeV to 25.8 MeV, but at the lowest energy (19.9 MeV) there is a strong change in the P_{31} phase.
Comparing the results of the fits to the SAID FA02 solution in table 6.1, the S_{11} and the S_{31} phase shift have a smaller absolute size than expected. The absolute value of P_{11} is smaller, of P_{31} is larger than in the SAID FA02

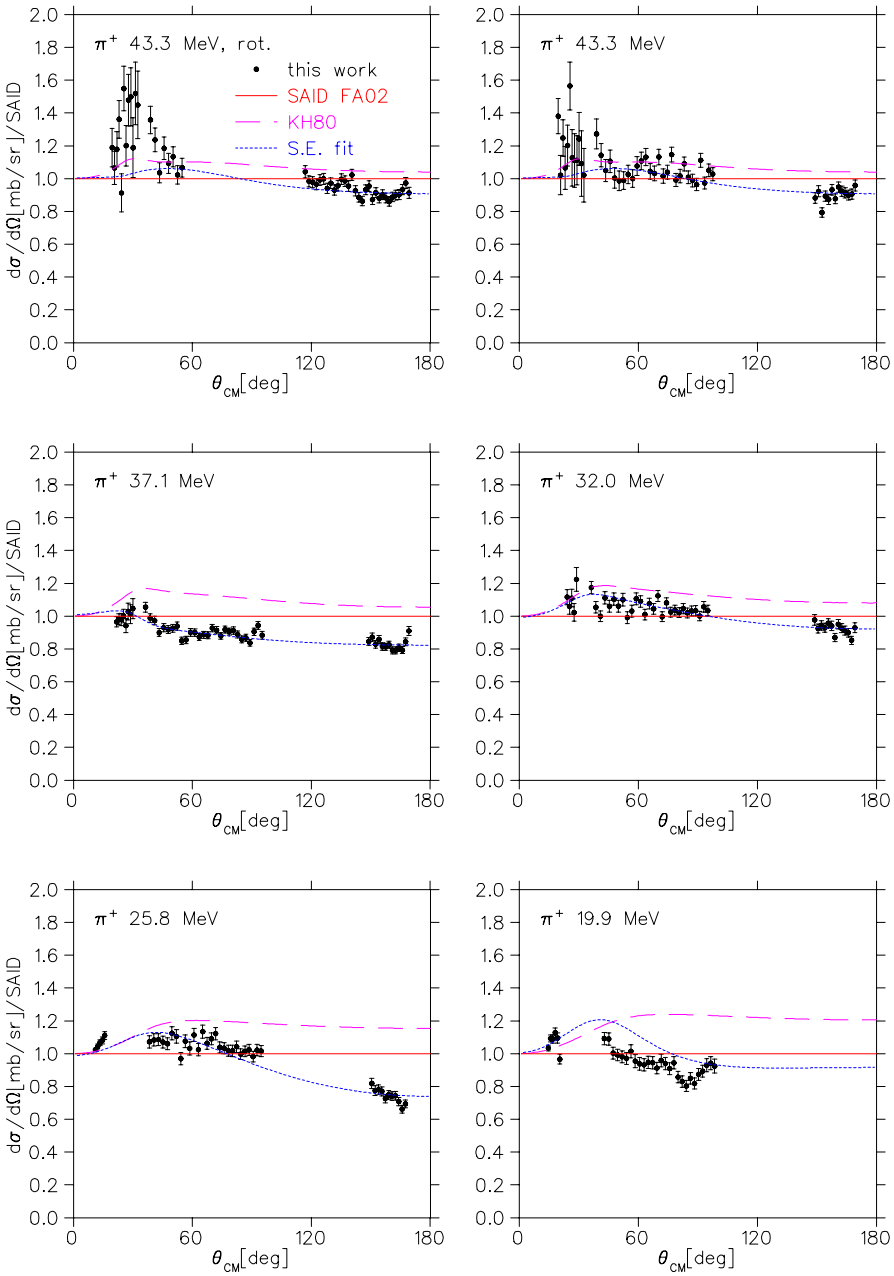

Figure 6.3: *Ratio of measured π^+p cross sections and SAID FA02 predictions. Also shown are KH80 predictions (dashed line) and results of a single energy fit (dotted line).*

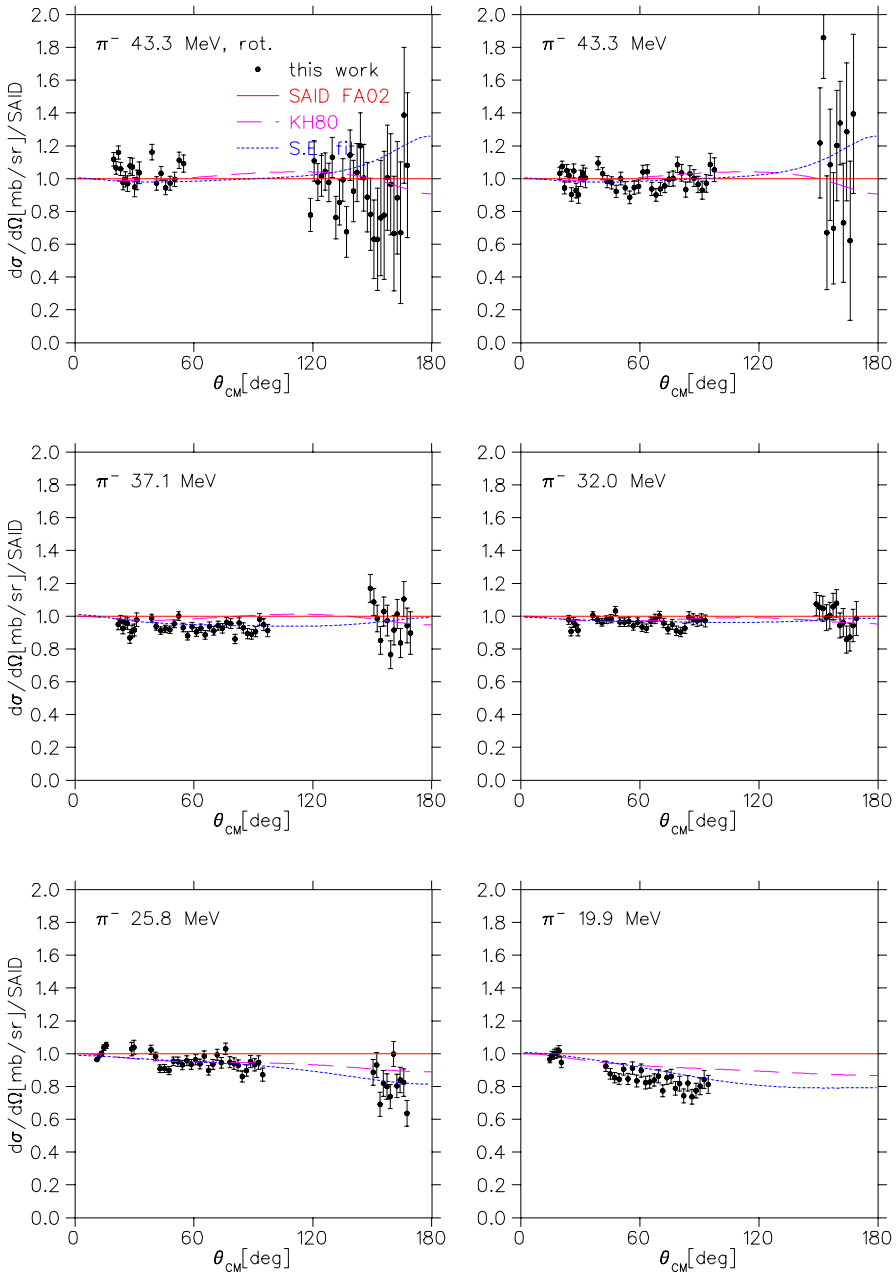

Figure 6.4: *Ratio of measured $\pi^- p$ cross sections and SAID FA02 predictions. Also shown are KH80 predictions (dashed line) and results of a single energy fit (dotted line).*

T_π[MeV]	δ[deg] for	S_{11}	P_{11}	P_{13}	S_{31}	P_{31}	P_{33}
43.3	this work	6.32	-0.52	-0.57	-4.31	-0.92	4.54
	SAID FA02	6.31	-0.70	-0.42	-4.61	-0.66	4.54
	KH80	6.43	-0.81	-0.40	-4.84	-0.79	4.65
45.1	Joram et al.	5.15	-1.03	-0.04	-3.74	-0.77	4.36
37.1	this work	5.67	-0.45	-0.35	-3.68	-0.62	3.28
	SAID FA02	5.90	-0.60	-0.34	-4.10	-0.53	3.48
	KH80	6.04	-0.70	-0.33	-4.41	-0.64	3.57
32.0	this work	5.58	-0.34	-0.31	-3.70	-0.59	2.68
	SAID FA02	5.56	-0.51	-0.28	-3.70	-0.43	2.76
	KH80	5.67	-0.60	-0.27	-4.03	-0.50	2.80
32.7	Joram et al.	4.93	-0.76	-0.01	-2.95	-0.70	2.72
25.8	this work	4.79	-0.24	-0.07	-2.89	-0.69	1.80
	SAID FA02	5.06	-0.40	-0.21	-3.18	-0.32	1.96
	KH80	5.12	-0.46	-0.21	-3.56	-0.36	2.03
19.9	this work	4.38	-0.06	-0.09	-2.86	0.65	0.63
	SAID FA02	4.48	-0.29	-0.14	-2.65	-0.22	1.29
	KH80	4.53	-0.31	-0.15	-3.07	-0.23	1.34

Table 6.1: *Phase shifts for the 5 measured energies: Listed are the phase shifts obtained by single energy fits to the results of this experiment [Sta04], the phase shifts from the SAID FA02 solution [Arn02], the KH80 solution [KH80] and for two energies the phase shifts obtained by single energy fits to the results of Joram et al.[Jor95b]*

solution. The behavior of the phase shifts with energy is shown in fig. 6.5.

The S_{31} and S_{11} phase shifts extracted from this experiment at 43.3 MeV and 32.0 MeV do not confirm the findings by Joram et al. [Jor95b] that these phases are about 1 degree smaller than the phases from the SAID FA02 solution at 45.1 MeV and about 0.7 degrees smaller at 32.7 MeV.

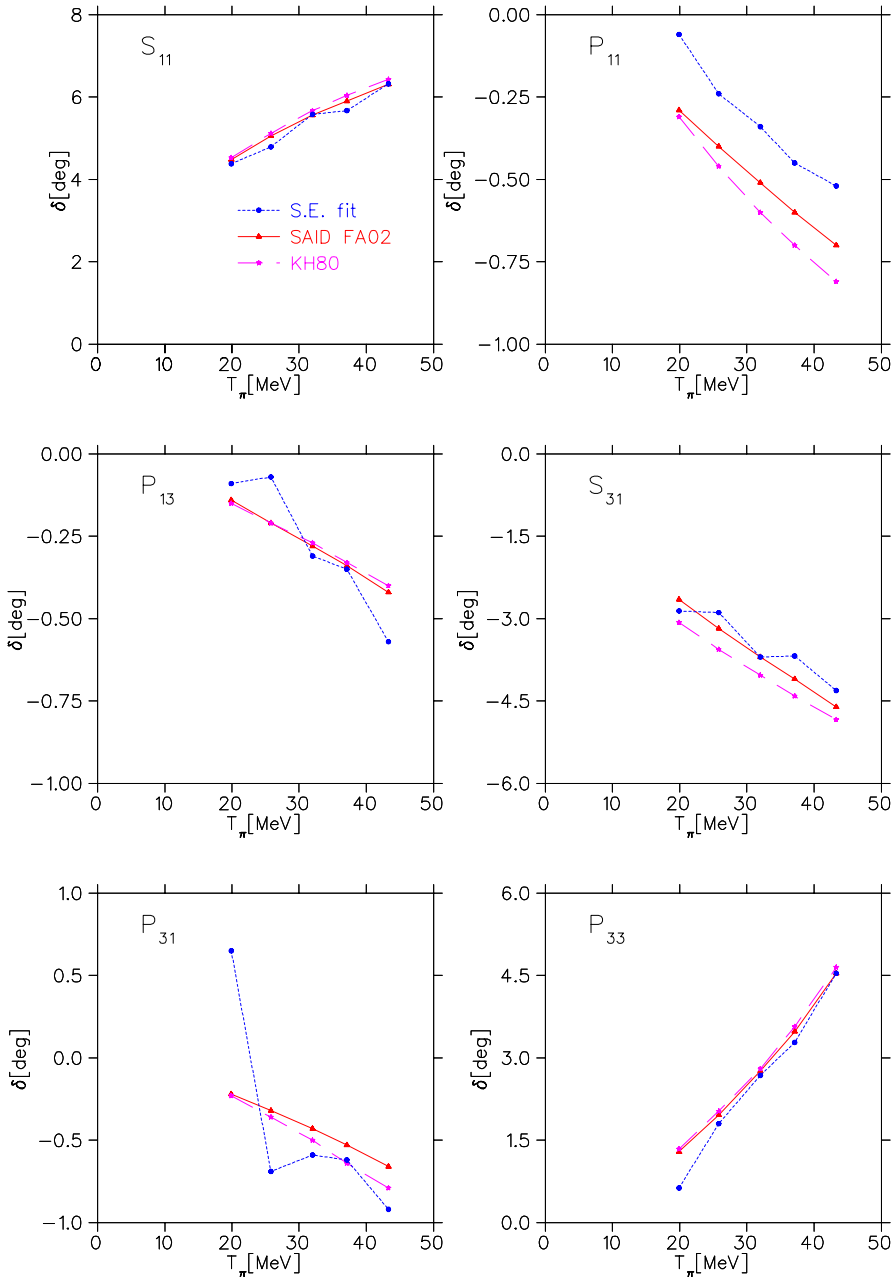

Figure 6.5: *Energy dependence of phase shifts: shown are the 6 phase shifts (s- and p-wave) $S, P_{2I,2J}$ from the SAID FA02 solution (solid line), the KH80 solution (dashed line) and the results from the single energy fit (dotted line).*

Chapter 7

Conclusion and outlook

TRIUMF experiment 778 measured differential cross sections in π^+p and π^-p elastic scattering at low energies from 19.9 to 67.0 MeV incident pion energy. The data analyzed in this thesis were taken at 19.9, 25.8, 32.0, 37.1 and 43.3 MeV. The CHAOS spectrometer was used to simultaneously cover a large angular range, at forward scattering angles this spectrometer was supplemented by a range telescope capable of identifying pions and muons. This allowed parallel μp cross section measurements at forward angles to test the angle reconstruction and normalization.
In the π^-p channel, the cross sections from this experiment at 43.3 MeV lie in-between the data by Brack et al. and the data by Joram et al. measured at close-by energies. The suppression around 40 degrees seen by Joram et al. is not confirmed. At 32.0 MeV the results are similar to the Joram et al. data for angles up to 80 degrees, the deviation from the SAID solution observed by Joram et al. at higher angles is not seen. There is good agreement with partial wave analyses at the higher energies, at 25.8 and 19.9 MeV the data at larger angles are lower than the SAID FA02 solution. The KH80 phase shift solution gives a better description of this channel.
In the π^+p channel, at 43.3 MeV the data at large angles are higher than the results from Brack et al. and Joram et al. The strong suppression at backward angles seen by Joram et al. is not observed. At forward angles around 40 degrees the Coulomb-nuclear interference minimum is found to be far less pronounced than seen by Joram et al. At 32.0 MeV, again the comparison with the Joram et al. data yields similar results in the interference region and at backward angles. At 19.9 MeV, the cross sections are about 20 % lower than the results from Bertin et al., also the shape of the angular distribution is different. Comparing the results of this work to the SAID FA02 partial wave analysis, the cross sections in the interference region are higher than predicted by SAID, at very backward angles the data are systematically lower than the partial wave solution. The discrepancy at backward angles is increasing towards lower energies. The KH80 solution is significantly higher, i.e. closer to our data, at forward angles, however it describes the observed

behavior at backward angles even less.
Single energy fits of the data give a better description of the π^-p channel than the π^+p channel. The fact that the partial wave fits do not describe both channels equally well might be a hint towards isospin violation in the pion-nucleon system.
The results from this experiment almost triple the available world data base for $\pi^\pm$p elastic scattering at low energies, thus it is now dominated by this experiment. Progress may now be expected from the inclusion of the data into a more sophisticated multi-energy partial wave analysis like the SAID analysis. In such an analysis also the analytic structure of phases will be considered, and results with predictive power can be expected. There should be considerable impact on determining the low energy phase shifts, and it should be possible to better fix the extrapolation into the unphysical region required in the determination of the pion-nucleon sigma term. It will be very interesting to see if the changes in phases due to the results of this experiment will translate into a smaller value for the pion-nucleon sigma term.

Chapter 8

Deutsche Zusammenfassung

Die Hauptmotivation für die Messung von differentiellen Wirkungsquerschnitten in der elastischen Pion-Proton-Streuung bei niedrigen Energien ist der Pion-Proton-Sigma-Term. Dieser Term ist ein Maß für die explizite Brechung der chiralen Symmetrie aufgrund der Stromquarkmassen. Sein Wert kann aus dem Baryonenmassenspektrum und aus Pion-Nukleon-Streudaten bestimmt werden. Um die Ergebnisse dieser beiden Extraktionen zur Übereinstimmung zu bringen, muss jedoch ein sehr großer Strangeness-Anteil in den Seequarks im Nukleon angenommen werden. Ein solch hoher Strangenessanteil im Nukleon ist aber nicht verträglich mit den Beobachtungen anderer Experimente, z.B. in der tiefinelastischen Neutrinostreuung.
Als mögliche Ursache für die Diskrepanz wird im Augenblick die vorhandene Datenbasis für Pion-Nukleon-Streuung angesehen. Besonders wichtig für die Extraktion der Streuamplitude sind Daten bei niedrigen Energien, aber dort führen der Zerfall von Pionen und der erhebliche Energieverlust in Materie zu großen experimentellen Problemen. Deshalb existieren in diesem Bereich nur wenige Datensätze, und die verfügbaren Daten sind teilweise nicht innerhalb der angegebenen Fehler verträglich.

Um diese Situation zu verbessern, wurden im TRIUMF Experiment 778 von der CHAOS-Kollaboration differentielle Wirkungsquerschnitte in der elastischen $\pi^{\pm}$p-Streuung bei Pionenergien zwischen 19.9 und 67.0 MeV gemessen. Als Test für die Rekonstruktion von kleinen Streuwinkeln und die Normierung wurden gleichzeitig mit diesen Messungen $\mu^{\pm}$p-Wirkungsquerschnitte unter Vorwärtswinkeln gemessen. Als Detektor wurde das Spektrometer CHAOS verwendet, das aufgrund seiner kompakten Bauweise und seiner massearmen Drahtkammernkonstruktion für Messungen bei niedrigen Energien geeignet ist. Bei niedrigen Energien und kleinen Streuwinkeln erhält das Proton nicht genug Rückstoßenergie, um das Flüssigwasserstofftarget zu verlassen. Um gestreute Pionen unter kleinen Streuwinkeln, bei denen der Pionzerfall in Myonen einen großen Untergrund erzeugt, zu identifizieren, wurde deshalb für die Messung der Vorwärtswinkel ein Reichweitenteleskop

installiert.
In dieser Doktorarbeit wurden die am M13-Kanal durchgeführten Messungen bei 43.3, 37.1, 32.0, 25.8 und 19.9 MeV ausgewertet. In der Analyse werden die elastischen Pion-Proton-Streuereignisse durch Schnitte auf die Flugzeit im Kanal, die Vertexposition und kinematische Schnitte identifiziert. Für Ereignisse, die im Reichweitenteleskop nachgewiesen wurden, wird zusätzlich die Ortsinformation in diesem Detektor und die Teilchenidentifikation durch ein neuronales Netz verwendet. Verbleibender Untergrund aufgrund von Streuungen an den dünnen Fenstern des Flüssigwasserstofftargets und fehlidentifizierten Myonen wird durch Untergrundabzug beseitigt. Hierfür wurden bei allen Energien auch Messungen mit leerem Target durchgeführt. Die Akzeptanz des Detektors wurde mithilfe von Monte-Carlo-Simulationen bestimmt. Die experimentellen Bedingungen wurden in der Simulation genau nachgebildet. Insbesondere wurden die Auswirkungen des Energieverlusts der Pionen in den Materialien der Kammern genau untersucht, da dieser Effekt bei den niedrigsten Energien die Akzeptanz beeinflusst.

Die in diesem Experiment gemessenen Wirkungsquerschnitte liegen im π^-p-Kanal bei 43.3 MeV zwischen den Daten von Brack et al. und den Daten von Joram et al. Die von Joram et al. beobachteten niedrigen Wirkungsquerschnitte im Bereich von 40 Grad werden nicht bestätigt. Bei 32.0 MeV stimmen die Ergebnisse dieses Experiments mit den Daten von Joram et al. bis zu Streuwinkeln von 80 Grad gut überein, allerdings zeigen sie im Gegensatz zu den Joram et al. Daten keine Abweichung von der SAID-Phasenanalyse bei größeren Winkeln. Die Vorhersagen der Phasenanalysen stimmen mit den Ergebnissen dieses Experiments bei den höheren Energien gut überein, bei 25.8 und 19.9 MeV sind die Wirkungsquerschnitte unter großen Streuwinkeln allerdings niedriger als vorhergesagt. Die KH80-Phasenanalyse beschreibt die gemessenen Daten im π^--Kanal insgesamt besser als die SAID-Phasenanalyse.
In der π^+p-Streuung sind bei 43.3 MeV die in diesem Experiment gemessenen Wirkungsquerschnitte bei großen Streuwinkeln höher als die Ergebnisse von Brack et al. und insbesondere von Joram et al. Bei Streuwinkeln von ungefähr 40 Grad wird das von Joram et al. beobachtete starke Interferenzminimum nicht bestätigt. Bei 32.0 MeV führt der Vergleich mit den von Joram et al. gemessenen Wirkungsquerschnitten für das Interferenzminimum und die Rückwärtswinkel zu ähnlichen Ergebnissen. Die bei 19.9 MeV gemessenen Daten sind ca. 20 % niedriger als die Wirkungsquerschnitte von Bertin et al. Auch die Form der Winkelverteilung ist unterschiedlich.
Verglichen mit der SAID-Phasenanalyse sind die Wirkungsquerschnitte unter Rückwärtswinkeln systematisch niedriger als vorhergesagt, das Interferenz-

minimum der Coulomb-Nuklearen Interferenz ist nicht so ausgeprägt wie erwartet. Die Abweichungen bei großen Winkeln verstärken sich zu niedrigen Energien hin. Die KH80-Phasenanalyse liegt bei Vorwärtswinkeln höher und beschreibt unsere Daten daher besser, allerdings sind die Abweichungen unter Rückwärtswinkeln für diese Lösung noch deutlich größer.
Die Ergebnisse dieses Experiments stellen eine erhebliche Erweiterung der verfügbaren Daten für eine Phasenanalyse bei niedrigen Energien dar, die Anzahl der Datenpunkte für elastische $\pi^{\pm}$p Streuung unterhalb 50 MeV wurde fast verdreifacht. Es wird sich in künftigen Partialwellenanalysen zeigen, ob die erweiterte Datenbasis (zu der auch kürzliche Messungen der Analysierstärken in der $\pi\vec{p}$-Streuung durch unsere Gruppe beitragen) die Probleme des Sigma-Terms und des Strangeness-Anteils lösen werden oder ob ein verbesserter theoretischer Zugang dafür notwendig ist.

Appendix A

CHAOS E778 collaboration

- TRIUMF:
  - P. Amaudruz, L. Felawka, G.J. Hofman, B. Jamieson, D. Ottewell, M. Pavan, K. Raywood
- JLAB:
  - G.R. Smith
- Regina:
  - E.L. Mathie, R. Tacik, D.M. Yeomans
- Trieste:
  - P. Camerini, E. Fragiacomo, N. Grion, R. Rui
- Colorado:
  - J.T. Brack, J. Patterson, R.J. Peterson, R.A. Ristinen
- Melbourne:
  - J.L. Clark, G. Moloney, M.E. Sevior
- Tübingen:
  - J. Breitschopf, H. Clement, H. Denz, R. Meier, F. von Wrochem, G.J. Wagner
- California State University, Sacramento:
  - E.F. Gibson
- Kurchatov-Institute Moscow:
  - O. Patarakin

Appendix B

Tables of pion-proton cross sections

π^+p 43.3 MeV rot.		
θ_{CM}	dσ/dΩ [mb/sr]	Δ(dσ/dΩ)$_{stat}$[mb/sr]
19.52	0.9978E+00	0.9927E-01
20.70	0.6727E+00	0.6357E-01
21.88	0.5713E+00	0.5205E-01
23.07	0.5179E+00	0.4372E-01
24.25	0.2799E+00	0.3562E-01
25.42	0.3938E+00	0.3449E-01
26.61	0.2597E+00	0.2681E-01
27.78	0.2806E+00	0.2978E-01
28.95	0.2567E+00	0.3031E-01
30.13	0.1888E+00	0.2896E-01
31.30	0.2295E+00	0.2887E-01
32.46	0.2142E+00	0.3043E-01
38.85	0.2079E+00	0.1267E-01
41.15	0.2002E+00	0.1184E-01
43.45	0.1785E+00	0.1062E-01
45.74	0.2178E+00	0.1259E-01
48.02	0.2143E+00	0.1205E-01
50.30	0.2370E+00	0.1279E-01
52.56	0.2279E+00	0.1238E-01
54.81	0.2532E+00	0.1344E-01
116.92	0.1171E+01	0.4100E-01
118.80	0.1144E+01	0.3955E-01
120.66	0.1176E+01	0.3982E-01
122.52	0.1198E+01	0.4058E-01
124.36	0.1268E+01	0.4228E-01
126.20	0.1315E+01	0.4371E-01
128.02	0.1274E+01	0.4256E-01

π^+p 43.3 MeV rot.		
θ_{CM}	dσ/dΩ [mb/sr]	Δ(dσ/dΩ)$_{stat}$[mb/sr]
129.83	0.1353E+01	0.4396E-01
131.63	0.1328E+01	0.4368E-01
133.42	0.1400E+01	0.4603E-01
135.20	0.1494E+01	0.4868E-01
136.98	0.1510E+01	0.4947E-01
138.74	0.1495E+01	0.4903E-01
140.49	0.1635E+01	0.5415E-01
142.24	0.1510E+01	0.4965E-01
143.98	0.1470E+01	0.4841E-01
145.71	0.1458E+01	0.4810E-01
147.43	0.1602E+01	0.5221E-01
149.14	0.1667E+01	0.5505E-01
150.85	0.1545E+01	0.5146E-01
152.55	0.1642E+01	0.5460E-01
154.25	0.1603E+01	0.5358E-01
155.94	0.1662E+01	0.5605E-01
157.62	0.1645E+01	0.5483E-01
159.30	0.1619E+01	0.5410E-01
160.97	0.1688E+01	0.5581E-01
162.64	0.1727E+01	0.5758E-01
164.31	0.1743E+01	0.5802E-01
165.97	0.1817E+01	0.6072E-01
167.63	0.1906E+01	0.6434E-01
169.28	0.1798E+01	0.6565E-01

Table B.1: Table of cross sections for π^+p 43.3 MeV rot. The common normalization error is 5.2 % for scattering angles up to 35 degrees and 2.9 % for larger angles.

π^+p 43.3 MeV		
θ_{CM}	dσ/dΩ [mb/sr]	Δ(dσ/dΩ)$_{stat}$[mb/sr]
19.52	0.1159E+01	0.9052E-01
20.70	0.6449E+00	0.7561E-01
21.88	0.6049E+00	0.5423E-01
23.07	0.4051E+00	0.4959E-01
24.25	0.3688E+00	0.3846E-01
25.42	0.3978E+00	0.3720E-01
26.61	0.2439E+00	0.3732E-01

π^+p 43.3 MeV		
θ_{CM}	dσ/dΩ [mb/sr]	Δ(dσ/d$\Omega)_{stat}$[mb/sr]
27.78	0.2108E+00	0.3107E-01
28.95	0.1905E+00	0.2549E-01
30.13	0.1973E+00	0.2562E-01
31.30	0.1650E+00	0.3025E-01
32.46	0.1511E+00	0.2418E-01
38.85	0.1948E+00	0.1410E-01
41.15	0.1850E+00	0.1158E-01
43.45	0.1809E+00	0.1163E-01
45.74	0.2031E+00	0.1260E-01
48.02	0.1968E+00	0.1214E-01
50.30	0.2062E+00	0.1248E-01
52.56	0.2203E+00	0.1205E-01
54.81	0.2433E+00	0.1321E-01
57.06	0.2526E+00	0.1350E-01
59.29	0.2895E+00	0.1525E-01
61.51	0.3166E+00	0.1552E-01
63.72	0.3437E+00	0.1608E-01
65.92	0.3371E+00	0.1545E-01
68.11	0.3539E+00	0.1560E-01
70.29	0.4127E+00	0.1729E-01
72.45	0.3929E+00	0.1719E-01
74.61	0.4267E+00	0.1766E-01
76.75	0.4991E+00	0.1991E-01
78.88	0.4573E+00	0.1861E-01
80.99	0.4966E+00	0.2009E-01
83.10	0.5635E+00	0.2194E-01
85.19	0.5509E+00	0.2135E-01
87.27	0.5702E+00	0.2212E-01
89.33	0.5861E+00	0.2263E-01
91.39	0.7126E+00	0.2669E-01
93.43	0.6564E+00	0.2491E-01
95.45	0.7445E+00	0.2797E-01
97.47	0.7645E+00	0.2983E-01
149.14	0.1540E+01	0.5733E-01
150.85	0.1635E+01	0.5895E-01
152.55	0.1425E+01	0.5084E-01
154.25	0.1625E+01	0.5757E-01
155.94	0.1609E+01	0.5567E-01
157.62	0.1737E+01	0.5932E-01

π^+p 43.3 MeV		
θ_{CM}	dσ/dΩ [mb/sr]	Δ(dσ/dΩ)$_{stat}$[mb/sr]
159.30	0.1652E+01	0.5707E-01
160.97	0.1803E+01	0.6052E-01
162.64	0.1771E+01	0.5839E-01
164.31	0.1765E+01	0.5909E-01
165.97	0.1750E+01	0.5752E-01
167.63	0.1773E+01	0.5991E-01
169.28	0.1888E+01	0.6774E-01

Table B.2: Table of cross sections for π^+p 43.3 MeV. The common normalization error is 5.2 % for scattering angles up to 35 degrees and 2.9 % for larger angles.

π^+p 37.1 MeV		
θ_{CM}	dσ/dΩ [mb/sr]	Δ(dσ/dΩ)$_{stat}$[mb/sr]
21.79	0.8546E+00	0.2761E-01
22.97	0.6923E+00	0.2371E-01
24.14	0.5601E+00	0.2123E-01
25.31	0.4723E+00	0.1948E-01
26.47	0.3724E+00	0.1663E-01
27.65	0.3459E+00	0.1727E-01
28.82	0.2951E+00	0.1686E-01
29.98	0.2695E+00	0.1564E-01
36.37	0.1837E+00	0.5175E-02
38.68	0.1644E+00	0.4412E-02
40.98	0.1600E+00	0.4278E-02
43.27	0.1499E+00	0.3912E-02
45.55	0.1592E+00	0.4251E-02
47.82	0.1635E+00	0.4185E-02
50.09	0.1729E+00	0.4458E-02
52.35	0.1848E+00	0.4904E-02
54.59	0.1765E+00	0.4761E-02
56.83	0.1881E+00	0.4999E-02
59.06	0.2100E+00	0.5451E-02
61.28	0.2223E+00	0.5600E-02
63.48	0.2288E+00	0.5540E-02
65.68	0.2465E+00	0.5948E-02
67.86	0.2604E+00	0.6246E-02
70.04	0.2896E+00	0.6954E-02

π^+p 37.1 MeV		
θ_{CM}	dσ/dΩ [mb/sr]	Δ(dσ/d$\Omega)_{stat}$[mb/sr]
72.20	0.3025E+00	0.7236E-02
74.35	0.3084E+00	0.7313E-02
76.49	0.3405E+00	0.8129E-02
78.61	0.3553E+00	0.8507E-02
80.73	0.3775E+00	0.9171E-02
82.83	0.3879E+00	0.9295E-02
84.92	0.3956E+00	0.9365E-02
87.00	0.4211E+00	0.1007E-01
89.06	0.4272E+00	0.1020E-01
91.12	0.4855E+00	0.1203E-01
93.16	0.5307E+00	0.1365E-01
95.19	0.5213E+00	0.1346E-01
149.01	0.1169E+01	0.3356E-01
150.72	0.1223E+01	0.3462E-01
152.43	0.1178E+01	0.3228E-01
154.13	0.1234E+01	0.3400E-01
155.83	0.1186E+01	0.3165E-01
157.52	0.1197E+01	0.3212E-01
159.20	0.1226E+01	0.3285E-01
160.89	0.1186E+01	0.3163E-01
162.56	0.1195E+01	0.3164E-01
164.24	0.1229E+01	0.3276E-01
165.90	0.1216E+01	0.3249E-01
167.57	0.1301E+01	0.3583E-01
169.23	0.1410E+01	0.4145E-01

Table B.3: Table of cross sections for π^+p 37.1 MeV. The common normalization error is 8 % for scattering angles up to 35 degrees and also 8 % for larger angles.

π^+p 32.0 MeV		
θ_{CM}	dσ/dΩ [mb/sr]	Δ(dσ/d$\Omega)_{stat}$[mb/sr]
24.05	0.1045E+01	0.4311E-01
25.21	0.8229E+00	0.3696E-01
26.38	0.7256E+00	0.3506E-01
27.55	0.5685E+00	0.2980E-01
28.71	0.5871E+00	0.3446E-01
36.24	0.2915E+00	0.9322E-02

π^+p 32.0 MeV		
θ_{CM}	dσ/dΩ [mb/sr]	Δ(dσ/dΩ)$_{stat}$[mb/sr]
38.54	0.2347E+00	0.7680E-02
40.83	0.2069E+00	0.6840E-02
43.11	0.2203E+00	0.7320E-02
45.39	0.2061E+00	0.6968E-02
47.66	0.2143E+00	0.7278E-02
49.92	0.2089E+00	0.7180E-02
52.17	0.2217E+00	0.7818E-02
54.41	0.2063E+00	0.7477E-02
56.64	0.2227E+00	0.7609E-02
58.87	0.2493E+00	0.8112E-02
61.08	0.2570E+00	0.8213E-02
63.28	0.2495E+00	0.7888E-02
65.47	0.2792E+00	0.8543E-02
67.66	0.2849E+00	0.8667E-02
69.83	0.3224E+00	0.9610E-02
71.99	0.3007E+00	0.8935E-02
74.13	0.3433E+00	0.1009E-01
76.27	0.3423E+00	0.1010E-01
78.39	0.3642E+00	0.1074E-01
80.51	0.3768E+00	0.1094E-01
82.61	0.4052E+00	0.1191E-01
84.70	0.4146E+00	0.1212E-01
86.78	0.4395E+00	0.1286E-01
88.84	0.4611E+00	0.1362E-01
90.89	0.4671E+00	0.1356E-01
92.93	0.5156E+00	0.1565E-01
94.96	0.5267E+00	0.1645E-01
148.89	0.1101E+01	0.3527E-01
150.61	0.1056E+01	0.3251E-01
152.33	0.1091E+01	0.3361E-01
154.03	0.1087E+01	0.3278E-01
155.74	0.1131E+01	0.3384E-01
157.43	0.1124E+01	0.3358E-01
159.13	0.1049E+01	0.3075E-01
160.81	0.1156E+01	0.3479E-01
162.50	0.1136E+01	0.3362E-01
164.17	0.1127E+01	0.3311E-01
165.85	0.1117E+01	0.3276E-01
167.52	0.1066E+01	0.3172E-01

π^+p 32.0 MeV		
θ_{CM}	dσ/dΩ [mb/sr]	Δ(dσ/d$\Omega)_{stat}$[mb/sr]
169.19	0.1167E+01	0.3724E-01

Table B.4: Table of cross sections for π^+p 32.0 MeV. The common normalization error is 5.2 % for scattering angles up to 35 degrees and 2.9 % for larger angles.

π^+p 25.8 MeV		
θ_{CM}	dσ/dΩ [mb/sr]	Δ(dσ/d$\Omega)_{stat}$[mb/sr]
11.07	0.3663E+02	0.4688E+00
12.25	0.2491E+02	0.3615E+00
13.42	0.1770E+02	0.2964E+00
14.59	0.1282E+02	0.2425E+00
15.77	0.9643E+01	0.2076E+00
38.37	0.3948E+00	0.1352E-01
40.65	0.3530E+00	0.1205E-01
42.93	0.3213E+00	0.1083E-01
45.20	0.2942E+00	0.1003E-01
47.46	0.2765E+00	0.9584E-02
49.71	0.2829E+00	0.1002E-01
51.95	0.2723E+00	0.9941E-02
54.19	0.2368E+00	0.9086E-02
56.42	0.2631E+00	0.9566E-02
58.63	0.2548E+00	0.9681E-02
60.84	0.2793E+00	0.1014E-01
63.04	0.2626E+00	0.9383E-02
65.23	0.2982E+00	0.1034E-01
67.40	0.2878E+00	0.9950E-02
69.57	0.3047E+00	0.1024E-01
71.72	0.3245E+00	0.1074E-01
73.87	0.3108E+00	0.1038E-01
76.00	0.3207E+00	0.1045E-01
78.13	0.3280E+00	0.1088E-01
80.24	0.3402E+00	0.1131E-01
82.34	0.3620E+00	0.1212E-01
84.43	0.3598E+00	0.1177E-01
86.50	0.3795E+00	0.1217E-01
88.57	0.3980E+00	0.1306E-01
90.62	0.3962E+00	0.1299E-01

π^+p 25.8 MeV		
θ_{CM}	dσ/dΩ [mb/sr]	Δ(dσ/dΩ)$_{stat}$[mb/sr]
92.66	0.4273E+00	0.1436E-01
94.69	0.4404E+00	0.1501E-01
150.48	0.7173E+00	0.2634E-01
152.20	0.6864E+00	0.2567E-01
153.91	0.6993E+00	0.2528E-01
155.62	0.6965E+00	0.2486E-01
157.33	0.6625E+00	0.2278E-01
159.03	0.6895E+00	0.2392E-01
160.72	0.6867E+00	0.2389E-01
162.41	0.6946E+00	0.2432E-01
164.10	0.6657E+00	0.2304E-01
165.78	0.6258E+00	0.2198E-01
167.46	0.6592E+00	0.2363E-01

Table B.5: Table of cross sections for π^+p 25.8 MeV. The common normalization error is 5.2 % for scattering angles up to 35 degrees and 2.9 % for larger angles.

π^+p 19.9 MeV		
θ_{CM}	dσ/dΩ [mb/sr]	Δ(dσ/dΩ)$_{stat}$[mb/sr]
14.54	0.2105E+02	0.3730E+00
15.70	0.1644E+02	0.3282E+00
16.86	0.1240E+02	0.2766E+00
18.02	0.9914E+01	0.2467E+00
19.19	0.7563E+01	0.2095E+00
20.35	0.5337E+01	0.1652E+00
42.75	0.5353E+00	0.1797E-01
45.01	0.4792E+00	0.1628E-01
47.26	0.4028E+00	0.1422E-01
49.51	0.3695E+00	0.1320E-01
51.75	0.3439E+00	0.1261E-01
53.98	0.3245E+00	0.1218E-01
56.20	0.3269E+00	0.1276E-01
58.41	0.2994E+00	0.1221E-01
60.61	0.2889E+00	0.1216E-01
62.80	0.2840E+00	0.1158E-01
64.99	0.2873E+00	0.1151E-01
67.16	0.2869E+00	0.1127E-01

π^+p 19.9 MeV		
θ_{CM}	dσ/dΩ [mb/sr]	Δ(dσ/dΩ)$_{stat}$[mb/sr]
69.32	0.2782E+00	0.1067E-01
71.47	0.2951E+00	0.1161E-01
73.62	0.2931E+00	0.1159E-01
75.75	0.2879E+00	0.1163E-01
77.87	0.3042E+00	0.1217E-01
79.98	0.2816E+00	0.1166E-01
82.08	0.2787E+00	0.1161E-01
84.16	0.2753E+00	0.1153E-01
86.24	0.2984E+00	0.1248E-01
88.30	0.2941E+00	0.1224E-01
90.36	0.3218E+00	0.1322E-01
92.40	0.3370E+00	0.1391E-01
94.43	0.3593E+00	0.1521E-01
96.45	0.3732E+00	0.1601E-01
98.45	0.3756E+00	0.1714E-01

Table B.6: Table of cross sections for π^+p 19.9 MeV. The common normalization error is 5.2 % for scattering angles up to 35 degrees and 2.9 % for larger angles.

π^-p 43.3 MeV rot.		
θ_{CM}	dσ/dΩ [mb/sr]	Δ(dσ/dΩ)$_{stat}$[mb/sr]
19.54	0.3329E+01	0.1218E+00
20.72	0.2689E+01	0.9720E-01
21.91	0.2513E+01	0.8564E-01
23.08	0.2002E+01	0.7612E-01
24.26	0.1626E+01	0.7196E-01
25.43	0.1477E+01	0.6937E-01
26.61	0.1291E+01	0.6433E-01
27.78	0.1301E+01	0.6024E-01
28.95	0.1178E+01	0.5747E-01
30.12	0.9587E+00	0.5995E-01
31.29	0.9261E+00	0.5550E-01
32.46	0.9224E+00	0.5950E-01
38.85	0.7192E+00	0.2880E-01
41.15	0.5453E+00	0.2318E-01
43.45	0.5305E+00	0.2204E-01
45.74	0.4474E+00	0.1999E-01

π^-p 43.3 MeV rot.		
θ_{CM}	dσ/dΩ [mb/sr]	Δ(dσ/dΩ)$_{stat}$[mb/sr]
48.02	0.4278E+00	0.1850E-01
50.30	0.4094E+00	0.1818E-01
52.56	0.4287E+00	0.1933E-01
54.81	0.3966E+00	0.1867E-01
118.80	0.7489E-01	0.9696E-02
120.66	0.1019E+00	0.1133E-01
122.52	0.8597E-01	0.9824E-02
124.36	0.8526E-01	0.1053E-01
126.20	0.8350E-01	0.9025E-02
128.02	0.7454E-01	0.9009E-02
129.83	0.8213E-01	0.8910E-02
131.63	0.5277E-01	0.8973E-02
133.42	0.5629E-01	0.9047E-02
135.20	0.6215E-01	0.8122E-02
136.98	0.4017E-01	0.9188E-02
138.74	0.6450E-01	0.8665E-02
140.49	0.4947E-01	0.1004E-01
142.24	0.5265E-01	0.8971E-02
143.98	0.5770E-01	0.9718E-02
145.71	0.4576E-01	0.9257E-02
147.43	0.3825E-01	0.9137E-02
149.14	0.3192E-01	0.8947E-02
150.85	0.2436E-01	0.9237E-02
152.55	0.2302E-01	0.1137E-01
154.25	0.2630E-01	0.1217E-01
155.94	0.2545E-01	0.1278E-01
157.62	0.3122E-01	0.9923E-02
159.30	0.2843E-01	0.9068E-02
160.97	0.1862E-01	0.9763E-02
162.64	0.2351E-01	0.9132E-02
164.31	0.1702E-01	0.1093E-01
165.97	0.3367E-01	0.1005E-01
167.63	0.2518E-01	0.1029E-01

Table B.7: Table of cross sections for π^-p 43.3 MeV rot. The common normalization error is 5.2 % for scattering angles up to 35 degrees and 2.9 % for larger angles.

π^-p 43.3 MeV		
θ_{CM}	dσ/dΩ [mb/sr]	Δ(dσ/d$\Omega)_{stat}$[mb/sr]
19.54	0.3070E+01	0.1139E+00
20.72	0.2711E+01	0.8330E-01
21.91	0.2044E+01	0.7594E-01
23.08	0.1982E+01	0.7035E-01
24.26	0.1696E+01	0.6562E-01
25.43	0.1340E+01	0.6043E-01
26.61	0.1395E+01	0.5570E-01
27.78	0.1120E+01	0.5408E-01
28.95	0.9916E+00	0.5563E-01
30.12	0.1013E+01	0.5033E-01
31.29	0.9637E+00	0.4560E-01
32.46	0.8945E+00	0.5322E-01
38.85	0.6781E+00	0.2477E-01
41.15	0.5784E+00	0.2055E-01
43.45	0.5046E+00	0.1930E-01
45.74	0.4620E+00	0.1741E-01
48.02	0.4058E+00	0.1657E-01
50.30	0.4112E+00	0.1598E-01
52.56	0.3639E+00	0.1442E-01
54.81	0.3219E+00	0.1393E-01
57.06	0.3246E+00	0.1422E-01
59.29	0.3102E+00	0.1307E-01
61.51	0.3218E+00	0.1277E-01
63.72	0.3070E+00	0.1231E-01
65.92	0.2633E+00	0.1104E-01
68.11	0.2418E+00	0.1012E-01
70.29	0.2406E+00	0.1029E-01
72.45	0.2351E+00	0.1028E-01
74.61	0.2348E+00	0.1029E-01
76.75	0.2265E+00	0.1031E-01
78.88	0.2354E+00	0.1017E-01
80.99	0.2159E+00	0.1045E-01
83.10	0.1870E+00	0.9147E-02
85.19	0.1983E+00	0.9636E-02
87.27	0.1856E+00	0.9480E-02
89.33	0.1718E+00	0.8835E-02
91.39	0.1591E+00	0.9404E-02
93.43	0.1599E+00	0.8860E-02

π^-p 43.3 MeV		
θ_{CM}	dσ/dΩ [mb/sr]	Δ(dσ/dΩ)$_{stat}$[mb/sr]
95.45	0.1718E+00	0.1068E-01
97.47	0.1602E+00	0.1100E-01
150.85	0.4700E-01	0.1295E-01
152.55	0.6794E-01	0.9076E-02
154.25	0.2319E-01	0.1200E-01
155.94	0.3551E-01	0.1109E-01
157.62	0.2164E-01	0.1051E-01
159.30	0.3538E-01	0.9901E-02
160.97	0.3743E-01	0.7095E-02
162.64	0.1946E-01	0.9671E-02
164.31	0.3265E-01	0.1067E-01
165.97	0.1510E-01	0.1179E-01
167.63	0.3248E-01	0.1129E-01

Table B.8: Table of cross sections for π^-p 43.3 MeV. The common normalization error is 5.2 % for scattering angles up to 35 degrees and 2.9 % for larger angles.

π^-p 37.1 MeV		
θ_{CM}	dσ/dΩ [mb/sr]	Δ(dσ/dΩ)$_{stat}$[mb/sr]
21.82	0.2427E+01	0.8200E-01
22.99	0.2141E+01	0.7525E-01
24.16	0.1785E+01	0.6327E-01
25.33	0.1643E+01	0.6018E-01
26.50	0.1451E+01	0.5433E-01
27.67	0.1186E+01	0.4377E-01
28.83	0.1124E+01	0.4377E-01
30.00	0.1033E+01	0.4106E-01
31.16	0.1013E+01	0.4274E-01
38.68	0.6574E+00	0.1586E-01
40.98	0.5606E+00	0.1342E-01
43.27	0.4958E+00	0.1214E-01
45.55	0.4599E+00	0.1147E-01
47.82	0.4222E+00	0.1077E-01
50.09	0.4082E+00	0.1062E-01
52.35	0.4005E+00	0.1086E-01
54.59	0.3497E+00	0.9826E-02
56.83	0.3119E+00	0.9059E-02

π^-p 37.1 MeV		
θ_{CM}	dσ/dΩ [mb/sr]	Δ(dσ/d$\Omega)_{stat}$[mb/sr]
59.06	0.3137E+00	0.9067E-02
61.28	0.2877E+00	0.8123E-02
63.48	0.2804E+00	0.7974E-02
65.68	0.2558E+00	0.7390E-02
67.86	0.2586E+00	0.7525E-02
70.04	0.2403E+00	0.6984E-02
72.20	0.2385E+00	0.7047E-02
74.35	0.2249E+00	0.6851E-02
76.49	0.2244E+00	0.6941E-02
78.61	0.2140E+00	0.6646E-02
80.73	0.1857E+00	0.5953E-02
82.83	0.1991E+00	0.6510E-02
84.92	0.1859E+00	0.6228E-02
87.00	0.1723E+00	0.5952E-02
89.06	0.1653E+00	0.5715E-02
91.12	0.1624E+00	0.5717E-02
93.16	0.1697E+00	0.6180E-02
95.19	0.1583E+00	0.6054E-02
97.20	0.1469E+00	0.6011E-02
149.01	0.6734E-01	0.4836E-02
150.72	0.6044E-01	0.4568E-02
152.43	0.5296E-01	0.4316E-02
154.13	0.4426E-01	0.4424E-02
155.83	0.5173E-01	0.4489E-02
157.52	0.4740E-01	0.4564E-02
159.20	0.3625E-01	0.4014E-02
160.89	0.4207E-01	0.4139E-02
162.56	0.4534E-01	0.3968E-02
164.24	0.3651E-01	0.3883E-02
165.90	0.4710E-01	0.4560E-02
167.57	0.3938E-01	0.4455E-02
169.23	0.3677E-01	0.5337E-02

Table B.9: Table of cross sections for π^-p 37.1 MeV. The common normalization error is 8 % for scattering angles up to 35 degrees and also 8 % for larger angles.

π^-p 32.0 MeV		
θ_{CM}	dσ/dΩ [mb/sr]	Δ(dσ/dΩ)$_{stat}$[mb/sr]
24.06	0.2232E+01	0.6140E-01
25.22	0.1818E+01	0.5284E-01
26.39	0.1710E+01	0.5297E-01
27.55	0.1502E+01	0.5107E-01
28.71	0.1304E+01	0.4690E-01
36.24	0.8364E+00	0.2023E-01
38.54	0.7176E+00	0.1694E-01
40.83	0.6304E+00	0.1528E-01
43.11	0.5789E+00	0.1432E-01
45.39	0.5309E+00	0.1335E-01
47.66	0.5113E+00	0.1335E-01
49.92	0.4418E+00	0.1167E-01
52.17	0.4113E+00	0.1130E-01
54.41	0.3868E+00	0.1110E-01
56.64	0.3536E+00	0.1009E-01
58.87	0.3418E+00	0.9597E-02
61.08	0.3139E+00	0.8859E-02
63.28	0.2956E+00	0.8289E-02
65.47	0.2945E+00	0.8398E-02
67.66	0.2855E+00	0.8348E-02
69.83	0.2780E+00	0.8183E-02
71.99	0.2551E+00	0.7625E-02
74.13	0.2356E+00	0.7265E-02
76.27	0.2332E+00	0.7396E-02
78.39	0.2155E+00	0.6720E-02
80.51	0.2057E+00	0.6617E-02
82.61	0.2035E+00	0.6675E-02
84.70	0.2107E+00	0.6960E-02
86.78	0.2010E+00	0.6931E-02
88.84	0.1921E+00	0.6685E-02
90.89	0.1875E+00	0.6768E-02
92.93	0.1798E+00	0.6702E-02
148.89	0.8130E-01	0.5386E-02
150.61	0.7790E-01	0.5359E-02
152.33	0.7550E-01	0.5518E-02
154.03	0.6994E-01	0.5604E-02
155.74	0.6930E-01	0.5580E-02
157.43	0.7154E-01	0.5449E-02

π^-p 32.0 MeV		
θ_{CM}	dσ/dΩ [mb/sr]	Δ(dσ/d$\Omega)_{stat}$[mb/sr]
159.13	0.7150E-01	0.5566E-02
160.81	0.6140E-01	0.4970E-02
162.50	0.6153E-01	0.5490E-02
164.17	0.5399E-01	0.5192E-02
165.85	0.5419E-01	0.5210E-02
167.52	0.5780E-01	0.6006E-02
169.19	0.5975E-01	0.6301E-02

Table B.10: Table of cross sections for π^-p 32.0 MeV. The common normalization error is 5.2 % for scattering angles up to 35 degrees and 2.9 % for larger angles.

π^-p 25.8 MeV		
θ_{CM}	dσ/dΩ [mb/sr]	Δ(dσ/d$\Omega)_{stat}$[mb/sr]
11.08	0.4014E+02	0.4678E+00
12.25	0.2842E+02	0.3702E+00
13.43	0.2067E+02	0.3054E+00
14.60	0.1590E+02	0.2610E+00
15.77	0.1229E+02	0.2250E+00
28.58	0.1875E+01	0.7420E-01
29.74	0.1702E+01	0.7208E-01
38.37	0.9055E+00	0.2397E-01
40.65	0.7675E+00	0.2031E-01
42.93	0.6341E+00	0.1706E-01
45.20	0.5731E+00	0.1576E-01
47.46	0.5163E+00	0.1438E-01
49.71	0.5035E+00	0.1421E-01
51.95	0.4646E+00	0.1371E-01
54.19	0.4238E+00	0.1320E-01
56.42	0.4077E+00	0.1298E-01
58.63	0.3741E+00	0.1181E-01
60.84	0.3642E+00	0.1144E-01
63.04	0.3359E+00	0.1071E-01
65.23	0.3353E+00	0.1057E-01
67.40	0.2912E+00	0.9398E-02
69.57	0.2897E+00	0.9646E-02
71.72	0.2948E+00	0.9706E-02
73.87	0.2693E+00	0.9222E-02

π^-p 25.8 MeV		
θ_{CM}	dσ/dΩ [mb/sr]	Δ(dσ/dΩ)$_{stat}$[mb/sr]
76.00	0.2818E+00	0.9677E-02
78.13	0.2498E+00	0.8823E-02
80.24	0.2388E+00	0.8575E-02
82.34	0.2279E+00	0.8429E-02
84.43	0.2041E+00	0.7940E-02
86.50	0.2056E+00	0.8009E-02
88.57	0.2115E+00	0.8461E-02
90.62	0.2008E+00	0.8133E-02
92.66	0.1977E+00	0.8614E-02
94.69	0.1767E+00	0.8013E-02
150.48	0.9060E-01	0.8041E-02
152.20	0.9378E-01	0.7714E-02
153.91	0.6864E-01	0.7260E-02
155.62	0.8020E-01	0.7623E-02
157.33	0.7732E-01	0.7523E-02
159.03	0.7052E-01	0.7098E-02
160.72	0.9420E-01	0.7166E-02
162.41	0.7512E-01	0.6551E-02
164.10	0.7777E-01	0.7227E-02
165.78	0.7562E-01	0.7729E-02
167.46	0.5791E-01	0.7143E-02

Table B.11: Table of cross sections for π^-p 25.8 MeV. The common normalization error is 5.2 % for scattering angles up to 35 degrees and 2.9 % for larger angles.

π^-p 19.9 MeV		
θ_{CM}	dσ/dΩ [mb/sr]	Δ(dσ/dΩ)$_{stat}$[mb/sr]
14.54	0.2304E+02	0.5364E+00
15.70	0.1787E+02	0.4509E+00
16.86	0.1398E+02	0.3751E+00
18.03	0.1110E+02	0.3285E+00
19.19	0.9066E+01	0.3058E+00
20.35	0.6936E+01	0.2381E+00
42.75	0.8288E+00	0.2842E-01
45.01	0.7032E+00	0.2552E-01
47.26	0.6180E+00	0.2298E-01
49.51	0.5565E+00	0.2152E-01

π^-p 19.9 MeV		
θ_{CM}	dσ/dΩ [mb/sr]	Δ(dσ/dΩ)$_{stat}$[mb/sr]
51.75	0.5478E+00	0.2113E-01
53.98	0.4729E+00	0.1910E-01
56.20	0.4736E+00	0.1933E-01
58.41	0.4051E+00	0.1738E-01
60.61	0.4095E+00	0.1802E-01
62.80	0.3544E+00	0.1645E-01
64.99	0.3368E+00	0.1494E-01
67.16	0.3248E+00	0.1483E-01
69.32	0.3180E+00	0.1486E-01
71.47	0.2724E+00	0.1307E-01
73.62	0.2880E+00	0.1368E-01
75.75	0.2788E+00	0.1371E-01
77.87	0.2455E+00	0.1258E-01
79.98	0.2451E+00	0.1322E-01
82.08	0.2151E+00	0.1214E-01
84.16	0.2295E+00	0.1336E-01
86.24	0.1996E+00	0.1232E-01
88.30	0.2032E+00	0.1183E-01
90.36	0.2042E+00	0.1307E-01
92.40	0.2084E+00	0.1346E-01
94.43	0.1953E+00	0.1315E-01

Table B.12: Table of cross sections for π^-p 19.9 MeV. The common normalization error is 5.2 % for scattering angles up to 35 degrees and 2.9 % for larger angles.

Appendix C

Ratio plots for previously measured $\pi^{\pm}$p data

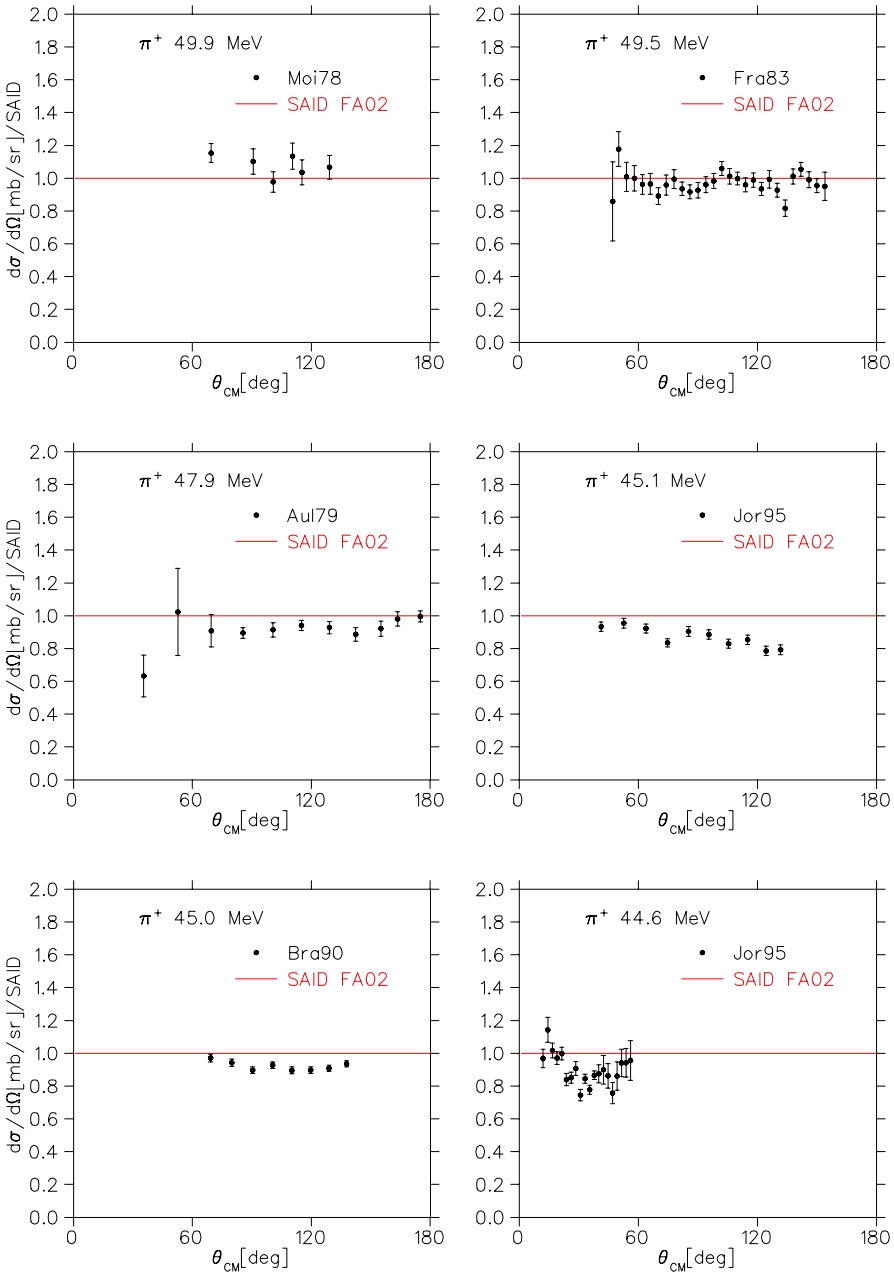

Figure C.1: *Ratios of previously measured $\pi^{\pm}$p data divided by the SAID FA02 solutions for the corresponding energies*

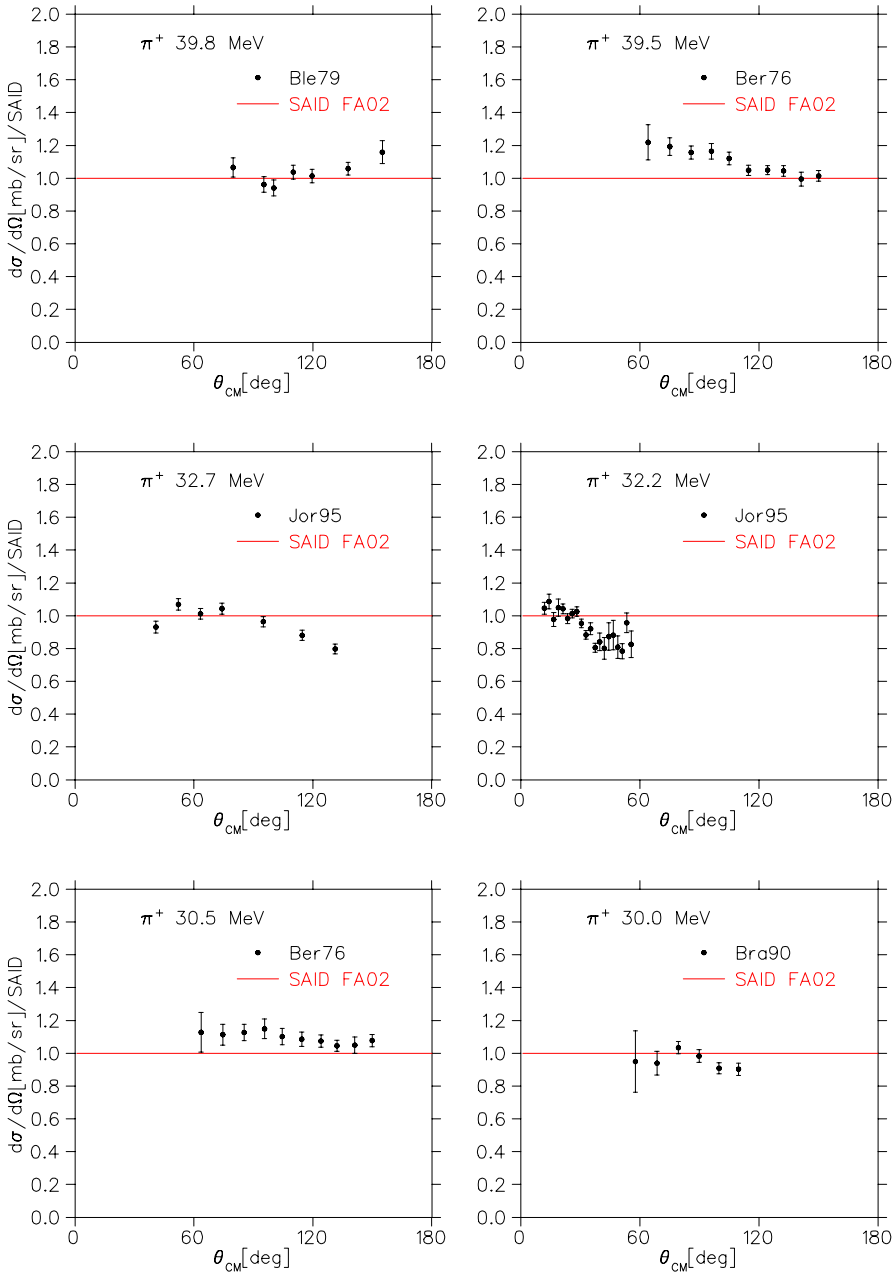

Figure C.2: *Ratios of previously measured $\pi^{\pm}$p data divided by the SAID FA02 solutions for the corresponding energies*

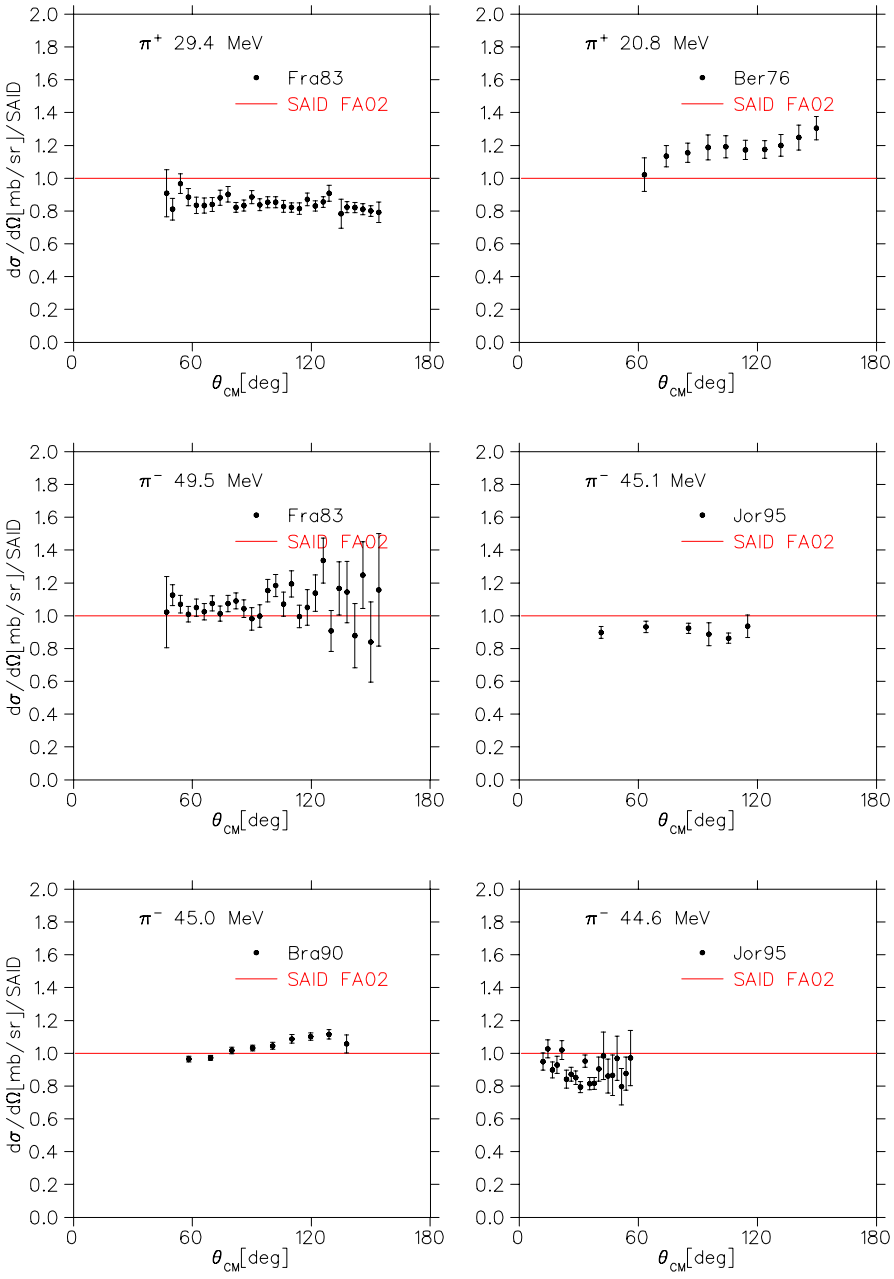

Figure C.3: *Ratios of previously measured $\pi^{\pm}$p data divided by the SAID FA02 solutions for the corresponding energies*

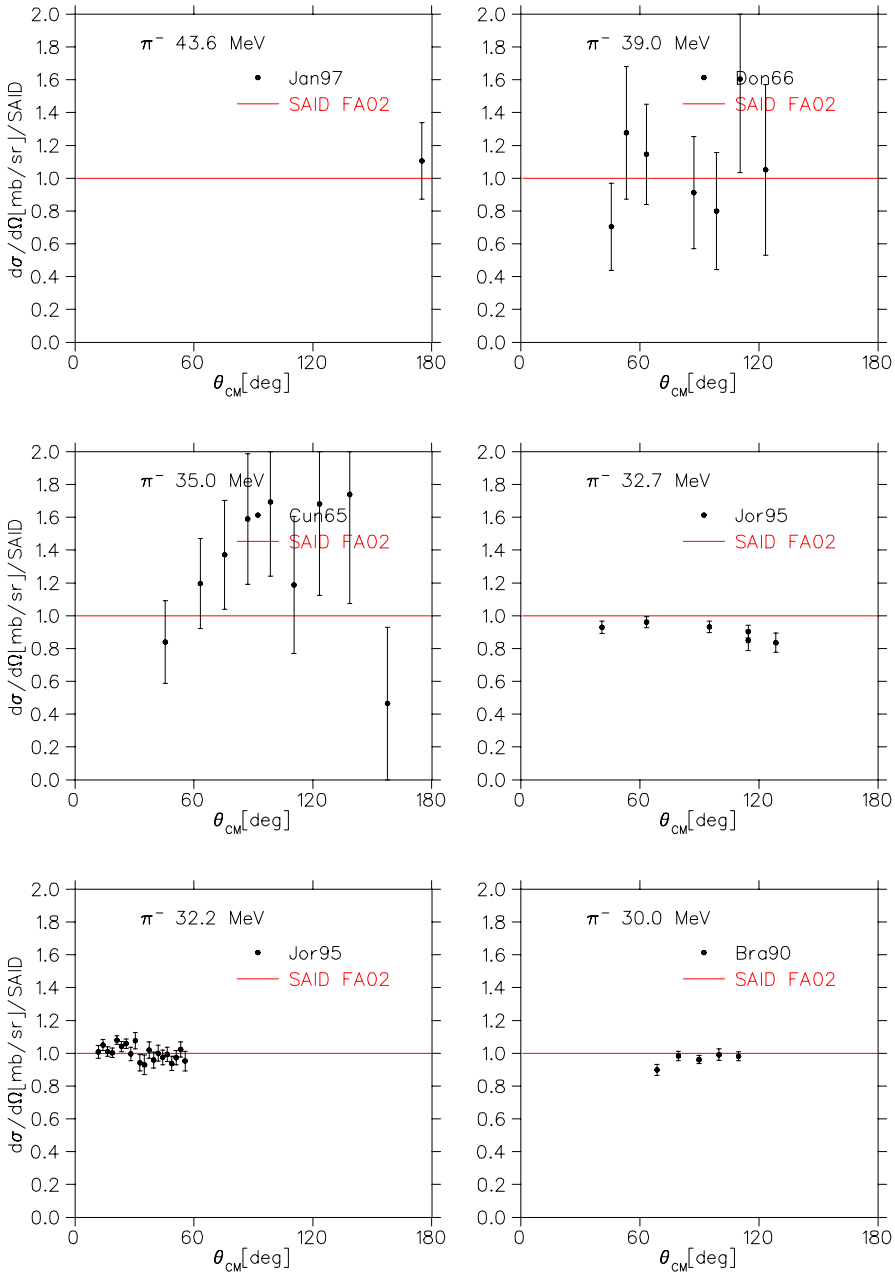

Figure C.4: *Ratios of previously measured $\pi^{\pm}$p data divided by the SAID FA02 solutions for the corresponding energies*

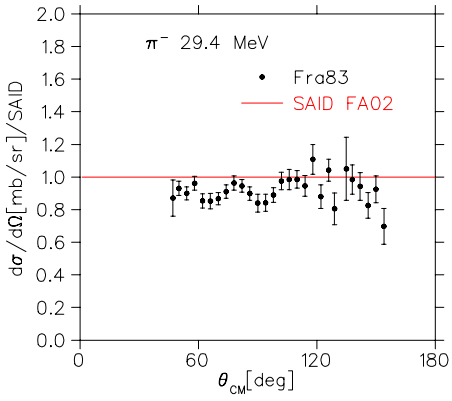

Figure C.5: *Ratios of previously measured $\pi^{\pm}p$ data divided by the SAID FA02 solutions for the corresponding energies*

Appendix D

Drawings for LH_2 target

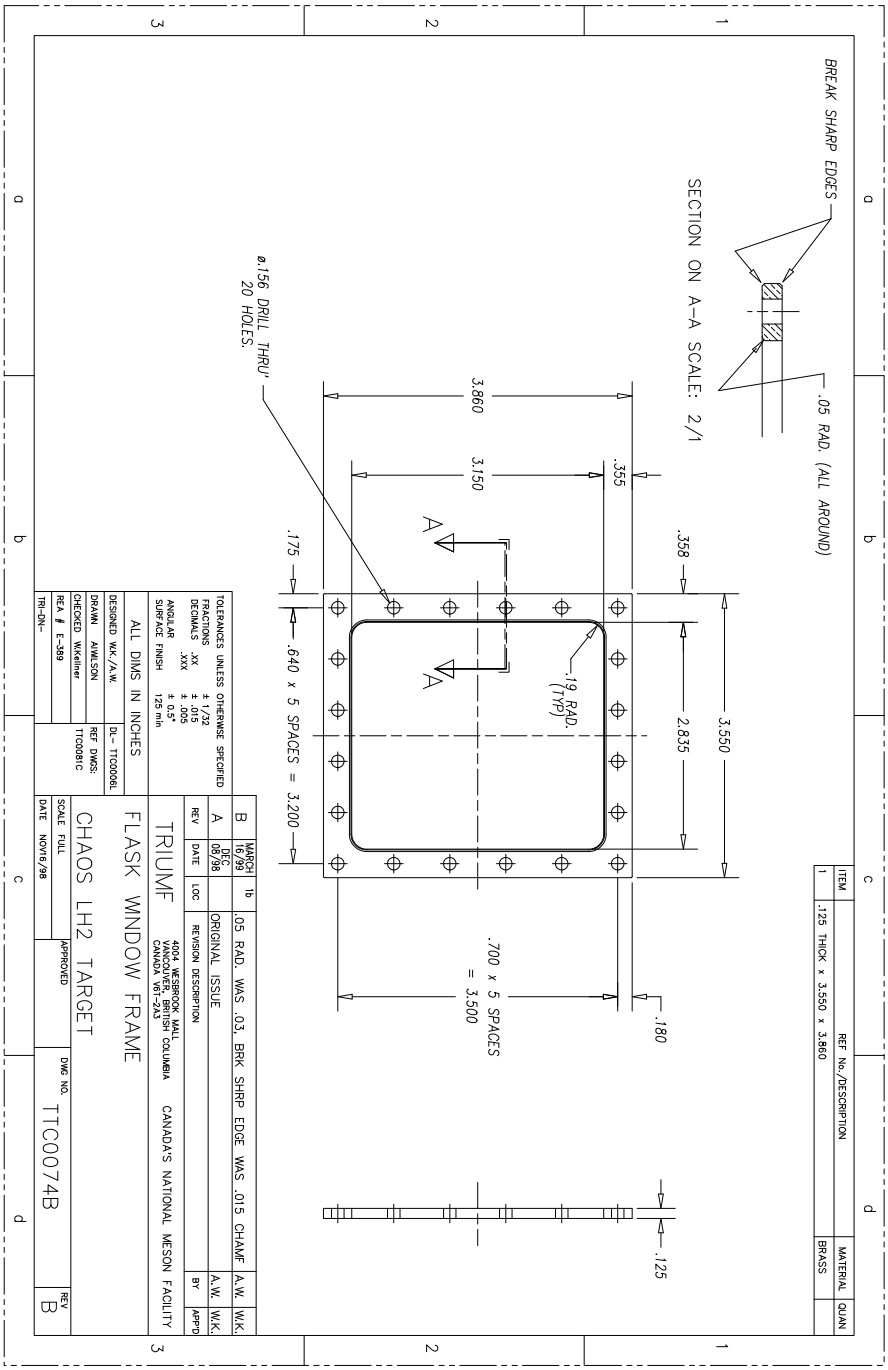

Figure D.1: *Flask window frame[Kel99]*

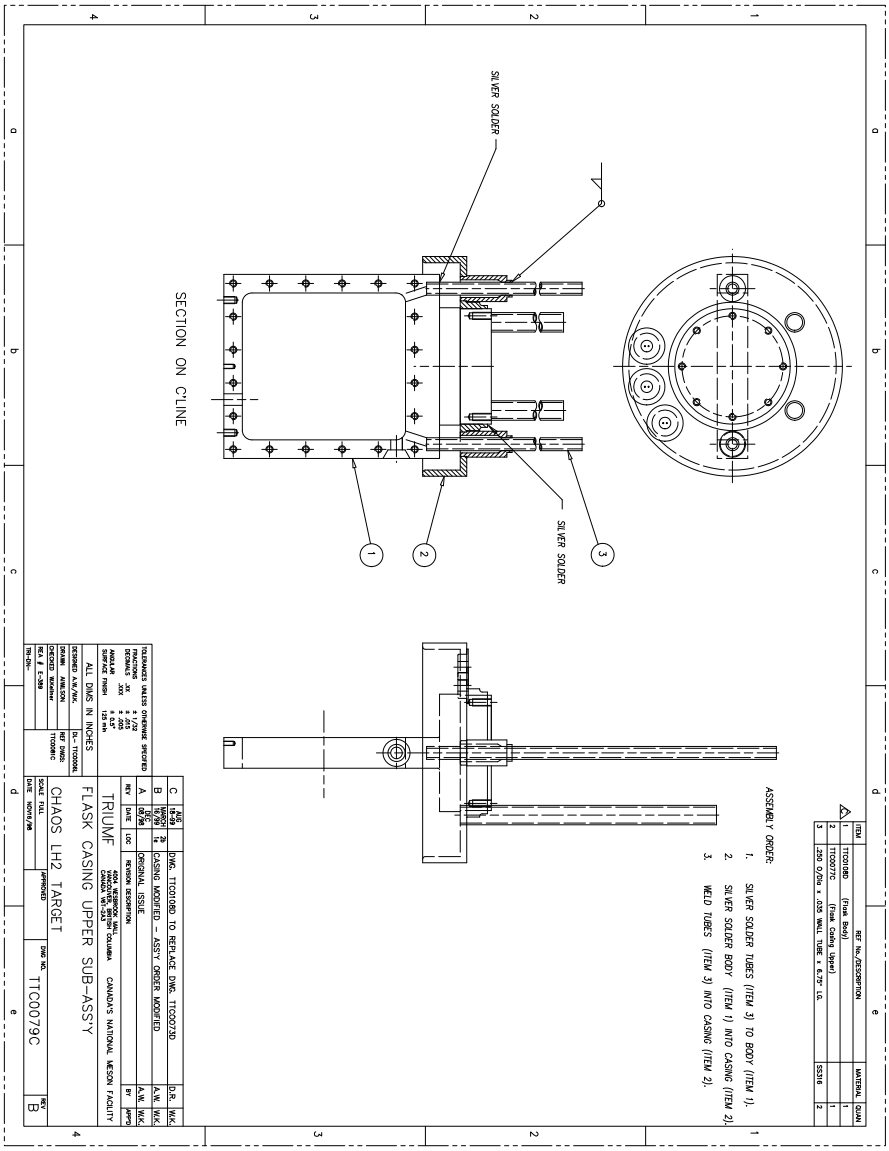

Figure D.2: *Flask casing upper sub-assembly[Kel99]*

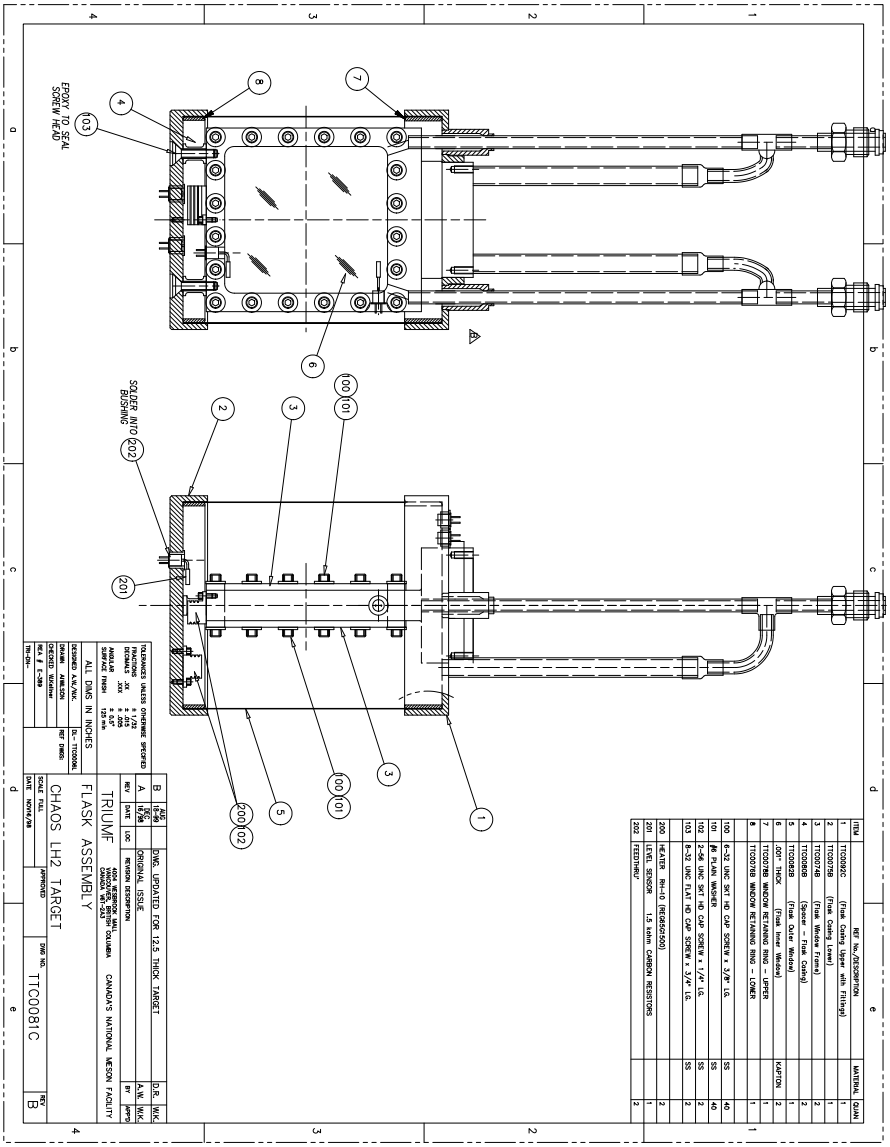

Figure D.3: *Flask assembly[Kel99]*

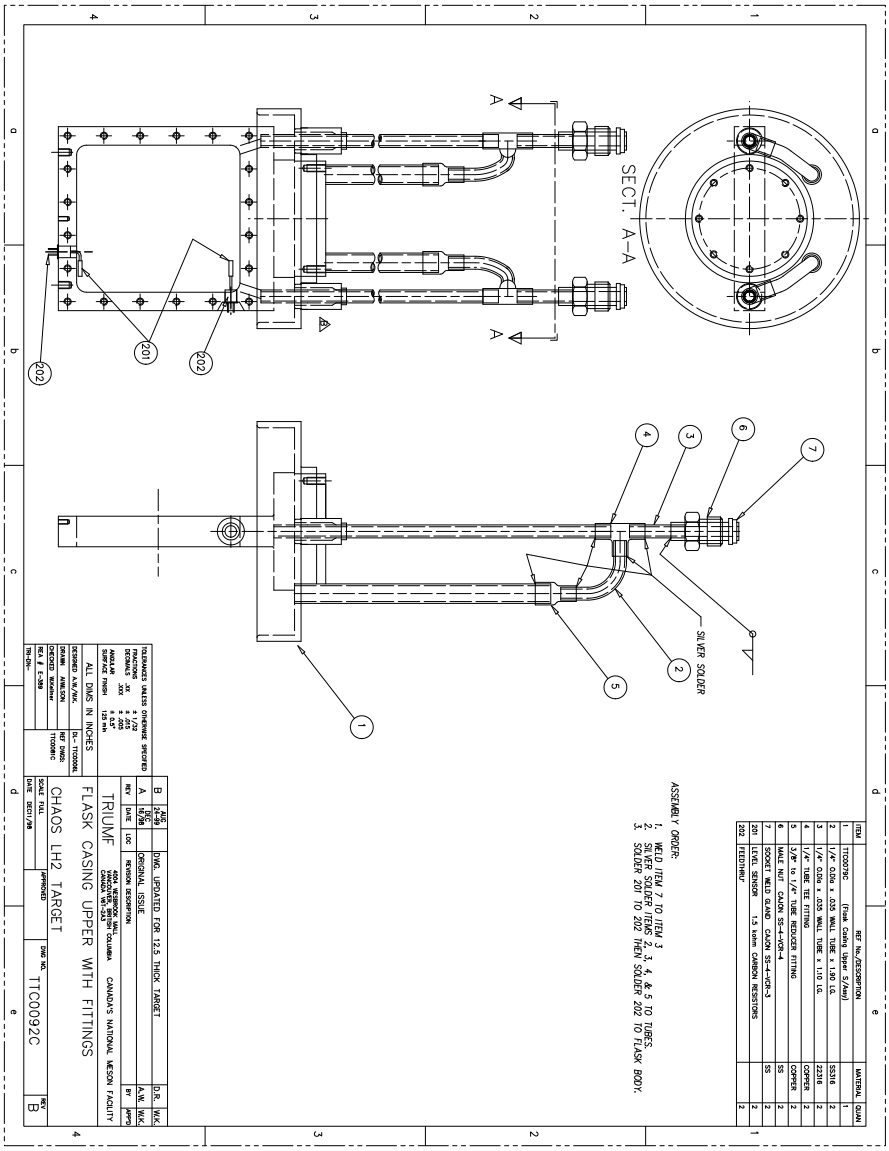

Figure D.4: *Flask casing upper with fittings[Kel99]*

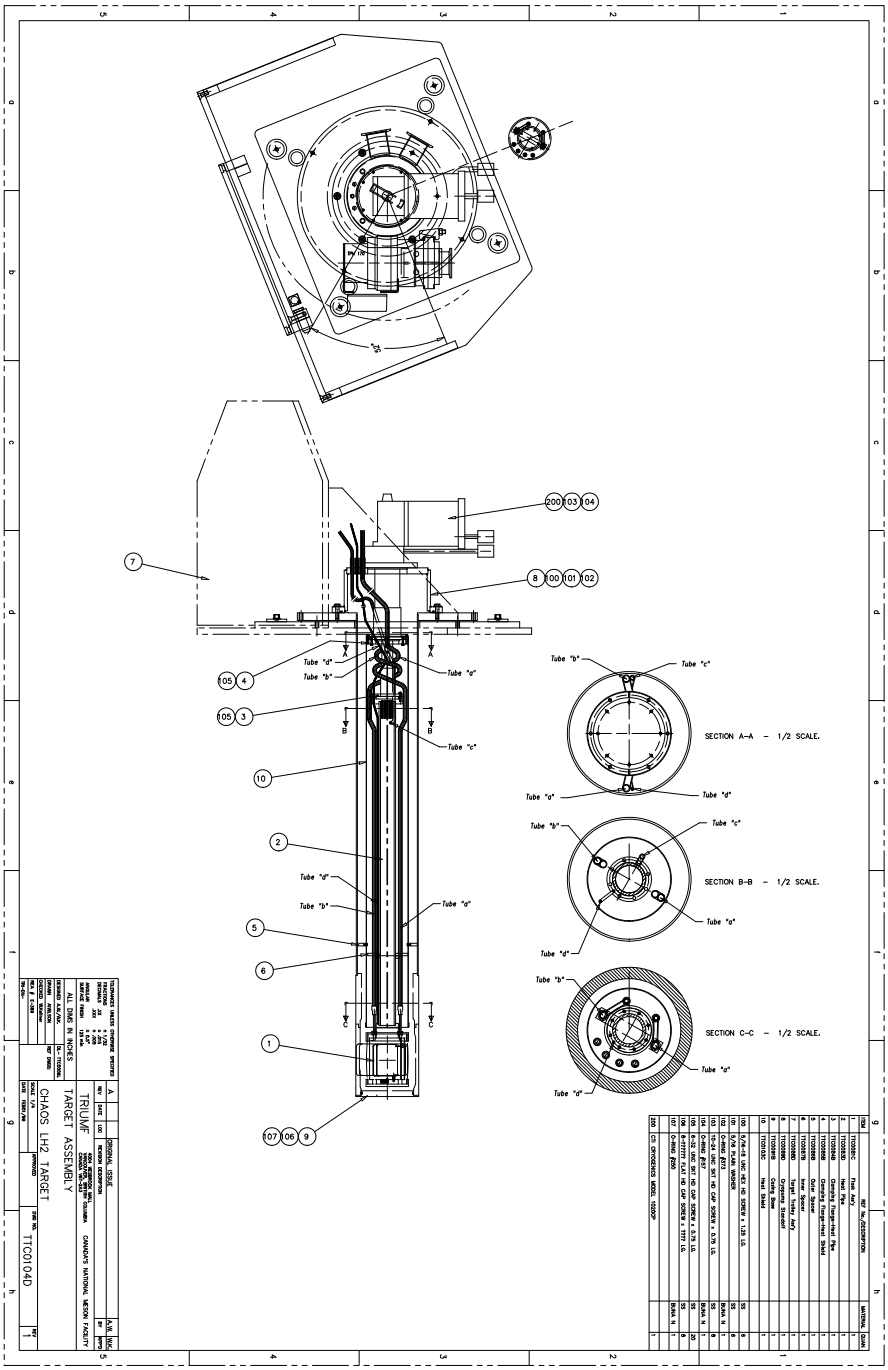

Figure D.5: *Target assembly[Kel99]*

Appendix E

Drawings for range telescope

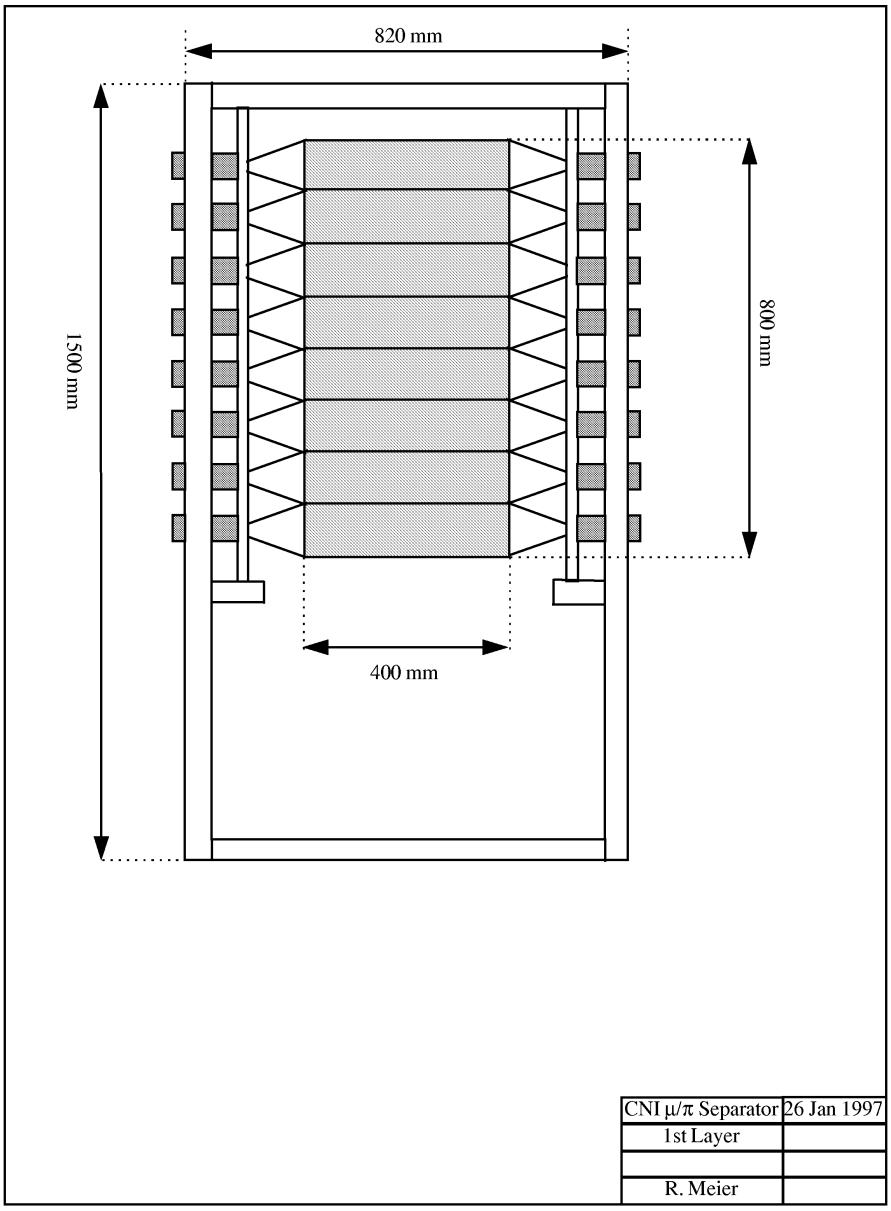

Figure E.1: *View of the first layer of the telescope[Den98]*

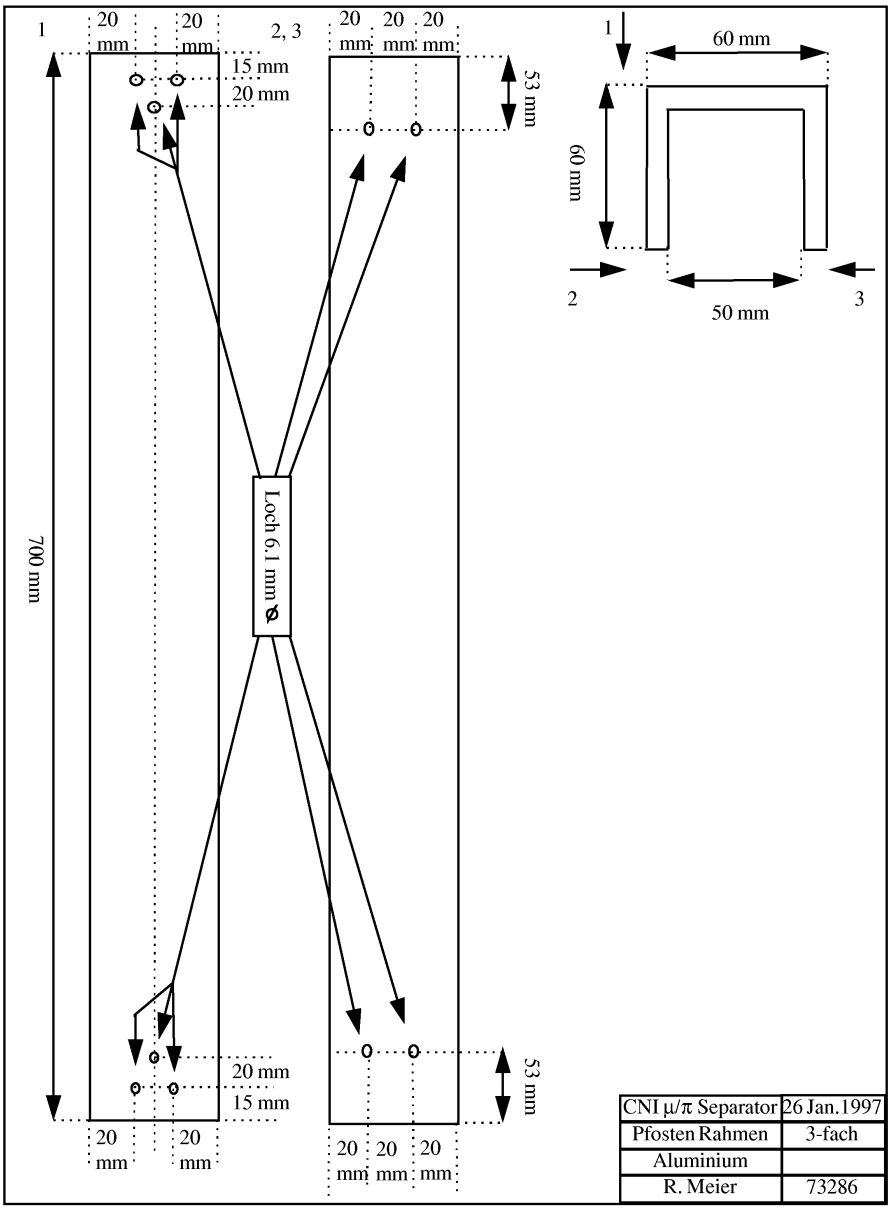

Figure E.2: *Drawing for vertical bars of frame[Den98]*

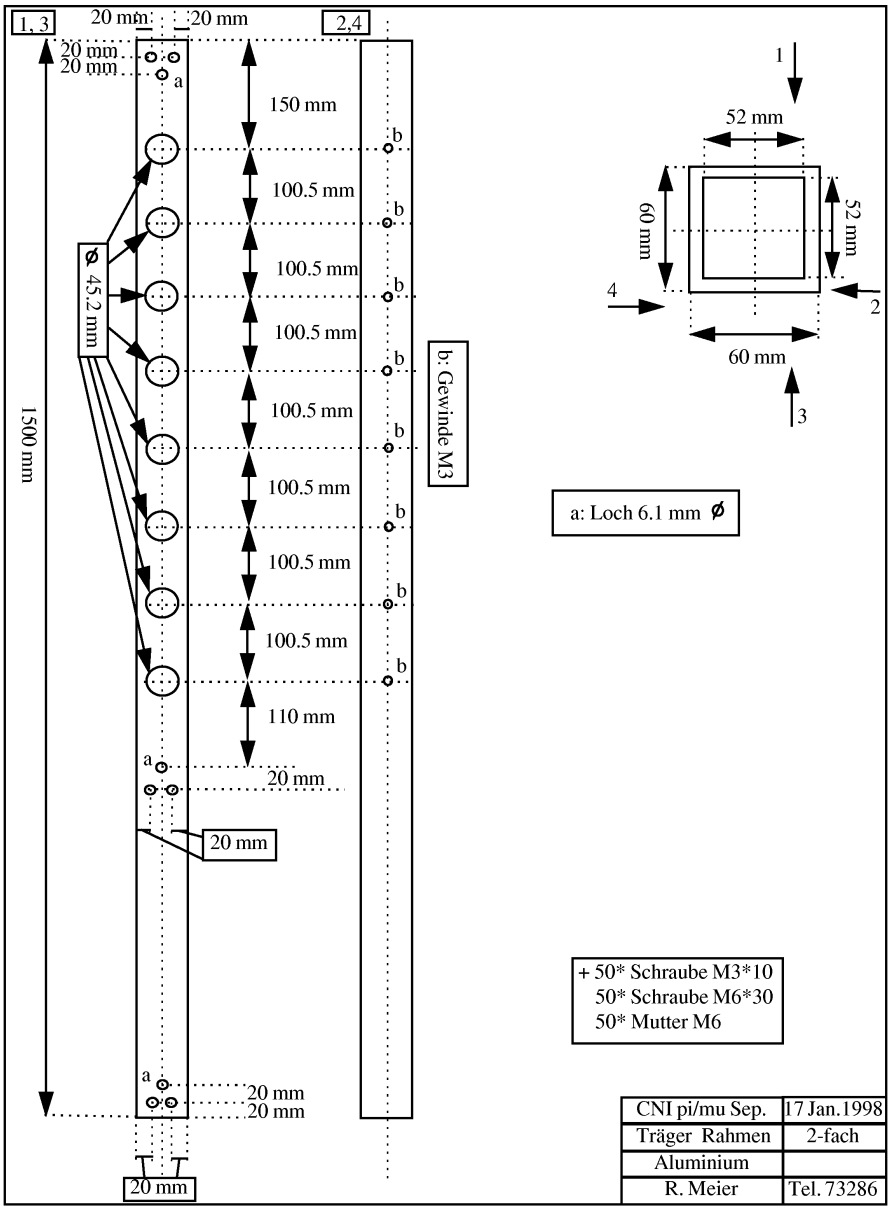

Figure E.3: *Drawing for iron tubes mount[Den98]*

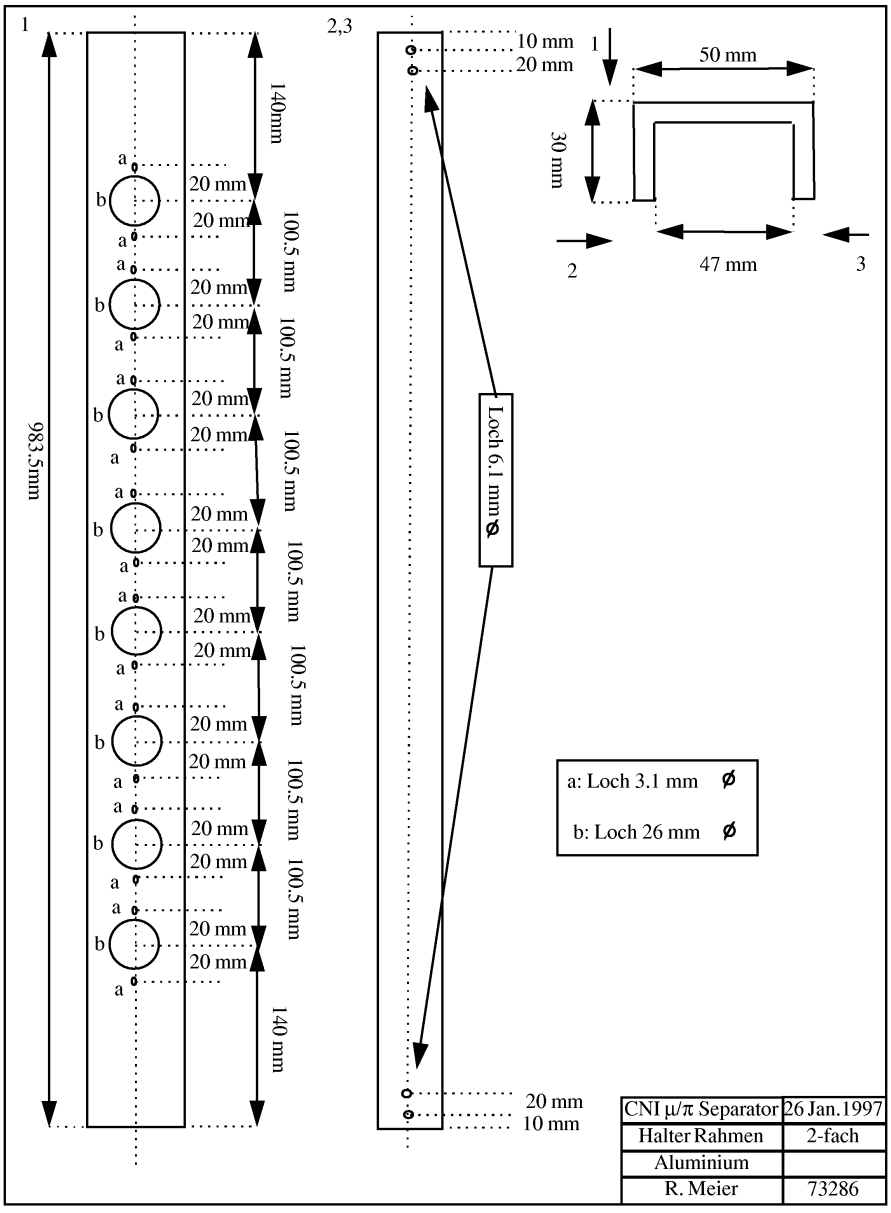

Figure E.4: *Drawing for vertical bars of frame[Den98]*

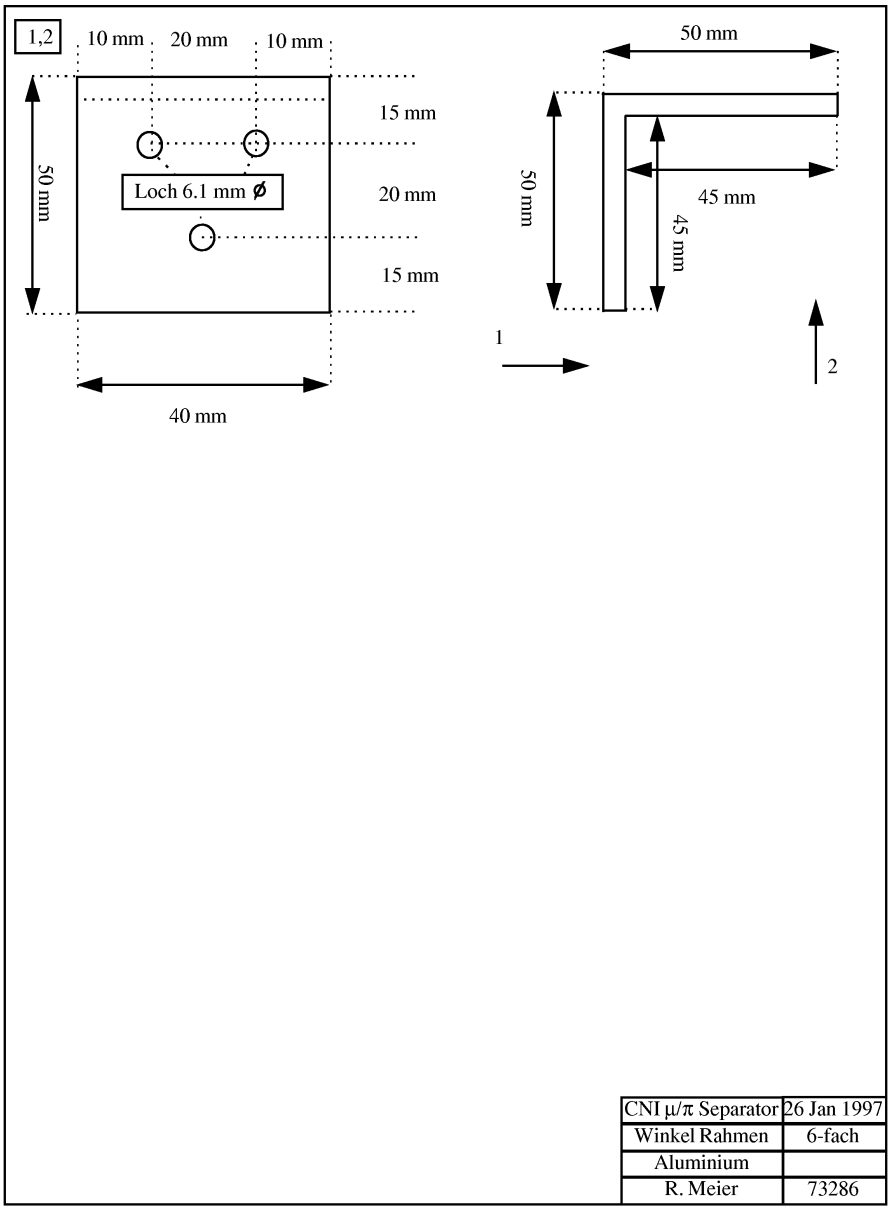

Figure E.5: *Drawing for bracket[Den98]*

List of Figures

List of Tables

Bibliography

[Ama03] P. Amaudruz, private communication (2003)

[Amo01] G. Amoros et al., Nucl. Phys. B **602**, 87 (2001)

[Arn02] R.A. Arndt, J. Briscoe, I.I. Strakovsky, R.L. Workman, M.M. Pavan, arXiv:nucl-th/0311089; SAID phase shift analysis web page: `http://gwdac.phys.gwu.edu/analysis/pin_analysis.html`

[Aul79] E. G. Auld et al., Can. J. Phys. **57**, 73 (1979)

[Baz95] A. O. Bazarko et al., Z. Phys. C **65**, 189 (1995)

[Bec99] T. Becher and H. Leutwyler, Eur. Phys. J. C **9**, 643 (1999)

[Ber76] P. Y. Bertin et al., Nuclear Physics B **106**, 341 (1976)

[Ber96] V. Bernard et al., Phys. Lett. B **389**, 144 (1996)

[Ble79] M. Blecher et al., Phys. Rev. C **20**, 1884 (1979)

[Bor97] B. Borasoy and U. Meißner, Ann. Phys. (NY) **254**, 192 (1997)

[Bra90] J. Brack et al., Phys. Rev. C **41**, 2202 (1990)

[Bro71] L. S. Brown, W. J. Pardee, R. D. Peccei, Phys. Rev. D **4**, 2801 (1971)

[Bro96] R. Brockmann and W. Weise, Phys. Lett. B **367**, 40 (1996)

[Car76] A. S. Carroll et al., Phys. Rev C **14**, 635 (1976)

[Che71] T. P. Cheng, R. Dashen, Phys. Rev. Lett. **26**, 594 (1971)

[Che84] T. P. Cheng and L. F. Li, Gauge theory of elementary particle physics, Oxford University Press (1984)

[Clo76] A.S. Clough et al., Nucl. Phys. B **76**, 15 (1974)

[Cun65] Cundy, LAB PRE-PRINTS **85**, 257 (1965)

[Den98] H. Denz, Diplomarbeit, Tübingen University, unpublished (1998)

[Don66] Donald, LAB PRE-PRINTS **87**, 445 (1966)

[Eri87] T. E. O. Ericson, Physics Letters B **195**, 116 (1987)

[Fet97] N. Fettes and E. Matsinos, Phys. Rev. C **55**, 464 (1997)

[Fet01] N. Fettes and U. Meißner, Phys. Rev. C **63**, 045201 (2001)

[Fra83] J. S. Frank et al., Phys. Rev. D **28**, 1569 (1983)

[Fra00] E. Fragiacomo et al., Nuclear Instruments and Methods in Physics Research A **339**, 45 (2000)

[Gas81] J. Gasser, Ann. Phys. (N.Y.) **136**, 62 (1981)

[Gas88] J. Gasser, H. Leutwyler, M. P. Locher and M. E. Sainio, Phys. Lett. **213B**, 85 (1988)

[Gas88b] J. Gasser, M. E. Sainio, A. Svarc, Nucl. Phys. B **307**, 779 (1988)

[Gas91] J. Gasser, H. Leutwyler, M. E. Sainio, Phys. Lett. **253B**, 252 (1991) and Phys. Lett. **253B**, 260 (1991)

[Gen01] W. Gentzsch, *Proceedings First IEEE/ACM International Symposium on Cluster Computing and the Grid. IEEE Comput. Soc. 2001, Los Alamitos, CA, USA*, 35 (2001)

[Gib98] W. R. Gibbs et al., Phys. Rev. C **57**, 784 (1998)

[Gib03] W. R. Gibbs, Mod. Phys. Lett. A **18**, 1171 (2003)

[Hof93] G. Hofman et al., Nucl. Instr. and Meth. A **325**, 384 (1993)

[Hof97] G. Hofman, Ph.D. thesis, University of British Columbia, unpublished (1997)

[Jam99] B. Jamieson, M.Sc. thesis, University of British Columbia, unpublished (1999)

[Jan97] M. Janousch et al., Phys. Lett. B **414**, 237 (1997)

[Jor95] C. Joram et al., Phys. Rev.C **51**, 2144 (1995)

[Jor95b] C. Joram et al., Phys. Rev.C **51**, 2159 (1995)

[Koc82] R. Koch, Zeitschrift für Physik C **15**, 161 (1982)

[Kel99] W. Kellner, private communication (1999)

[Ker93] M. Kermani, M.Sc. thesis, University of British Columbia, unpublished (1993)

[KH80] R. Koch, E. Pietarinen, Nucl. Phys. A **336**, 331 (1980)

[Klu91] W. Kluge, Rep. Prog. Phys. **54**, 1251 (1991)

[Koc85] R. Koch, Z. Phys. C **29**, 597 (1985)

[Lan99] A. Lanaro et al., in *Proceedings of the Eighth International Symposium on Meson-Nucleon Physics and the Structure of the Nucleon, Zuoz, Switzerland* [π-N Newsletter **15**, 270 (1999)]

[Lei00] D. B. Leinweber, A. W. Thomas and S. V. Wright, Phys. Lett. B **482**, 109 (2000)

[Leu96] H. Leutwyler, Phys.Lett. B **378**, 313 (1996)

[Man59] S. Mandelstam, Phys. Rev. **115**, 1741 (1959)

[Mat97] E. Matsinos, Phys. Rev. C **56**, 3014 (1997)

[Mat04] E.L. Mathie, private communication (2004)

[Mei87] O. Meirav et al., Phys. Rev. C **36**, 1066 (1987)

[Mei02] R. Meier, private communication (2002)

[Mei04] R. Meier et al., Phys. Lett. B, in press, arXiv:nucl-ex/0402018 (2004)

[Met90] M. Metzler, Ph.D. thesis, Karlsruhe University, unpublished (1990)

[Met95] M. Metzler in C. Joram et al., Phys. Rev. C **51**, 2144 (1995)

[MID01] S. Ritt, *MIDAS data aquisition system*, `http://midas.psi.ch`, 2001

[Moi78] M.A. Moinester et al., Phys. Rev. C **18**, 2678 (1978)

[Nam60] Y. Nambu, Phys. Rev. Lett. **4**, 380 (1960)

[Nam61] Y. Nambu and G. Jona-Lasinio , Phys. Rev. **122**, 345 (1960) and Phys. Rev. **124**, 246 (1960)

[Gol61] J. Goldstone, Nuevo Cimento **19**, 154 (1961)

[Gol62] J. Goldstone, A. Salam and S. Weinberg, Phys. Rev. **127**, 965 (1962)

[Odo96] R. Odorico, Comput. Phys. Commun. **96**, 314 (1996)

[Ols00] M. G. Olsson, Physics Letters B **482**, 50 (2000)

[Ols01] M. G. Olsson and W. B. Kaufmann, in *Proceedings of the 9th International Symposium on Meson-Nucleon Physics and the Structure of the Nucleon, Washington, D.C., U.S.A.* [πN-Newsletter **16**, 382 (2001)]

[Ora81] C. Oram et al., Nuclear Instruments and Methods **179**, 95 (1981)

[Pat02] J. D. Patterson et al., Phys. Rev. C **66**, 025207 (2002)

[Pav97] M. M. Pavan and R. A. Arndt, in *Proceedings of the Seventh International Symposium on Meson-Nucleon Physics and the Structure of the Nucleon, Vancouver, B.C., Canada* [πN-Newsletter **13**, 165 (1997)]

[Pav99] M. M. Pavan et al., in *Proceedings of the Eighth International Symposium on Meson-Nucleon Physics and the Structure of the Nucleon, Zuoz, Switzerland* [πN-Newsletter **15**, 118 (1999)]

[Pav01] M. M. Pavan et al, in *Proceedings of the 9th International Symposium on Meson-Nucleon Physics and the Structure of the Nucleon, Washington, D.C., U.S.A.* [πN-Newsletter **16**, 110 (2001)]

[Pav01b] M. M. Pavan, private communication (2001)

[Pav01c] M M. Pavan et al., Phys. Rev. C **64**, 064611 (2001)

[PDG02] K. Hagiwara et al., Phys. Rev. D **66**, 010001 (2002)

[Pok98] Y. Pokravsky, private communication

[Rum86] D.E. Rumelhart et al., Nature **323**, 533 (1986)

[Sai95] M. Sainio, in *Proceedings of the Sixth International Symposium on Meson-Nucleon Physics and the Structure of the Nucleon, Blaubeuren/Tübingen, Germany* [πN-Newsletter **10**, 13 (1995)]

[Sch01] H.Ch. Schröder et al., Eur. Phys. J. C **21**, 473 (2001)

[Smi95] G. R. Smith et al., Nucl. Instr. and Meth. A **357**, 296 (1995)

[Smi96] G. R. Smith, M. Sevior, P. Camerini et al., *TRIUMF - Research Proposal E778, $\pi^{\pm}p$ Differential Cross Sections in the Coulomb-Nuclear Interference Region* (1996)

[Sta99] J. Stahov, in *Proceedings of the Eighth International Symposium on Meson-Nucleon Physics and the Structure of the Nucleon, Zuoz, Switzerland* [πN-Newsletter **15**, 13 (1999)]

[Sta02] J. Stahov, arXiv:hep-ph/0206041 (2002)

[Sta04] J. Stahov, private communication (2004)

[Str79] K. Stricker et al., Phys. Rev. C **19**, 929 (1979)

[TRI96] `http://www.triumf.ca/maps_and_drawings.html`

[Wei66] S. Weinberg, Phys. Rev. Lett. **17**, 616 (1966)

[Wro01] F. von Wrochem, Diplomarbeit, Tübingen University, unpublished (2001)

I would like to express my gratitude to all the people who supported me, helped me and encouraged me during this thesis.
In particular, I'd like to thank my thesis advisor, Prof. Dr. Gerhard J. Wagner, for his support and the complete confidence he put into me and my work.
I'd also like to thank Prof. Dr. Heinz Clement, who was the supervisor of my Diplomarbeit thesis, for his continuing support. Also, this thesis would never have been possible without the advice and patience of PD Dr. Rudi Meier.
Furthermore I'd like to thank all members of the CHAOS collaboration. I truely enjoyed working with you, and I think the atmosphere, cooperation and support I encountered are exceptional. I learned a lot during this time, not only about physics. I am grateful for discussions with Prof. Dr. J. Stahov. Finally I want to thank the people at TRIUMF, the staff of TRIUMF house, all the people at the Physikalisches Institut, the members of the European Graduate School Basel-Tübingen, my brother, my friends and everyone I forgot.
Special thanks go to my parents who supported me throughout my studies.
This work is supported by BMBF (06Tü987I) and DFG (GRK683).